Technical Report Documentation Page

1. Report No.	2. Government Accession No.	3. Recipient's Catalog No.
FHWA/TX-05/0-1707-6		

4. Title and Subtitle	5. Report Date
MECHANISTIC MODEL TO PREDICT THE IMPACT OF THE AGGREGATE MATRIX ON THE PERMANENT DEFORMATION OF ASPHALT MIXTURES	July 2005
	6. Performing Organization Code

7. Author(s)	8. Performing Organization Report No.
Samer Dessouky, Eyad Masad, and Dallas Little	Report 1707-6

9. Performing Organization Name and Address	10. Work Unit No. (TRAIS)
Texas Transportation Institute The Texas A&M University System College Station, Texas 77843-3135	11. Contract or Grant No. Project 0-1707

12. Sponsoring Agency Name and Address	13. Type of Report and Period Covered
Texas Department of Transportation Research and Technology Implementation Office P. O. Box 5080 Austin, Texas 78763-5080	Technical Report: February 2003 – September 2004
	14. Sponsoring Agency Code

15. Supplementary Notes

Project performed in cooperation with the Texas Department of Transportation and the Federal Highway Administration.

Project Title: Long-Term Research on Bituminous Coarse Aggregate

URL: http://tti.tamu.edu/documents/0-1707-6.pdf

16. Abstract

Hot mix asphalt (HMA) is a granular composite material stabilized by the presence of asphalt binder. The behavior of HMA is highly influenced by the microstructure distribution in terms of the different aggregate particles present in the mix, the directional distribution of aggregates, the distribution of voids, and the nucleation and propagation of cracks. Conventional continuum modeling of HMA lacks the ability to explicitly account for the effect of aggregate microstructure distribution features. This report presents the development of elastic and visco-plastic models that account for important aspects of the aggregate and microstructure distribution in modeling the macroscopic behavior of HMA. The objective of Project 0-1707 is to develop tools by which engineers can judge the impact of the aggregate on the performance of HMA based on simple and repeatable tests. Of greatest concern in Project 0-1707 is the ability of the HMA to resist permanent deformation or to rut, which leads to safety concerns, especially under wet surface conditions.

In this report, the research team develops an approach is developed to introduce a length scale to the elasticity constitutive relationship in order to capture the influence of aggregate particle sizes on HMA response. A finite element (FE) analysis is used to analyze the microstructure response and predict the macroscopic properties of HMA. Each point in the microstructure is assigned effective local properties that are calculated using an analytical micromechanical model that captures the influence of the number of particles on the microscopic response of the HMA. The moving window technique and autocorrelation function are used to determine the microstructure characteristic length scales that are used in strain gradient elasticity. A number of asphalt mixes with different aggregate types and size distributions are analyzed .

An elasto-visco-plastic continuum model is developed to predict HMA response and performance. The model incorporates a Drucker-Prager yield surface that is modified to capture the influence of stress path direction on the material response. Parameters that reflect the directional distribution of aggregates and damage density in the microstructure are included in the model. The elasto-visco-plastic model is converted into a numerical formulation and is implemented in FE analysis using a user-defined material subroutine (UMAT). A fully implicit algorithm in time-step control is used to enhance the efficiency of the FE analysis. The FE model used in this project simulates experimental data and pavement section.

17. Key Words	18. Distribution Statement
Asphalt Mixtures, Aggregate Matrix, Aggregate Shape, Aggregate Form, Aggregate Texture, Permanent Deformation, Continuum Damage Models, Elastic-visco-plastic Constitutive Models	No Restrictions. This document is available to the public through NTIS: National Technical Information Service Springfield, Virginia 22161 http://www.ntis.gov

19. Security Classif.(of this report)	20. Security Classif.(of this page)	21. No. of Pages	22. Price
Unclassified	Unclassified	144	

MECHANISTIC MODEL TO PREDICT THE IMPACT OF THE AGGREGATE MATRIX ON THE PERMANENT DEFORMATION OF ASPHALT MIXTURES

by

Samer Dessouky
Graduate Research Assistant
Texas A&M University

Eyad Masad
Research Engineer
Texas Transportation Institute

and

Dallas Little
Senior Research Fellow
Texas Transportation Institute

Report 0-1707-6
Project 0-1707
Project Title: Long-Term Research on Bituminous Coarse Aggregate

Performed in cooperation with the
Texas Department of Transportation
and the
Federal Highway Administration

July 2005

TEXAS TRANSPORTATION INSTITUTE
The Texas A&M University System
College Station, Texas 77843-3135

DISCLAIMER

The contents of this report reflect the views of the authors, who are responsible for the opinions, findings, and conclusions presented herein. The contents do not necessarily reflect the official views or policies of the Texas Department of Transportation (TxDOT) or the Federal Highway Administration (FHWA). This report does not constitute a standard, specification, or regulation. Additionally this report is not intended for construction, bidding, or permit purposes. Dr. Dallas N. Little, P.E. (40392) is the principal investigator for the project.

ACKNOWLEDGMENTS

The authors wish to thank Ms. Caroline Herrera of the Construction Division of TxDOT for her guidance and support during this project. We also thank TxDOT and the FHWA for the cooperative sponsorship of this project.

TABLE OF CONTENTS

Page

TABLE OF CONTENTS (cont)

Page

TABLE OF CONTENTS (cont)

Page

LIST OF FIGURES

Figure **Page**

LIST OF FIGURES (cont)

Figure **Page**

LIST OF FIGURES (cont)

Figure **Page**

LIST OF TABLES

Table **Page**

CHAPTER I

INTRODUCTION

PROBLEM STATEMENT

Permanent deformation is one of the main distresses in asphalt pavements. It occurs primarily due to shear failure in hot mix asphalt (HMA). The shear strength of an asphalt mix is a result of aggregate interlock and adhesion provided by the asphalt binder.

Careful review of the literature showed that two main approaches have usually been followed in modeling permanent deformation: the continuum modeling approach and the micromechanical modeling approach. The advantage of continuum models is that once the material properties are known, simulations of material response and performance can be achieved through finite element (FE) analysis under different boundary conditions. However, detailed information about the initial distribution of the microstructure and its evolution is not explicitly considered in these models. In contrast, micromechanical models have the capability to consider the microstructure distribution and the interactions among the microstructure constituents.

This approach, however, has been limited in modeling the actual geometry of the microstructure, as idealized aggregate shape has typically been used in these models. In addition, simplified assumptions have been employed to model the interactions among the HMA constituents.
An appealing approach that has also been developed for modeling granular materials relies on quantifying the microstructure in the form of scalar functions and directional distribution tensors that are incorporated in continuum constitutive models. This is a powerful approach, as it inherits the advantages of continuum modeling in terms of the efficiency in numerical simulation and at the same time it explicitly captures the influence of the microstructure distribution on the macroscopic response of the material.

This report deals with the development of continuum models for HMA that account for key features of the microstructure distribution and with FE implementation of these models. Two main advances are registered in this study. The first is related to enhancing the elastic analysis of the HMA response through employing strain gradient theory and effective local material properties. Strain gradient theory employs length scales in the constitutive relationship to account for the size variation within the microstructure and its effect on the macroscopic response. Micromechanics analysis is used to obtain the effective local material properties, which are in turn used in the FE analysis to obtain macroscopic elastic properties of HMA.

The second advancement registered in this study is the development of an elasto-visco-plastic constitutive model for HMA. This model considers several factors that are known to influence HMA permanent deformation such as aggregate structure friction and dilation, confining pressure, strain rate, stress path dependency, and microstructure characteristics that reflect anisotropy and damage.

OBJECTIVES

This study deals with the development of multiscale constitutive models for HMA. In these models, key features of the microstructure are measured and incorporated in continuum constitutive models of asphalt mixes. The main objectives of this study are to:

1. Develop a gradient elasticity constitutive relationship that accounts for the microstructure characteristics such as different particle size and asphalt film size distributions and strain localization.

2. Implement the gradient elasticity constitutive relationship in a FE model for the analysis of HMA response. The model reduces the sensitivity of FE analysis microscopic and macroscopic response to mesh resolution.

3. Develop an elasto-visco-plastic continuum model that links the microstructural properties in terms of aggregate anisotropy and damage to permanent deformation of the material. The model also accounts for the influence of loading rate, confining pressure, stress path direction, and dilation under shear loading.

4. Implement the elasto-visco-plastic continuum model into FE analysis to study the response of HMA under a variety of boundary conditions to predict permanent deformation.

CHAPTER II

LITERATURE REVIEW

Asphalt pavements are composite materials consisting of interspersed aggregates, asphalt binder, and air voids. Their constitutive behavior is defined by the interaction of these constituents. The load-carrying behavior and resulting failure of such materials depends on many mechanisms that occur at the constituent level.

Traffic loading repetitions and climate condition effects on hot mix asphalt (HMA) cause permanent deformation that is considered to be one of the most important pavement distresses. This chapter summarizes the causes and mechanisms of permanent deformation in HMA and the current approaches found in the literature to model this phenomenon. It also discusses the contributions reported in the literature on modeling HMA permanent deformation under the two primary approaches; namely the continuum approach and the micromechanical approach. A brief review of the basics of plasticity and visco-plasticity theories is also presented.

CAUSES AND MECHANISMS OF PERMANENT DEFORMATION

Permanent deformation in asphalt pavements manifests itself as depressions along the wheel paths as shown in Fig. 2.1. According to the National Cooperative Highway Research Program (Witczak 1998), permanent deformation was selected as the most serious problem for highways and runways in the United States among all the distresses in asphalt pavements. Fatigue cracking was rated the second most serious problem, followed by thermal cracking.

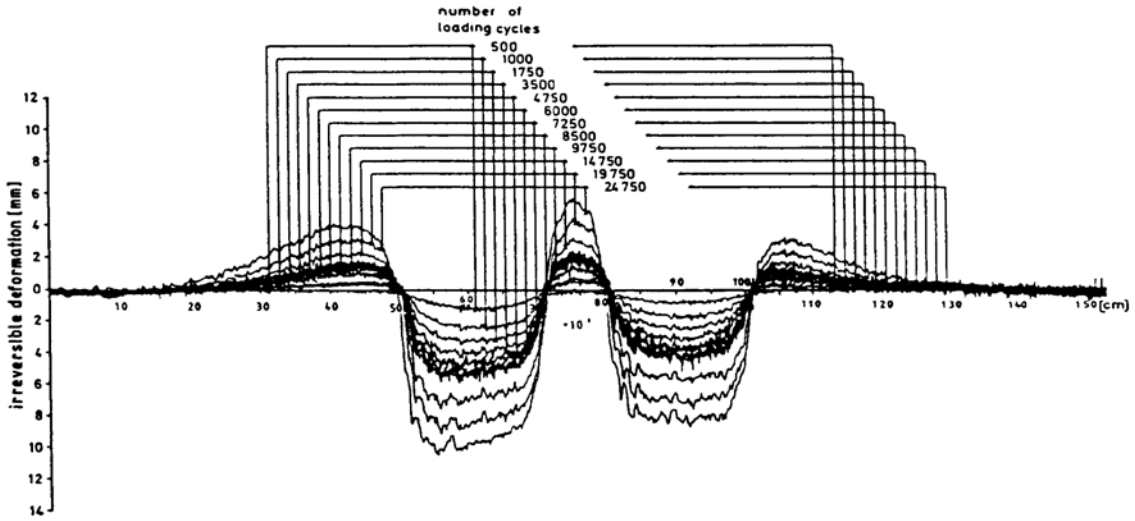

Figure 2.1. Effect of Wheel Loading Repetitions on Permanent Deformation Profile (after Eisenmann and Hilmer 1987).

Deformation in HMA is a complex phenomenon where aggregate, binder, and aggregate-binder interface properties control overall performance. These properties change over time until the mix reaches the end of its design life.

Prediction of rutting requires a knowledge of material characteristics that relates HMA strains to stresses. Rutting develops gradually as the number of load applications increases. As summarized by the Strategic Highway Research Program (SHRP 1991), rutting principally occurs due to repetitive shear deformation under a variety of traffic loading. Loading conditions in the form of magnitude, tire pressure, and traffic volume; environmental conditions in the form of temperature; and HMA properties in the form of aggregate characteristics (shape, texture, and structure), and binder type are among the major contributors to rutting resistance. Extensive literature of studies that considered rutting as a function of loading and environmental conditions can be found in Mclean and Monismith (1974), Brown and Bell (1977), Sousa et al. (1993) and Lytton et al. (1993).

The mechanism of permanent deformation is a combination of densification (decrease in volume) and shear deformation. Using a wheel-tracking device, Eisenmann and Hilmar (1987) concluded that pavement rutting can develop in two stages in HMA. First the initial stage is due to the accumulation of the permanent vertical deformation within the pavement layers under traffic loads. The increase of irrecoverable deformation below the tires is distinctly greater than the increase in the upheaval zones. Second, following the initial stage, the volume decreased beneath the tires is approximately equal to the volume increased in the adjacent upheaval zones. This indicates that compaction under traffic is completed for the most part and that further rutting is caused essentially by the displacement of material.

Based on experimental measurements as well as numerical simulations, Tashman (2003) summarized the causes of rutting due to energy dissipation in three internal mechanisms:

- Overcoming the friction between the aggregates coated with binder,
- Overcoming interlocking between the aggregates, which is responsible for the material dilation, and
- Overcoming the bonding between the binder elements (cohesion) and between the binder and aggregates (adhesion).

MECHANISTIC APPROACHES FOR MODELING HMA RESPONSE

Most design procedures used in design guides are based on linear elastic multilayer analysis. Typically, the elastic response is related to rutting through empricial relationships between the elastic strain and plastic strain. However, it has been shown over the years that the highly nonlinear response of HMA is too complex to be captured satisfactorily through the linear elastic analysis of HMA response. Huang (1967) showed that deformation behavior is a function of both the hydrostatic and deviatoric stress states. He also noticed that the mixes dilate under purely deviatoric stresses. Brown and Cooper (1980) concluded that the response of HMA in triaxial tests was a function in the deviatoric and confining stresses. Deshpande and Cebon (1999) developed a

constitutive model for steady-state deformation of idealized asphalt mixes to predict rutting under a moving load using triaxial compression tests. They reported the dilation phenomenon under compression load and the dependency of deformation on the hydrostatic pressure and the deviatoric stress.

There is overwhelming evidence in the literature that mechanistic models are needed to analyze HMA response and performance. These models have been used to relate microstructure distribution and indvidual constituent properties to macroscopic properties and to predict the macroscopic response and performance of HMA.

Continuum Approach

Although HMA is essentially a multicomponent interacted discrete composite, the concept of a continuum representation has been notionally accepted. This allows one to use the notations of deformable mechanics principles such as stresses and strains. The stresses and strains, or their derivatives with respect to time, can be linked together in a constitutive equation. Joined with equilibrium equations and boundary conditions, constitutive equations permit the evaluation of the pavement structure response either analytically or numerically.

Experimental observations made by Perl et al. (1983) and Sides et al. (1985), and others, proposed that the total strain of HMA has recoverable and irrecoverable elements, some of which are time-dependent and some of which are time-independent. The total strain is separated into four components as shown in Fig. 2.2 for the first cycle of a creep test as follows:

$$\varepsilon = \varepsilon^{e} + \varepsilon^{ve} + \varepsilon^{p} + \varepsilon^{vp} \qquad (2\text{-}1)$$

where ε is the total strain and ε^{e} is the elastic strain, which is recoverable and time-independent, meaning that the material exhibits no permanent strains in a loading /unloading cycle and this state is independent of the rate of loading and unloading. ε^{ve} is the visco-elastic strain, which is recoverable and time-dependent. ε^{p} is the plastic strain, which is irrecoverable and time-independent. ε^{vp} is the visco-plastic strain, which is irrecoverable and time-dependent. In general, the viscous components depend on the load duration and the rate of loading/unloading. No matter what the rate of loading/unloading, the same magnitude of permanent strain is obtained for the same loading history. In general, HMA behavior varies from elastic and linear visco-elastic at low temperatures and/or fast loading rates to nonlinear visco-elastic, visco-plastic, and plastic at high temperatures and/or slow loading rate.

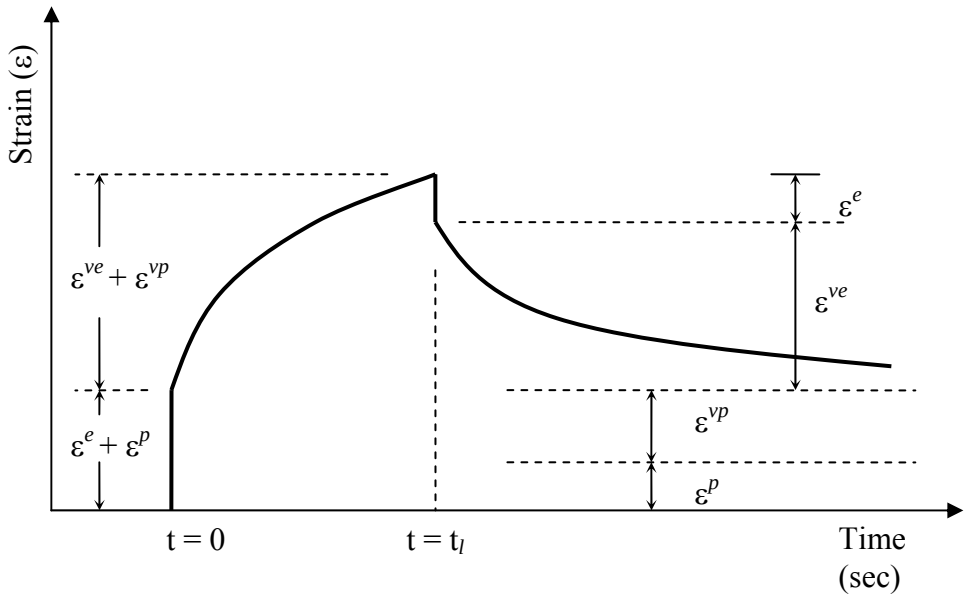

Figure 2.2. Schematic Representation of the Various Strain Components in an Elasto-Visco-Plastic Material.

The instantaneous response reflects the time-independent component, whereas the viscous response reflects the time-dependent component. The relative contribution of each component depends on temperature and loading condition. Rutting is due to the visco-plastic deformation, and consequently, the discussion herein will focus on models that consider the visco-plastic deformation of HMA.

Abdulshafi and Majidzadeh (1985) developed a one-dimensional elasto-visco-plastic constitutive model to characterize asphalt mixes and predict rutting as a result of densification of the material under static creep loading. They decomposed the total strain into a recoverable part to reflect the elastic and visco-elastic component and a nonrecoverable part for the viscous and plastic portion. A frictional slider connected to Burger elements was used to account for the plastic deformation with the aid of a Drucker-Prager yield criterion. Perl et al. (1983) employed a repeated uniaxial creep experiment under constant compression stress and temperature to develop an elasto-visco-plastic constitutive model for bituminous mixtures. Plastic strain was found to depend on the number of load applications, while the visco-elastic component was governed by the power law of time. They showed experimentally that visco-elastic and visco-plastic strain components are linearly related to stress for a stress level less than 0.4 MPa.

Bonnier and Troost (1991) proposed that strains of asphalt mixtures be resolved into instantaneous elasticity, visco-elastic, and visco-plastic components. The model involved a first component of an elastic spring to account for the instantaneous response, a second component of a Kelvin-Voigt element used in the simulation of visco-elasticity, and a third element of a frictional slider and a dashpot in parallel used to symbolize the visco-plastic strain. A nonassociated flow rule with the power law yield function defined in the Perzyna formulation was employed to model visco-plasticity. They exploited three yield functions of Mohr-Coulomb for the three-dimensional presentation of the model. These functions were suitable for

compressive stresses where for tension they introduced another three yield surfaces. They implemented their model into FE and compared it to experimental measurements.

Lytton et al. (1993) developed a permanent deformation model based on a Vermeer yield surface (Vermeer 1984). This model was incorporated in FE to compute the stresses and permanent strains under one wheel. Lytton et al. (1993) proposed using the slope of the log ε^p- log N curve to compute the permanent strain at any number of load repetitions (N) once the permanent strain in the first cycle is calculated from the FE model.

Sousa et al. (1993) developed a nonlinear visco-elastic damage model to predict permanent deformation of HMA. The model included macro characteristic observations such as dilatancy under shear strain, the hydrostatic pressure effect on shear modulus, and accumulation of plastic strain under repetitive loading. They utilized a series of three-dimensional combinations of Maxwell elements composed of sets of springs and a dashpot. The springs captured the dilatancy and hardening phenomena, while temperature and rate dependency were captured by the dashpot. Damage was accounted for by including a damage parameter in the equilibrium equation for the dashpot and it was considered as a function on shear strain. A variety of experiments including the uniaxial strain, simple shear at constant height, volumetric simple shear frequency, and strain sweep tests were used to determine nonlinear elastic, viscous, and damage parameters.

In an attempt to characterize HMA behavior under cyclic loading, Sousa and Weissman (1995) improved the nonlinear visco-elastic model developed previously by Sousa et al. (1993) by including an elastoplastic component using the associated J_2-plasticity (von Mises yield surface) with isotropic and kinematic hardening. They assumed that aggregate response is rate independent that dilates elastically under shear loading. Their conclusion was to employ a rate-independent elasto-plastic constitutive law to model HMA. Nonlinear elastic response that couples volumetric and deviatoric response was used. Their model accounted also for shear hardening under hydrostatic pressure and provided different elastic responses under tensile and compressive load applications.

In a different attempt to provide a phenomenological approach for materials that exhibit plastic and creep deformation, Scarpas et al. (1997a) decomposed total strain into elastic and visco-plastic components. Scarpas et al. (1997a) integrated Desai's yield surface and Perzyna's visco-plasticity formulation for simulating and studying the initiation and development of pavement distresses under various loading conditions. They used monotonic uniaxial compression and tension tests for evaluating model parameters related to path and rate-dependency characteristics and incremental creep tests to identify hardening and viscous parameters. They indicated that conventional Perzyna's visco-plasticity can be applied only for simulating the primary creep and secondary creep phases. They concluded that degradation of the material under triaxial stresses is caused predominantly by the nucleation, localization, and eventual propagation of splitting cracks along planes perpendicular to the maximum principal tensile stresses. Their model considered the damage evolution associated with material degradation and temperature effects in determining ultimate strength. In addition, the model accounted for material dilation under deviatoric stress, hardening, and crack evolution by determining the fracture energy.

Lu and Wright (1998) introduced a numerical approach for developing an elasto-visco-plastic

constitutive model assuming that material response is decomposed into elasticity, visco-elasticity, and visco-plasticity. Hooke's law was used to model the elastic component; a power law function of stress and time was used to model the visco-elastic component; and Perzyna's theory of visco-plasticity was utilized to model the visco-plastic component. Lu and Wright (1998) took the hardening parameter to be equal to zero while the viscosity parameter in Perzyna's theory was taken to change with time. The model parameters were determined using repetitive loading. The study also adapted the constitutive model in a numerical formulation to be implemented in FE analysis.

Seibi et al. (2001) developed an elasto-visco-plastic constitutive model for HMA under high rates of loading using uniaxial and triaxial compression experiments with different temperatures. They noticed that yielding stress is increased by increasing both strain rate and temperature. They utilized the Drucker-Prager yield surface and Perzyna's theory of visco-plasticity for isotropic work hardening and strain rate sensitive materials to describe the stress-strain behavior of HMA. They concluded that rate dependency of the material is governed mainly by visco-plastic response and is more prominent in the plastic range.

Huang et al. (2002) implemented the visco-plastic constitutive model developed by Desai et al. (e.g., Desai et al. 1986; Desai and Zhang 1987), which incorporates temperature and loading rate effect into a Hierarchical Single surface (HISS) plasticity-based model. The yield surface of the HISS model incorporated the first invariant of stress, J_1, and the second and third invariant of deviatoric stress, J_2 and J_3, respectively:

$$F = \frac{J_2}{P_a^2} - F_b \cdot F_s = 0 \tag{2-2}$$

in which

$$F_b = -\alpha_{ps}\left(\frac{J_1}{P_a}\right)^n - \gamma\left(\frac{J_1}{P_a}\right)^2$$

$$F_s = \left(1 - \beta \cdot cos\,3\theta\right)^{-m} \tag{2-3}$$

$$cos\,3\theta = \frac{3\sqrt{3}}{2} \cdot \frac{J_3}{J_2^{3/2}}$$

where P_a is the atmospheric pressure; α_{ps} is the hardening of growth function; and α_{ps}, β, γ, m and n are material parameters defining the yield surface. HISS models are elasto-plastic constitutive relationships that share the same yield function. Huang et al. (2002) modified the HISS model to account for temperature effects in the form of:

$$F = F\left(\sigma_{ij}, \alpha, \theta\right) \tag{2-4}$$

where σ_{ij} is the stress tensor component, α is the hardening function, and θ is the temperature. They used Perzyna's visco-plasticity postulate modified with the temperature effect to model the visco-plastic component. Creep tests were conducted to obtain viscous properties, while conventional triaxial tests were used to calibrate thermo-plastic parameters.

Chehab et al. (2003) proposed a constitutive model by incorporating damage, rate of loading, and the temperature effects. They decomposed their model to visco-elastic and visco-plastic components and developed a separate model for each component then combined them to develop a single elasto-visco-plastic model. All model parameters were determined using different testing modes in uniaxial tension tests. Their model was able to detect the material response before the localization point, while at the post-localization zone to capture material degradation they used fracture process zone strains measured using digital image correlation. The visco-elastic behavior was determined based on Shapery's continuum damage model, while an empirical strain hardening model was used to characterize the visco-plastic behavior. They concluded that the portion of visco-plastic strain with respect to visco-elastic strain increases as temperature increases and strain rate decreases.

Collop et al. (2003) developed an elasto-visco-plastic constitutive model that includes elastic, delayed elastic and visco-plastic components. Continuum damage mechanics were introduced to account for the damage mechanism during viscous flow. They implemented the model in an incremental formulation into a FE program with the aid of a local strain compatibility condition to explicitly find the incremental stresses and the incremental strains at each integration point.

Gibson et al. (2004) and Schwartz et al. (2004) developed a constitutive model based on an extended form of the Schapery continuum damage formulation (Schapery 1999). The model considered the visco-elastic (including instantaneous elastic), visco-plastic (including instantaneous plastic), and nonlinear visco-elastic damage components in a uniaxial unconfined compression tests. Their study focused on the visco-plastic response component at intermediate and high temperatures. By using the concept of time-temperature superposition for visco-plastic response, they extracted the visco-plastic material parameters from uniform load creep and recovery tests. The approach used to model the visco-plastic component is similar to that of Chehab et al. (2003). Compression tests were conducted by Schwartz et al. (2004) to determine the model parameters. They found that confinement suppressed visco-plasticity and increase nonlinearity of the hardening behavior while no change in damage was recorded.

Oeser and Moller (2004) presented a study to develop a three-dimensional rheological model. A one-dimensional formulation was adopted and it was further extended to three-dimensional using an energy hypothesis and a special yield function that consisted of Von Mises in the tension zone and Drucker-Prager in the compression zone. A combined Hook-Kelvin-Newton element was employed to account for elastic, visco-elastic, and visco-plastic components, respectively. With the use of nonmonotonic loading, they adopted a damage-healing element to account for damage and healing behavior resulting from dynamic loading. They emphasized that tertiary creep in a loading cycle is composed of a positive loading phase, which is considered as a damage stage, followed by a healing phase if negative stress is applied, and as the cycle repeats, the damage stage is rebound. Their model accounted for temperature effects, but it was applicable only to small deformation. They converted the model into a differential form in a numerical algorithm to be implemented in a computational model.

Tashman (2003) developed a nonassociated microstructural visco-plastic model for HMA. The model accounted for microstructure characteristics like particle orientation, damage evolution as a result of air voids, and nucleation of microcracks, work hardening, and dilation in the material

response. The study considered anisotropy by modifying the stress formulation with a microstructure fabric that is a function of vector magnitude. Damage and work hardening were taken as a function of effective visco-plastic strain. The study concluded that a nonassociated flow rule is essential to model the dilation response of the material.

The advantage of continuum models is their computational simplicity, and once the material properties are known, simulations of material deformation under static or dynamic loading can be easily implemented in FE analysis to predict HMA performance.

Bonnier and Troost (1991) employed FE analysis to compare the performance of their elastic-visco-elastic model with a closed-form semi analytical solution of a two-layered system loaded with a constant circular load. Sousa et al. (1993) implemented their constitutive model into a FE program to simulate a boundary value problem of a pavement lane. A repetitive haversine load defined in plane strain configuration was used to simulate slow moving traffic. Lu and Wright (1998) adapted their constitutive model into numerical form to find the response of HMA using FE analysis under different loading conditions. Lu and Wright (1998) used a step-by-step time integration approach with a Newton-Raphson iteration procedure to determine strain in the constitutive equation. As a result, an increment form of stress and strain was obtained in time-step control. Papagiannakis et al. (2002) is an example of a study that related the microstructure of HMA to its visco-elastic behavior. They used FE analysis to model the material stress-strain relationship in the time domain. They employed a user subroutine associated with FE analysis to account for the nonlinearity of the material.

Although most analytical methods assume two-dimensional axisymmetric conditions, Zaghloul and White (1993), Scarpas et al. (1997a), Seibi et al. (2001), Collop et al. (2003) and Oeser and Moller (2004) applied three-dimensional FE analyses to simulate realistic traffic loads. Zaghloul and White (1993) used a visco-elastic model for HMA, an extended Drucker-Prager model for the granular base course, and a Cam Clay model for clay subgrade soils. Scarpas et al. (1997a) utilized FE analysis to investigate the dynamic nonlinear response of HMA. They simulated the pavement system by using two different subgrade layers that differed in strength. Seibi et al. (2001) extended the uniaxial visco-plastic model to a multiaxial case by using a pavement structure simulation and FE to determine material parameters.

Collop et al. (2003) used FE to demonstrate the capability of an elasto-visco-plastic model to simulate field conditions. Elastic material properties were used for all pavement layers except the HMA. Load simulations were equivalent to dynamic configurations with loading and unloading cycles. They demonstrated a numerical algorithm to evaluate stress and strain in their constitutive relationship. They used a local strain compatibility condition such that the incremental stresses were determined explicitly from the incremental strains at each integration point.

Erkens et al. (2002) developed a constitutive model to account for the strain rate and temperature effects on HMA. They utilized the model to simulate the response of a pavement system by imposing three-dimensional stress conditions in the FE formulations. The FE model was used also to investigate damage development under repeated loading conditions in different pavement systems. Erkens et al. (2002) used nonlinear Newton-Raphson methodology to evaluate incremental

volumetric and deviatoric plastic strain. The updated stress was computed by means of a trial stress and stress correction.

However, in continuum approach, when describing the material response using a single set of material properties, only stress-strain at the boundaries is known but not the exact distribution along different locations within the material. Detailed information about particular features such as initial distribution of the microstructure and evolution of its macroscopic behavior is thus lost. Heterogeneous multiphase of HMA is complicated by nature, and classical continuum mechanics are not able to address the significance of this nature into macroscopic response.

Micromechanical Approach

In contrast to the continuum approach, the micromechanical approach is being utilized to further predict HMA behavior under different loading conditions. Micromechanical models consider the microstructure distribution, properties of components, and interactions between aggregates and asphalt binder. Therefore, micromechanical models can include most of the important factors that govern the performance of HMA.

Careful review of the literature shows that significant progress has been made in laboratory investigations of the influence of HMA constituent properties on the macroscopic response. Morris et al. (1974), and Button et al. (1990) are examples of research that relates macroscopic mechanical behavior of HMA to its microscopic functions. These studies reflect the influence of a number of microscopic factors such as aggregate characteristic (size, shape, type, texture, and orientation), properties of binder, and concentration of aggregate, binder, and air voids in HMA.

An approach found in literature was to generate numerical representation of HMA microstructure. The representation is used to study interactions between different constituents and their influence on macroscopic properties. Two methods were used to simulate microstructure, the discrete element method (DEM), and the FE method.

DEM analyzes particulate systems by modeling the translational and rotational response of particles by applying Newton's second law to particle-particle contact forces. The method is used to simulate interactions of individual particles in a matrix medium. Rothenburg et al. (1992) proposed a micromechanical discrete model of HMA. In this model, HMA was represented by a set of discrete elastic elements bounded by a linearly visco-elastic binder, and the binder within voids was treated as a compressible Newtonian fluid. Chang and Meegoda (1997) used DEM to simulate the interaction between idealized representations of elastic aggregates and a visco-elastic asphalt binder. Buttlar and You (2001) utilized the DEM to study the behavior of HMA in indirect tension test.

On other hand, FE analysis with different constitutive models for the individual constituents has been used to analyze HMA microstructure (e.g., Sepehr et al. 1994, Weissman et al. 1999; Kose et al. 2000; Masad et al. 2001; Papagiannakis et al. 2002). In these models, the microstructure was either assumed to exhibit some idealized distribution or was captured through photographic and X-ray computed tomography imaging techniques. These studies showed that FE analysis is useful in providing information on stress and strain distribution within the microstructure. Masad and Somadevan (2002) calculated strain distribution within the microstructure and compared it to

experimental measurements of strain distribution using image correlation techniques. Papagiannakis et al. (2002) used FE analysis in addition to the image processing to simulate HMA microstructure visco-elastic stress-strain behavior in the time domain.

In summary, micromechanical models directly consider the characteristics of the microstructure geometry, such as aggregate size effect, and nature, such as contact evolution, interlocking, and localization in modeling HMA. They also explicitly provide information on the influence of changes in the microstructure on material response when the material undergoes deformation. This approach, however, has not been able to realistically simulate the actual geometry of material microstructure or the interaction among the constituents. This approach is valuable in relating microstructure properties to macroscopic response; however, it consumes tremendous computing time, for which it has not been applicable and reliable for performance prediction models.

THEORETICAL BACKGROUND ON PLASTICITY

Theory of plasticity deals with two equally important aspects; first, the general technique used in developing stress-strain relationships with work hardening/softening to define real material behavior; and second, the general numerical solution for solving a material problem under the action of loads and/or displacements.

The first task of the theory is to establish an adequate relationship between stress and strain to describe the linear and nonlinear deformation of the material. The second task concerns with the development of numerical technique for implementing the relationship between the stress and strain. Because of the nonlinear nature of HMA deformation, solutions may inevitably present considerable difficulties. However, development of computers and modern techniques of FE analysis have provided powerful tools for solving nonlinear problems.

In classical plasticity, models contain three fundamental ingredients (Chen and Han 1988):

- A yield function or yield criterion defines the limit of elastic behavior for a general state of stress. In visco-plasticity, the term "flow surface" or "overstress function" is used instead of yield surface,

- A flow rule determines the relative magnitudes of the components of the plastic strain increment tensor,

- A hardening rule defines the changes in the yield function as a result of plastic straining.

Each ingredient is discussed briefly in the next section with the focus on the Drucker-Prager yield function, since it is the basis for developing the visco-plastic model presented in this study.

Drucker-Prager Yield Surface

If there is a continuous function $f(\sigma,\varepsilon,\kappa)$ such that there is a region that satisfies the condition $f(\sigma,\varepsilon,\kappa)<0$ in the stress space, then this region constitutes the elastic range. On other hand, the condition $f(\sigma,\varepsilon,\kappa)=0$ defines the yield surface in this stress space, and the orientation of

this surface is defined by the elastic range that outlines its interior (Lubliner 1991). The yield surface may be written as a function of stress and a hardening parameter. Experimental results showed that the plastic yield surface is affected by shear stresses or normal stresses or a combination of both. One well-known yield surfaces is the one proposed by Drucker-Prager. A three-dimensional yield surface is shown in Fig. 2.3. (Drucker and Prager 1952)

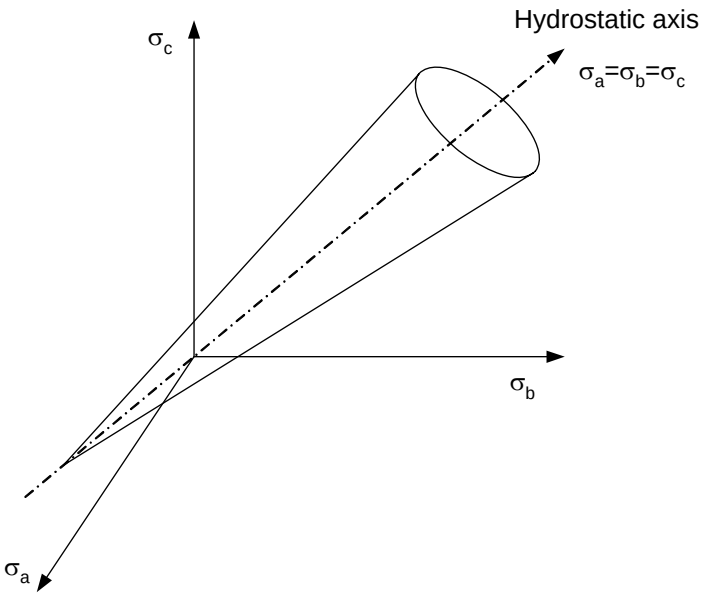

Figure 2.3. Three-Dimensional Diagram of the Linear Drucker-Prager Yield Surface.

The Drucker-Prager yield surface can be described by the general expression in Eq. (2-5):

$$f = F(J_2, \mathrm{I}_1, \alpha) - \kappa \qquad (2\text{-}5)$$

where I_1 and J_2 are the first stress invariant and the second deviatoric stress invariant, respectively and α and κ are material parameters: the first reflects the frictional potential of the material, while the second reflects the material hardening.

Abdulshafi and Majidzadeh (1985), Seibi et al. (2001), Tashman (2003), and Oeser and Moller 2004 among others, are examples of work that used the Drucker-Prager yield function or modified versions of it to describe visco-plastic behavior in HMA. The advantages of using the Drucker-Prager over other models are summarized as follows:

- The yield surface is continuous and smooth, and hence does not have sharp edges;
- The model allows for initiation of dilation in terms of plastic strain before reaching the ultimate stress;
- The model expresses the hardening rule as a function of plastic strain;

- The model incorporates the main terms to account for the plastic deformation; behavior of the material, and the hydrostatic and deviatoric stress; and

- The model incorporates factors to account for nonassociative behavior.

Associated and Nonassociated Flow Rules

Experimental evidence from tests on granular materials has clearly indicated that use of the associated flow rule overestimates dilation or expansion. Many studies have shown that a nonassociative flow rule should be employed to characterize volume changes (e.g., Zeinkiewicz et al. 1975; Oda and Nakayama 1989). In the nonassociated response, another surface is associated with the deformation flow, called plastic potential surface. In general, plastic potential and yield surfaces can have similar form and hence they coincide, while for nonassociated flow the two families of surfaces cross each other.

Work Hardening and Strain Softening

Plastic deformation occurs in the HMA when the applied stress exceeds the yielding point. The stress-strain curve resulting from this load application in the plastic range is called the "flow curve". If the specimen is unloaded after some plastic deformation has taken place and then reloaded a new and higher yield stress is attained. The material may be regarded as having been hardened due to plastic deformation in a process namely work hardening.

In the literature, the work hardening phenomenon is an important factor governing plastic deformation of HMA. In simple terms, the phenomenon occurs during plastic deformation of the material at a microscopic level due to the generation and changing interaction between constituents at the aggregate-aggregate and aggregate-binder interfaces as the degree of deformation increases.

Chen and Han (1988) reported two basic approaches that were utilized to develop constitutive equations for work hardening materials. First is the deformation theory, which relates the total stress to total strain, and can be given in general form:

$$\varepsilon_{ij}^{p} = \varepsilon_{ij} - \varepsilon_{ij}^{e} = f\left(\sigma_{ij}\right) \qquad (2\text{-}6)$$

where σ_{ij} is the state of stress in which the plastic strain occurs. Despite its simplicity, the deformation theory could not describe hardening phenomena near the yield surface along the neutral loading path associated with loading/unloading. Second is the flow theory, which relates the plastic strain increment $d\varepsilon_{ij}^{p}$ to the state of stress σ_{ij} and the stress increment $d\sigma_{ij}$. As the stress increment increases gradually above the yield limit, a new yield surface is specified, called the subsequent yield surface, on which plastic deformation takes place. The hardening rule that applies for the post-yield response can be given in the form of:

$$\dot{\varepsilon}_{ij}^{p} = \dot{\gamma}\frac{\partial g}{\partial \sigma_{ij}} \tag{2-7}$$

where $\dot{\gamma}$ is a positive coefficient that is nonzero only when plastic deformation occurs. It represents the magnitude of the plastic strain increment due to the applied subsequent stress. The vector $\frac{\partial g}{\partial \sigma_{ij}}$ implies the direction of the plastic potential surface associated with the applied stress. *g* as a function of stress σ_{ij} defines a plastic potential surface that coincides with the yield surface function *f,* in which the hardening rule is called an associated flow rule. In this case, Eq. (2-7) is simplified to:

$$\dot{\varepsilon}_{ij}^{p} = \dot{\gamma}\frac{\partial f}{\partial \sigma_{ij}} \tag{2-8}$$

Visco-plasticity Formulation

Theories of plasticity and nonlinear elasticity improve the layered elastic solution but still fail to capture an important characteristic of pavement materials, which is the time dependency of plastic behavior under traffic loading. The theory of visco-plasticity has been chosen by many researchers as the most suitable constitutive framework for modeling the time-dependent response of HMA. The theory has emerged as an attempt to provide a realistic, unified, and phenomenological approach for modeling materials that exhibit both plastic and creep deformation.

A widely used visco-plastic formulation is the Perzyna model (Perzyna, 1966). The formulation preserves the fundamental of classical plasticity notions of yield surface, decomposition of strains, and hardening, and at the same time, it is well-appropriate for FE implementation.

The main feature of this formulation is that it introduces the concept of the "overstress" effect in which the yield function used for describing the visco-plastic strain can become larger than zero. Perzyna's original model assumed that visco-plastic strain can occur only when the stress state reaches the yield surface and that visco-plastic strain is not significant in the elastic zone below the yield surface. The direction of the visco-plastic strain is specified by an associated flow rule. The visco-plastic strain rate depends on the amount by which the effective stress exceeds the current static yield stress (overstress). In this model the yield surface does not change with time when the visco-plastic strain is held constant. In addition, the visco-plastic strain rate is zero when the overstress is zero (Lubliner 1991).

In the small-strain theory, the total strain rate $\dot{\varepsilon}$ in an elasto-visco-plastic material may be additively decomposed into an elastic component $\dot{\varepsilon}^{e}$ and a visco-plastic component $\dot{\varepsilon}^{vp}$ that accounts for both irreversible and viscous deformation:

$$\dot{\varepsilon} = \dot{\varepsilon}^{e} + \dot{\varepsilon}^{vp} \tag{2-9}$$

when using the elasticity principle it follows:

$$\dot{\sigma} = D\ \dot{\varepsilon}^{e} \tag{2-10}$$

where D is the fourth-order tangent elastic stiffness tensor. In the Perzyna model, evolution of the visco-plastic strain rate $\dot{\varepsilon}^{vp}$ is defined as (Perzyna 1966):

$$\dot{\varepsilon}^{vp} = \Gamma \cdot < \phi(f) > \cdot \frac{\partial g}{\partial \sigma} \tag{2-11}$$

where $\Gamma \cdot < \phi(f) >$ specifies the magnitude of $\dot{\varepsilon}^{vp}$. The second-order tensor $\frac{\partial g}{\partial \sigma}$ determines the direction of the visco-plastic strain rate, in which g is the visco-plastic potential function and σ is the stress tensor. Γ is a viscosity parameter, and ϕ is the overstress function that depends on the rate-independent yield surface $f(\sigma, \kappa)$.

Combining Eq. (2-7) and Eq. (2-11), the consistency parameter can be obtained as:

$$\dot{\gamma}^{vp} = \Gamma \cdot < \phi(f) > \tag{2-12}$$

In Eq. (2-12), "$< \cdot >$" are McCauley brackets, such that:

$$< \phi(f) > = \begin{Bmatrix} 0, & \phi(f) \le 0 \\ \phi(f), & \phi(f) > 0 \end{Bmatrix} \tag{2-13}$$

CHAPTER III

FINITE ELEMENT ANALYSIS OF HOT MIX ASPHALT MICROSTRUCTURE USING EFFECTIVE LOCAL MATERIAL PROPERTIES AND STRAIN GRADIENT ELASTICITY [*]

INTRODUCTION

Asphalt mixes are particulate composite materials that consist of asphalt binder, particles, and air voids. There has been long-term interest in relating the macroscopic response of hot mix asphalt (HMA) to the properties of the constituents. This has been done mainly through laboratory investigations that relate mechanical behavior of asphalt mixes to aggregate characteristics, binder type and content, and percent of air voids (e.g., Monismith 1992).

Analytical studies based on micromechanics concepts, have been used to estimate HMA effective material properties. The first micromechanics model was proposed by Van der Poel (1954) based on the analysis of a concentrated suspension of rigid spheres in an elastic matrix. Another attempt to model the viscous behavior of asphalt mixes was reported by Hills (1973). He described the internal structure of HMA in terms of asphalt film thickness and the evolution of this state variable as a function of macroscopic straining of the material.

[*] Material in this chapter is printed with permission from "Finite element analysis of hot mix asphalt microstructure using effective local material properties and strain gradient elasticity." by Dessouky, S., Masad, E., Little, D., and Zbib, H. *Journal of Engineering Mechanics*, by American Society of Civil Engineers (ASCE). Accepted but not yet appeared

Classical micromechanical models, developed to estimate the effective properties of random particulate composites, have been found to underestimate the elastic properties of HMA (Deshpande 1995). This underestimation is due to high volume fraction of particulates in HMA; such that the interaction among these particulates is an important factor that is not taken into account by these micromechanical models. In addition, effective material properties are not sufficient representation of HMA response, as it averages fluctuations in stress and strain distributions caused by the wide range of particle sizes and the several orders of magnitude differences in stiffness between the constituents (Masad et al. 2001). The local distribution and spatial fluctuations of these stresses and strains are important factors that influence the overall mix response, especially at the microscopic level (e.g., Kose et al. 2000; Masad and Somadevan 2002; Masad et al. 2001). As stated by Graham and Baxter (2001), assuming homogeneous response of a composite material represented only by effective properties ignores the local microscopic response often associated with failure phenomena.

Numerical simulations of the microstructure response have been used to study interactions between different HMA constituents and their influence on localized microstructure response and macroscopic properties. Rothenburg at al. (1992), Chang and Meegoda (1997), Deshpande and Cebon (1999), and Buttlar and You (2001) are examples of work that used discrete element method (DEM) to simulate the microstructure of HMA, while Bahia et al. (1999), Weissman et al. (1999),

Kose et al. (2000), Abbas et al. (2001), and Masad and Somadevan (2002) are examples of studies that focused on using FE analysis to achieve this approach.

DEM analyzes particulate systems by modeling the translational and rotational behavior of each particle by applying Newton's second law to particle-particle contact forces. In DEM studies, aggregates are represented by a set of discrete elastic particles and their interactions are controlled by the mechanical properties of an elastic or visco-elastic asphalt film.

FE analysis with different constitutive models for the individual constituents has been used to analyze HMA microstructure (e.g., Weissman et al. 1999; Kose et al. 2000; Masad et al. 2001; Papagiannakis et al. 2002). These studies have shown that FE analysis is appropriate in providing information on the stress and strain distribution within the microstructure. However, this approach was found, due to experimental and computational limitations, to underestimate the effective properties of the HMA and the results can be mesh size dependent (e.g., Abbas et al. 2001; Masad and Somadevan 2002).

This chapter presents a methodology for the analysis of HMA microstructure using FE analysis. This methodology offers two main contributions. The first is using strain gradient elasticity in modeling material behavior. Strain gradient theories or nonlocal theories have been implemented in different constitutive models to introduce an internal length scale in the standard equations of continuum mechanics (e.g., Aifantis 1984, 1987; Zbib and Aifantis 1989, and 1992). Therefore, it is believed that using a strain gradient theory will assist in capturing the differences among mixes due to different particle and asphalt film size distributions, and reducing the effect of FE mesh resolution on the microscopic and macroscopic response. The gradient coefficients, which are directly related to the material characteristic length scale, are determined by analyzing the microstructure distribution using the autocorrelation function and the moving window technique.

The second contribution in this study is using a micromechanical model along with the moving window technique to calculate the local effective material properties used in the FE analysis. These calculations are supported by experimental measurements of the stiffness of HMA.

MICROSTRUCTURE FE ANALYSIS USING EFFECTIVE MATERIAL PROPERTIES

This section discusses the development of a FE analysis of HMA microstructure using effective local material properties. FE implementation of gradient elasticity is presented first, followed by the procedures used to determine the effective local material properties using micromechanics principles.

FE Implementation of Gradient Elasticity

Generalization of elasticity theory by incorporating the effect of higher gradients of the displacement field into the strain energy density function was studied by Cosserat and Cosserat (1909). A modern systematic treatment of gradient elasticity was given by Truesdell and Toupin

(1960). Subsequently, it was extended by Toupin (1962), Green and Rivlin (1964), and Mindlin (1965). They implemented the higher gradients of the displacement field to higher order stresses instead of directly introducing higher gradients into the constitutive equation. The gradient approach is typically employed to provide the standard equations of solid mechanics with a characteristic internal length scale. In this study, the feature of gradient elasticity (i.e., internal length scale) is being utilized to capture the differences in mechanical response among mixes with different particle size distributions and to reduce the influence of mesh size on this response.

Assuming that the elastic strain at a position vector x depends linearly on the relative strain with respect to an element movement from x to r, which occurs in a small but finite material volume V surrounding x. The average strain can be obtained by the volume average of the local strain distribution within the representative volume element (RVE) as follows:

$$\bar{\boldsymbol{\varepsilon}} = \frac{1}{V}\int_{V_{Ref}} \boldsymbol{\varepsilon}(x-r)dV \tag{3-1}$$

The Taylor's series expansion limited to the second-order term of the function $\varepsilon(x-r)$ around x gives (Zbib and Aifantis 1989):

$$\bar{\boldsymbol{\varepsilon}} = \boldsymbol{\varepsilon}(x) + l_c^2 \nabla^2 \boldsymbol{\varepsilon} \tag{3-2}$$

where l_c is a characteristic length scale of the material microstructure. The following gradient elasticity model is obtained when Eq. (3-2) is substituted in Hooke's law:

$$\boldsymbol{\sigma} = \boldsymbol{A}\boldsymbol{\varepsilon} + l_c^2 \boldsymbol{A}\nabla^2 \boldsymbol{\varepsilon} \tag{3-3}$$

where $\boldsymbol{\sigma}$ and $\boldsymbol{\varepsilon}$ are the stress and strain tensors, respectively, and $\boldsymbol{A}$ is the fourth-order elasticity tensor. Following standard FE formulation, e.g., the Galerkin's method, the equation of equilibrium can be written in the weak form:

$$\int_V grad\,[N]\boldsymbol{\sigma}\, dV = \int_S [N](\boldsymbol{\sigma}\cdot n)dS \tag{3-4}$$

where $[N]$ is a matrix containing the shape functions and n is a unit vector normal to the surface. By substituting Hooke's formula in Eq. (3-3) into Eq. (3-4) and noting that the right-hand side of the equation is the surface traction f^s, one obtains

$$\int_V [B]^T \boldsymbol{A}[B]u dV + l_c^2 \int_V [B]\boldsymbol{A}\nabla^2 \boldsymbol{\varepsilon}\, dV = f^s \tag{3-5}$$

where u is a displacement vector and $[B]$, the strain displacement matrix, is a first derivative of $[N]$. Rearranging the equation and considering the gradient term as a body force, Eq. (3-5) can be written as follows:

$$[K]u = f^s - l_c^2 \int_V [B] \boldsymbol{A} \nabla^2 \varepsilon \, dV \tag{3-6}$$

where $[K]$ is the global stiffness matrix and the term includes the strain gradient is defined as body force vector f^b.

A numerical scheme is used to evaluate the strain gradient at every integration point. The gradient quantity depends on the strain values at this point and the neighboring points. Also it depends inversely on the distance between the center point and the neighboring points. Consider a plane strain element that contains the points *A*, *P*, *B*, and *Q* at distances of *ah*, *ph*, *bh*, and *qh* from the center integration point *O*, respectively. *h* is a fixed distance, and *a*, *p*, *b*, and q are constant multipliers. *A* and *P* are in the x-direction and *B* and *Q* are in the y-direction. The expansion of strain at points *A* and *P*, for example, is given by:

$$\begin{aligned} \varepsilon_A &= \varepsilon_o + ah\frac{\partial \varepsilon_o}{\partial x} + \frac{1}{2}(ah)^2 \frac{\partial^2 \varepsilon_o}{\partial x^2} + ... \\ \varepsilon_P &= \varepsilon_o + ph\frac{\partial \varepsilon_o}{\partial x} + \frac{1}{2}(ph)^2 \frac{\partial^2 \varepsilon_o}{\partial x^2} + ... \end{aligned} \tag{3-7}$$

By disregarding the odd order terms and the higher terms, the second-order derivatives become:

$$\frac{\partial^2 \varepsilon_o}{\partial x^2} \cong \frac{2}{h^2}\left[\frac{\varepsilon_A}{a(a+p)} + \frac{\varepsilon_p}{p(a+p)} - \frac{1}{ap}\varepsilon_o\right] \tag{3-8}$$

$$\frac{\partial^2 \varepsilon_o}{\partial y^2} \cong \frac{2}{h^2}\left[\frac{\varepsilon_B}{b(b+q)} + \frac{\varepsilon_Q}{b(b+q)} - \frac{1}{bq}\varepsilon_o\right] \tag{3-9}$$

and the gradient is the summation of the second order derivatives in both directions as follows:

$$\begin{aligned} \nabla^2 \varepsilon_o &= \frac{\partial^2 \varepsilon_o}{\partial x^2} + \frac{\partial^2 \varepsilon_o}{\partial y^2} \\ \nabla^2 \varepsilon_o &= \frac{2}{h^2}\left[\frac{\varepsilon_A}{a(a+p)} + \frac{\varepsilon_B}{b(b+q)} + \frac{\varepsilon_p}{p(a+p)} + \frac{\varepsilon_Q}{b(b+q)} - \frac{(ap+bq)}{abpq}\varepsilon_o\right] \end{aligned} \tag{3-10}$$

For the boundary elements where there are no adjacent elements in the free side, the gradient is calculated using only the available values of strain while the other components drop out. Eq. (3-10) is applied to the various strain components in plane strain and is used to calculate the average strain gradient $\nabla^2 \varepsilon = [\nabla^2 \varepsilon_{11} \;\; \nabla^2 \varepsilon_{22} \;\; \nabla^2 \varepsilon_{12}]$ for each integration point within the element. This gradient is used in the second term of the right-hand side of Eq. (3-6) to evaluate the body forces.

In FE analysis, the first iteration (indicated by superscript ^{o}) does not include the effect of the strain gradients (body force = 0). In the following iteration i, the average strain gradient is computed and substituted in Eq. (3-6) to evaluate the body forces after assigning l_c. The body forces (strain gradient effects) in the second iteration will provide different displacements u^i than the ones calculated in the first iteration. In each iteration, the body forces determined at the integration points are averaged and transferred to the nearest nodes. This iterative procedure is repeated until convergence is achieved if the change in displacement becomes less than tolerance value of 1.0E-8. A flow chart illustrating the FE implementation of gradient elasticity is given in Fig. 3.1.

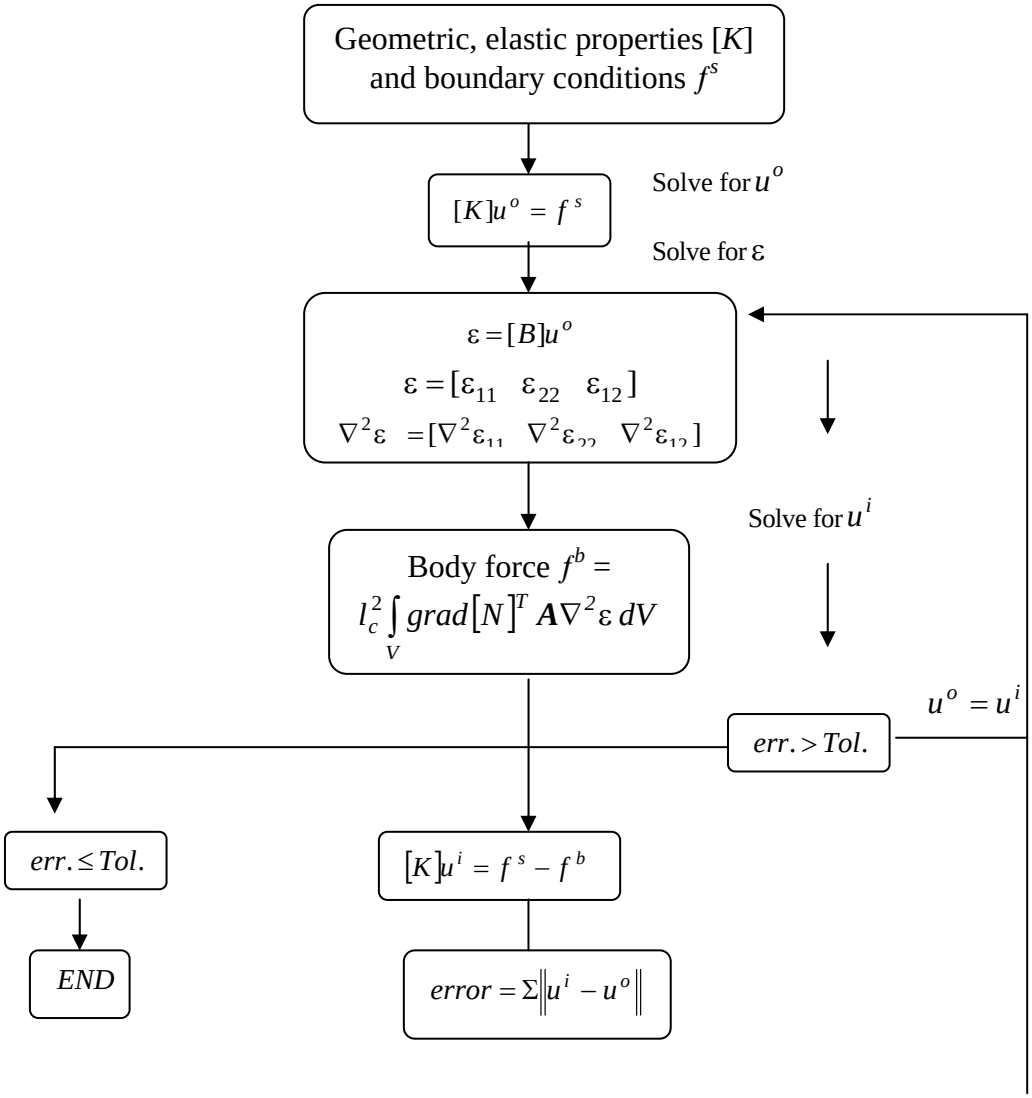

Figure 3.1. Flow Chart Illustrating the FE Algorithm.

The advantages of using strain gradient elasticity is illustrated here with the aid of an idealized plane strain model of a binder film between two blocks representing aggregates, as illustrated in Fig. 3.2. The 5-inch square model is subjected to a uniaxial pressure (P = 2.5 MPa) on the top, and the bottom is fixed in the horizontal and vertical directions. The aggregate blocks are modeled using Young's modulus = 25 GPa and Poisson's ratio = 0.25. The binder film is modeled with Young's modulus = 30 MPa and Poisson's ratio = 0.49. The idealized model is used to explore the relationship between element size and computed strain distribution. This is done by using 10×10, 30×30, 50×50. and 100×100 plane strain elements to represent the model in Fig. 3.2. Assuming that the finest mesh converges to the accurate solution, the value of l_c as shown in Fig. 3.3 is selected according to mesh size resolution. The results in Fig. 3.3 show that reducing the number of elements without including the strain gradient terms causes a reduction in the strain magnitude. However, when higher l_c values are assigned for finer meshes, all models converges to the same strain. This demonstrates that l_c reflects the influence of length scale (i.e., the mesh resolution with respect to the microstructure geometry) on the finite element results (see Fig. 3.3). It is worth mentioning that the computation time was not influenced by the gradient effect and the overall time was extremely small because the FE problem is still two-dimensional.

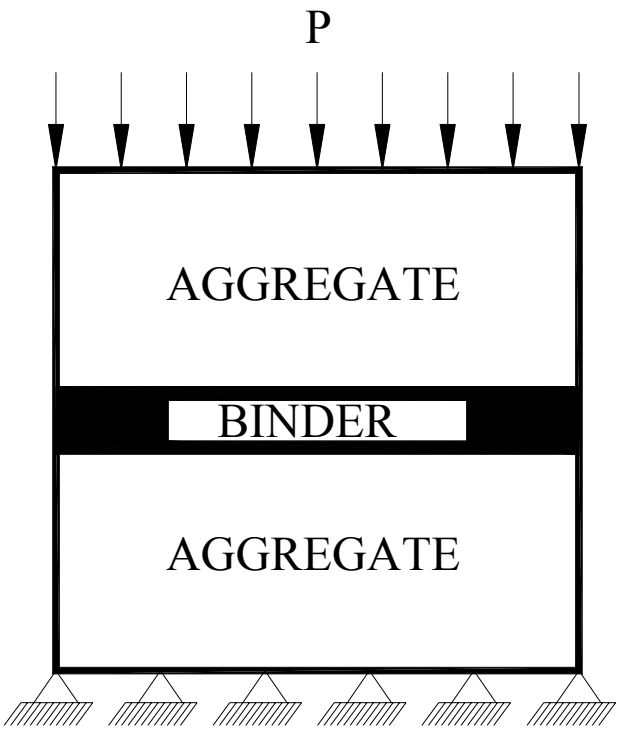

Figure 3.2. Illustration of the Idealized Model.

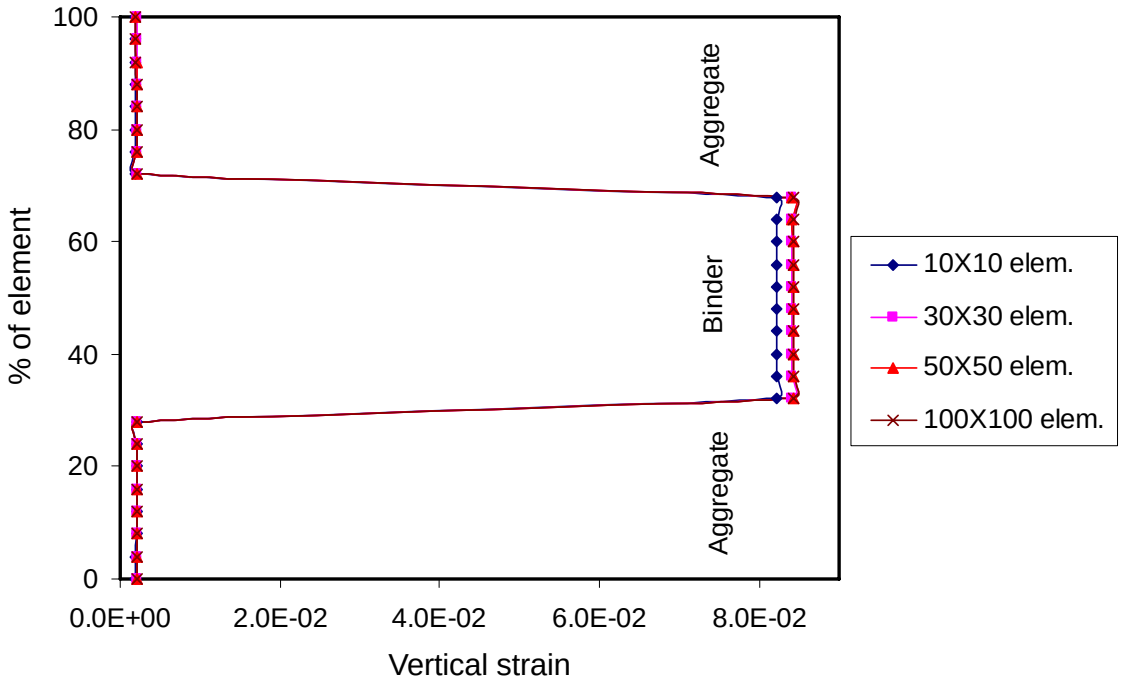

a) No strain gradient effect

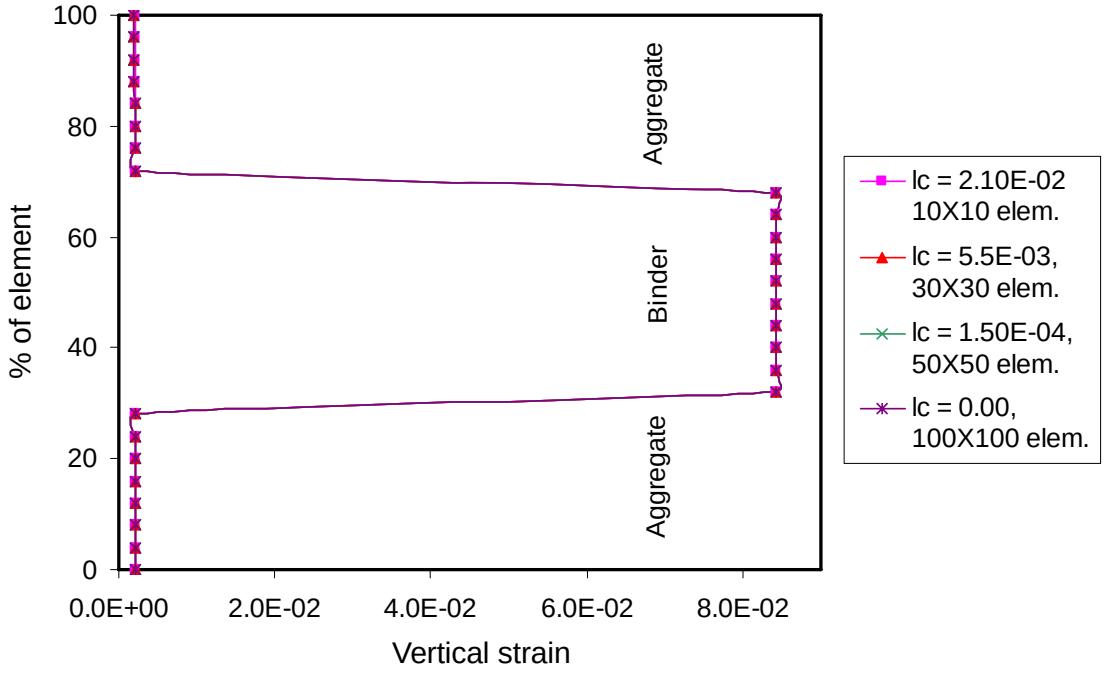

b) With strain gradient effect

Figure 3.3. Vertical Strain Distribution for the Idealized Model.

Similar to the model in Fig. 3.2, idealized microstructure representations of HMA with different particle sizes randomly dispersed in a matrix of asphalt binder at volume concentrations of 30%, 40%, and 50% with l_c values of 1.50 mm for fine and 5.5 mm for coarse, are used to examine the sensitivity of strain distribution to particle size and concentration. The values of the l_c is taking as a fraction of the average length of particles diameters. 50×50 plane strain elements with similar material properties of the constituents to those used in Fig. 3.2 are used. By recording vertical deformation due to the uniaxial load, results in Fig. 3.4a show that macroscopic (continuum) strains are not sensitive to particle size. However, sensitivity to particle size is significantly increased by using different l_c and strain gradients as shown in Fig. 3.4b.

The presence of fine particles is expected to produce more uniform strain distribution within the microstructure. Fig. 3.5 shows the strain distribution within the microstructure in which the ordinate gives the percent of elements that has a strain value equal to the corresponding magnitude on the x-axis.

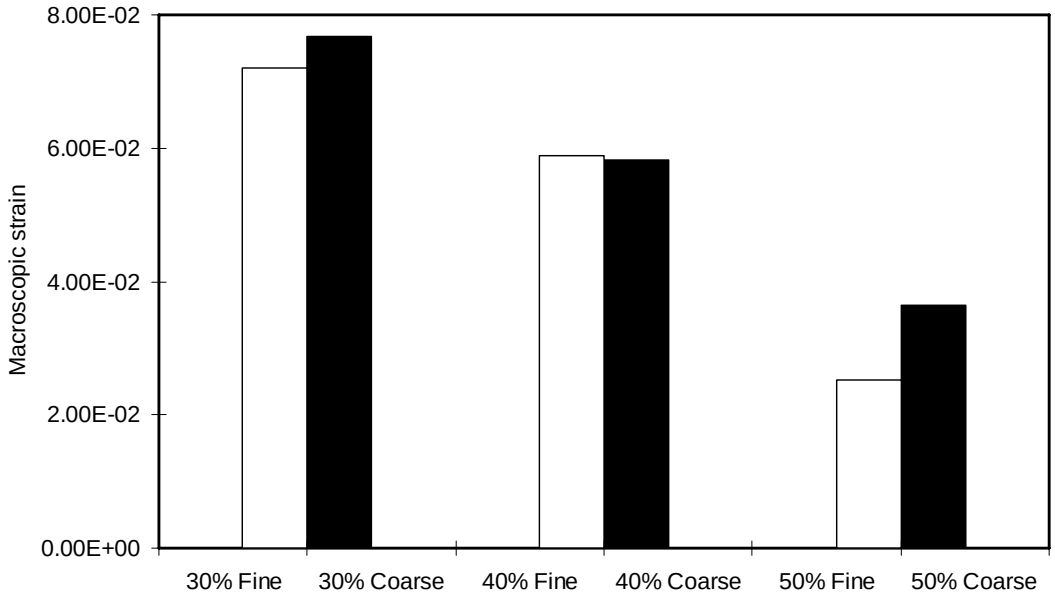

a) No strain gradient effect

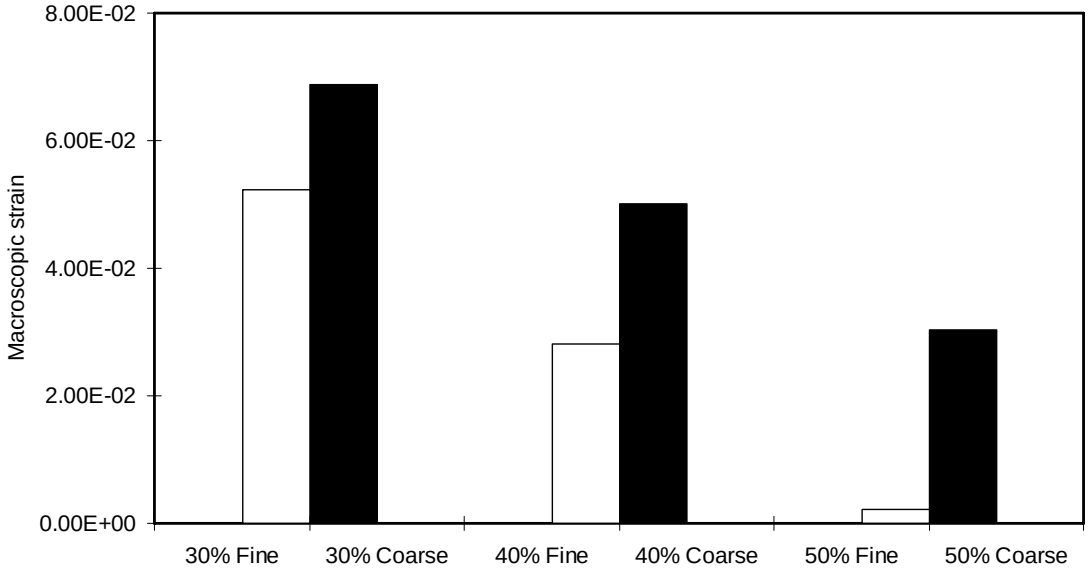

b) With strain gradient effect

Figure 3.4. Macroscopic Strain for Media with Different Percentages and Sizes of Particles.

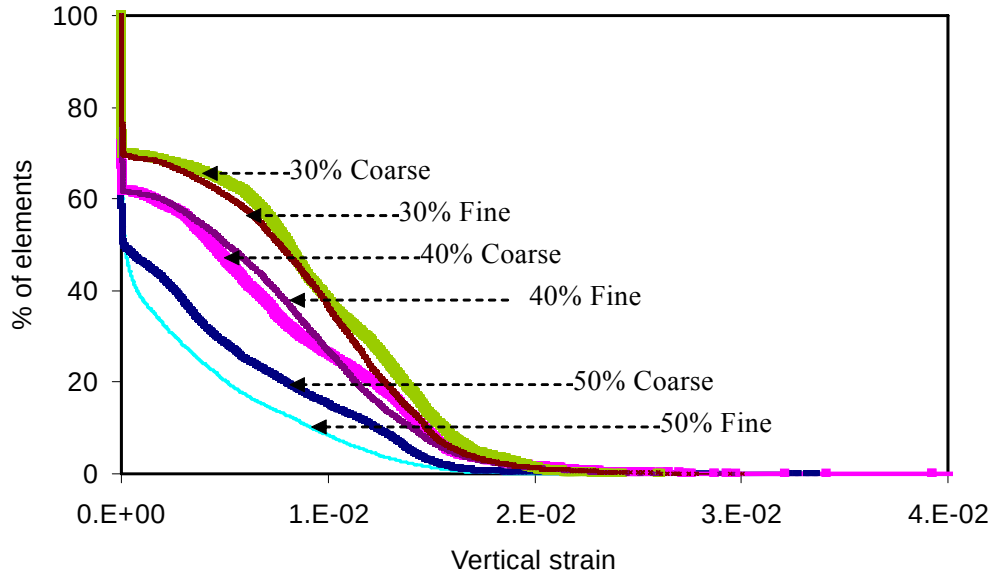

a) No strain gradient effect

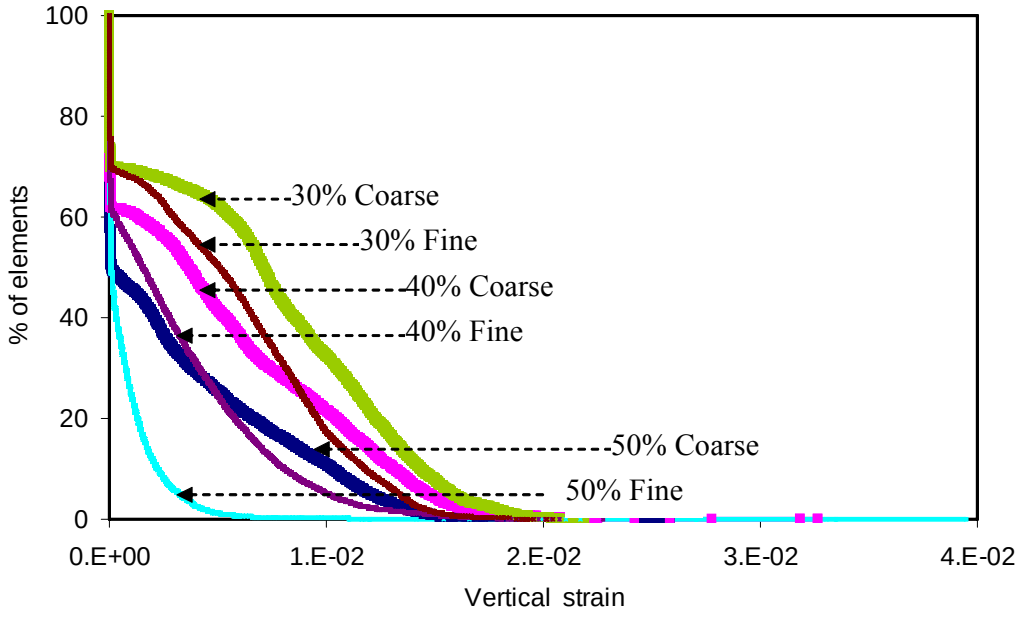

(b) With strain gradient effect

Figure 3.5. Microscopic Strain Distributions for Media with Different Percentages and Sizes of Particles.

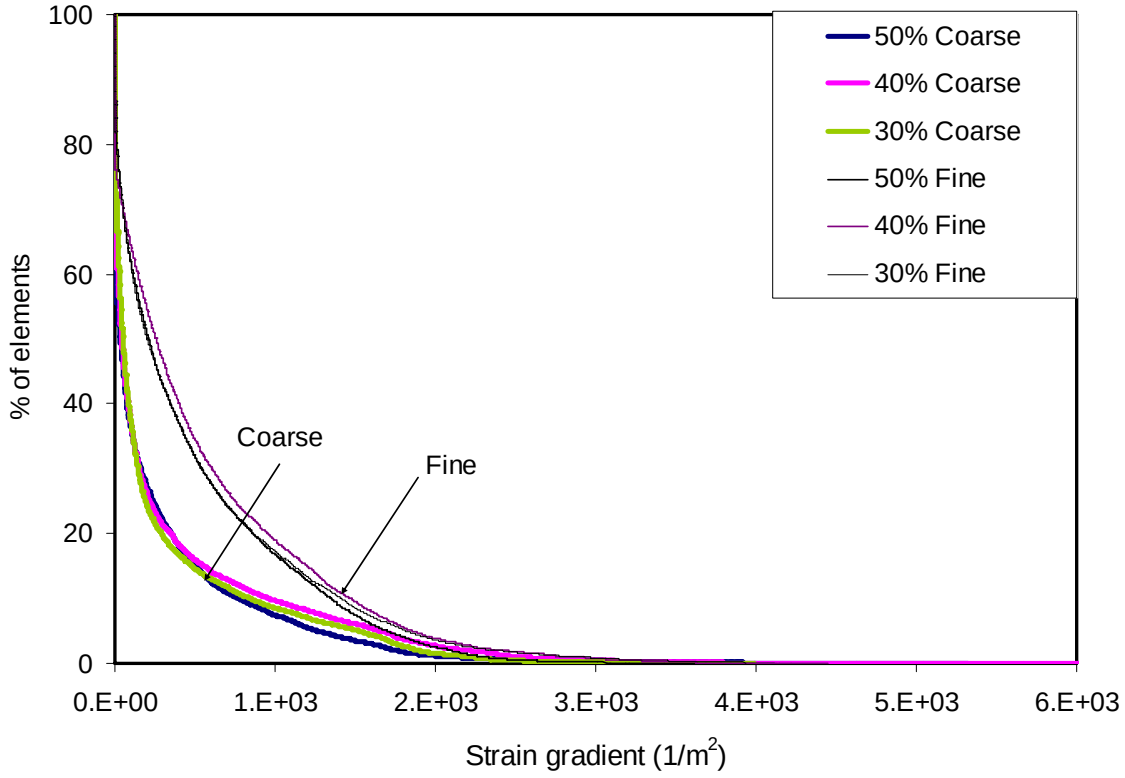

Figure 3.6. Strain Gradient for Different Media of Fine and Coarse Particles.

It is interesting to note in Fig. 3.5(a) that the effect of particle size on microstructure distribution is very small. The FE analysis becomes capable of capturing the difference in microstructure strain distributions when strain gradients and different l_c values are used for the fine and coarse media (Fig. 3.5b). The strain gradient distributions in the coarse and fine media are shown in Fig. 3.6.

An image of the HMA microstructure is usually limited, due to image resolution and experimental constraints, in capturing all fine particles present in a mix (e.g., Masad et al. 2001; Papagiannakis et al. 2002). Typically, the stiffening effect of these fine particles is compensated for by using an equivalent modulus for the mastic, which includes these fine particles, higher than that of the binder. Here the author explores the effect of using the equivalent modulus on microstructure strain distribution. Consider model "*A*" as shown in Fig. 3.7 that consists of coarse particles, fine particles, and binder. Model "*B*" represents the captured microstructure with the fine particles embedded within the mastic. FE analysis is conducted using the same material properties for all particles in model "*A*" and coarse particles in model "*B*" (Young's modulus = 25 GPa, and Poisson's ratio = 0.25). The binder in model "*A*" is represented with Young's modulus = 30 MPa and Poisson's ratio = 0.49. The same Poisson's ratio is used for the mastic in model "*B*", while a higher equivalent Young's modulus of 0.4 GPa is used for the mastic such that the macroscopic

strains for both models "*A*" and "*B*" are equal. As shown in Fig. 3.7, the two models have distinct microstructure strain distributions indicating that increasing the mastic modulus alone does not represent the model response at the microscopic level. Therefore, an alternative approach is followed in which the mastic is modeled using a higher equivalent modulus to reflect the stiffening effect of fine particles, and at the same time strain gradients with appropriate l_c represents the neglected particles are used to capture the influence of these fine particles on the microscopic strain distribution (see Fig. 3.7).

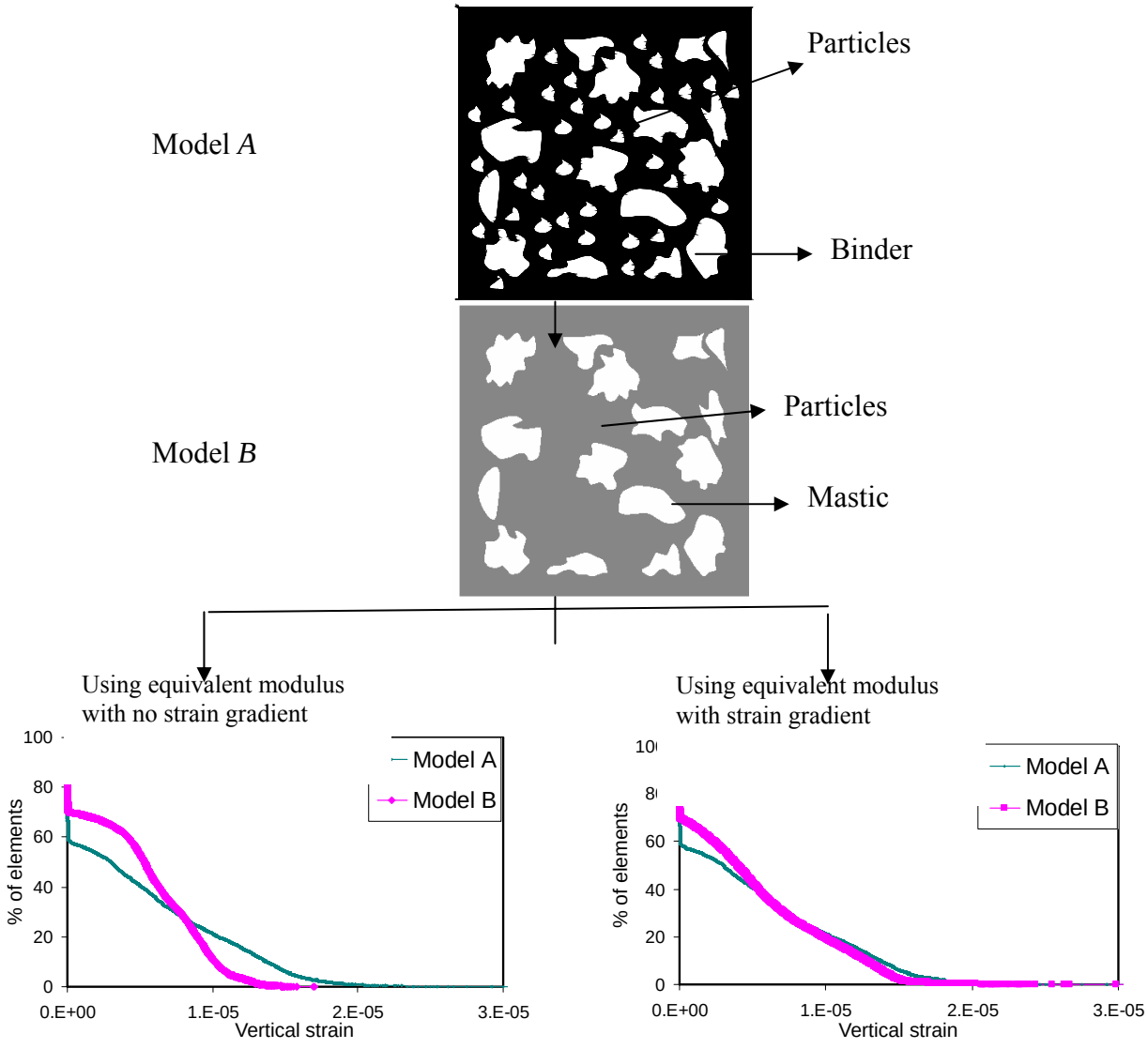

Figure 3.7. Influence of Strain Gradient on Microscopic Strain Distribution.

EFFECTIVE LOCAL MATERIAL PROPERTIES

Baxter and Graham (2000) presented an approach for FE analysis of composite material microstructure where the effective material properties are averaged within a moving window using the Generalized Method of Cells proposed by Paley and Aboudi (1992). In this study, we follow a similar approach; however, the effective material properties are calculated using a micromechanics solution that captures the influence of aggregate concentration within the moving window on the effective material properties. This approach is motivated by previous findings indicating that using the properties of the individual constituents in FE analysis of HMA microstructure significantly underestimates the macroscopic properties due to the experimental limitation of capturing all sizes of fine particles present in the microstructure (e.g., Masad and Somadevan 2002; Papagiannakis et al. 2002).

Christensen (1979) developed the well-known dilute suspension approximation for effective shear and bulk moduli μ and κ, respectively, of a macroscopically isotropic composite as follows:

$$\frac{\mu}{\mu_m} = 1 + \frac{15(1-\nu_m)\left(\frac{\mu_i}{\mu_m} - 1\right)}{7 - 5\nu_m + 2(4-5\nu_m)\frac{\mu_i}{\mu_m}} c$$

$$\frac{\kappa}{\kappa_m} = 1 + \frac{\left(\frac{\kappa_i}{\kappa_m} - 1\right)}{1 + \frac{\kappa_i - \kappa_m}{\kappa_m + \frac{4}{3}\mu_m}} c \qquad (3\text{-}11)$$

where i and m refer to the inclusion (aggregate) and matrix, respectively, ν_m is the matrix Poisson's ratio, and c is the volume fraction of the inclusions.

The model in Eq. (3-11) cannot be used for nondilute composites, such as HMA, in which interactions between particles influence the composite properties. Christensen (1990) modified the model in Eq. (3-11) using the differential method to better represent nondilute composites. The concept of the differential method is to add small percentages of particles (Δc) incrementally into the matrix. New effective properties are obtained for the composite in each increment and are subsequently used as matrix material properties in the following increments until c = 100%. The differential equations that represent this method are as follows:

$$\frac{d\mu}{dc} - \left(\frac{5(3\kappa + 4\mu)}{6(\kappa + 2\mu)}\right)\frac{\mu}{1-c} = 0$$
$$\frac{d\kappa}{dc} - \frac{\left(\kappa + \frac{4}{3}\mu\right)}{1-c} = 0 \qquad (3\text{-}12)$$

Christensen (1990) presented closed-form solutions for the effective properties of an incompressible material where $\kappa >> \mu$ and for the case of $\nu_m = 0.2$. However, the κ/μ ratio for HMA depends on the concentration of aggregates, and consequently, these solutions are not representative of asphalt mixes (Kim and Little 2004). Therefore, motivated by previous experimental measurements by Buttlar et al. (1999) and Kim and Little (2004), the following relation between κ and μ is proposed to solve Eq. (3-12):

$$\frac{\kappa}{\mu} = \beta \exp[\alpha(1-c)] \qquad (3\text{-}13)$$

where α and β are material constants determined based on experimental measurements and the properties of aggregates and binder as discussed later in this chapter. Eqs. (3-12, and 3-13) are solved such that the composite material properties are equal to those of the binder when $c = 0$. Eq. (3-12) is undefined for $c = 1$. Therefore, an approximate solution is sought where the composite properties are equal to those of aggregates when $c = 0.94$. A Gaussian quadrature numerical scheme is used to solve Eqs. (3-12 and 3-13) due to their implicit form, and the following expressions are obtained:

$$\ln\mu = \ln\mu_m - \frac{5}{3}\ln(1-c) + \frac{5}{6}\int_0^c \frac{\beta\exp\{\alpha(1-c^*)\}}{\beta(1-c^*)\exp\{\alpha(1-c^*)\}+2}dc^*$$
$$\ln\kappa = \ln\kappa_m - \ln(1-c) + \int_0^c \frac{\exp\{-\alpha(1-c^*)\}}{\beta(1-c^*)}dc^* \qquad (3\text{-}14)$$

The integration part can be solved numerically, and μ and κ are then found as a function of volume fraction. The Young's modulus E and Poisson's ratio ν are calculated using the elastic relationship with μ and κ.

EXPERIMENTAL CHARACTERIZATION

Description of Asphalt Mixes and Image Acquisition

Asphalt mixes were designed using the Superpave procedure (Roberts et al. 1996) with the variables shown in Table 3.1. The mixes were prepared with different nominal maximum aggregate sizes (aggregate size larger than about 90% of particles), two different gradations (fine and coarse), and two aggregate types (limestone and uncrushed gravel). HMA specimens were

compacted using the Superpave gyratory compactor. Each specimen had a diameter of 150 mm and a height of about 100 mm. A diamond saw was used to cut these specimens vertically.

Table 3.1. Description of Asphalt Mixes.

Mix	Aggregate Type	Gradation	NMAS*	Natural Sand (%)	OAC (%)**
A	Limestone	Coarse	9.5	0	5.3
B			19	0	4.4
C			19	40	4.7
D		Fine	9.5	0	6.2
E	Gravel	Coarse	9.5	0	6.3
F			19	0	5.4

* Nominal maximum aggregate size.
** Optimum asphalt content.

Gray scale images were captured using a digital camera connected to a computer. The original image was first reduced to a rectangular image with dimensions of 400×400 pixels and a resolution of 0.3 mm/pixel. A pixel in a gray-scale image has intensity from 0, representing black, to 255, representing white. Examples of images captured from the mixes are shown in Fig. 3.8. An image was thresholded and converted to a black-and-white image, where white represented aggregate particles larger than the image resolution of 0.3 mm and black represented the matrix, which consisted of asphalt, air voids, and particles smaller than 0.3 mm.

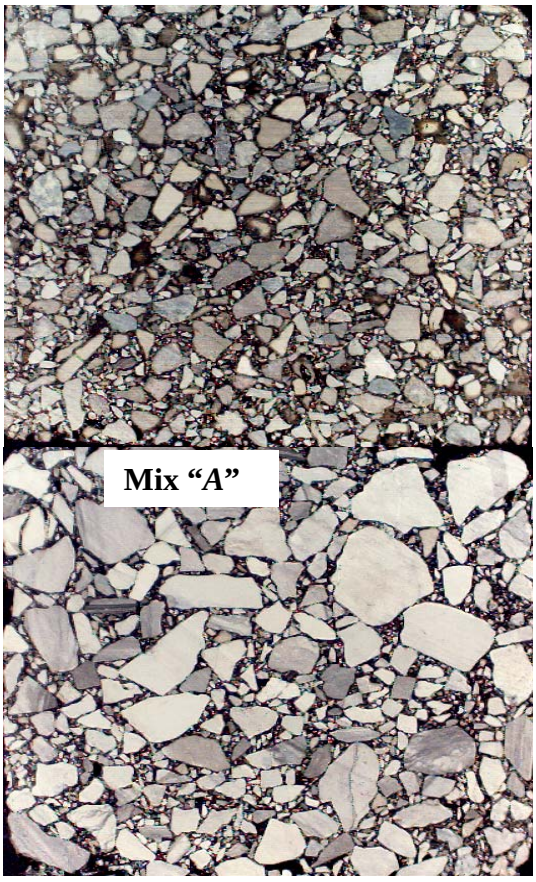

Mix "*B*"

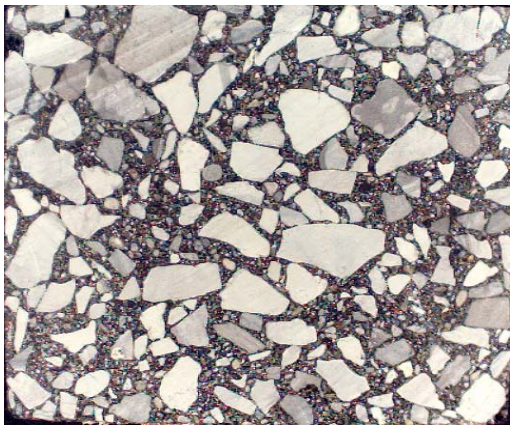

Mix "*C*"

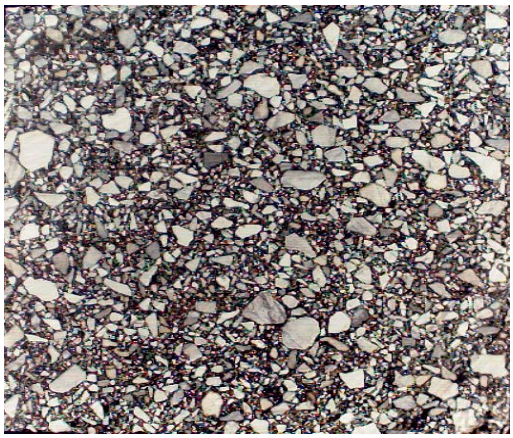

Mix "*D*"

Figure 3.8. Examples of Images with Different Aggregate Sizes.

Moving Window Technique

The moving window technique was used to calculate the effective elastic material properties in Eq. (3-14) and the characteristic length scale, l_c, in Eqs. (3-2, 3-4, 3-5 and 3-6). In this method, an image that represents the RVE of a mix is divided into cells or windows of equal sizes. Each window is shifted from the adjacent window by one pixel in the horizontal direction. A parametric analysis is first conducted to determine the appropriate window size to calculate the effective material properties. The percent of particles in windows of different sizes that included 10×10 pixels (3×3 mm), 20×20 pixels (6×6 mm), 40×40 pixels (12×12 mm), and 80×80 pixels (24×24 mm) were calculated for mixes *A* and *B*.

Small variations in percentage of particles between windows indicate more uniform distribution of particle sizes, while high variations indicate that a wide range of particle sizes is present within the microstructure. Fig. 3.9 shows that window sizes of 10×10 and 20×20 pixels produced high variations in percent aggregates for both mixes, which made it difficult to capture the differences between these two mixes in terms of percentage of particles and size distribution. Using a window size of 80×80 pixels was also not effective in capturing the difference between the two mixes, as it showed almost the same percentage of particles in windows for both mixes. However, the intermediate window size of 40×40 pixels captured the differences between mixes *A* and *B* (Fig. 3.9). Therefore, a window size of 40×40 pixels was employed in calculating the effective local material properties according to Eq. (3-14).

Effective material properties are calculated in three steps. First, the volume fraction of aggregates is determined within the moving window. Second, Eq. (3-14) is used to calculate the effective shear and bulk moduli. Finally, the corresponding Young's modulus and Poisson's ratio are calculated using elasticity theory. These effective properties are assigned to the element in the center of the moving window. The coefficients α and β in Eq. (3-13) are calculated using the material properties for aggregate and binder used earlier in the idealized microstructure. Consequently, the coefficients α and β are found to be 3.40 and 1.67, respectively.

Fig. 3.10 depicts the field of Young's moduli within the microstructure using both the properties of the individual constituents and the effective local properties, respectively. It is evident that a more uniform field of material properties is obtained using the effective material properties. This distribution is less affected by small changes that might occur in the microstructure distribution during image capturing and processing.

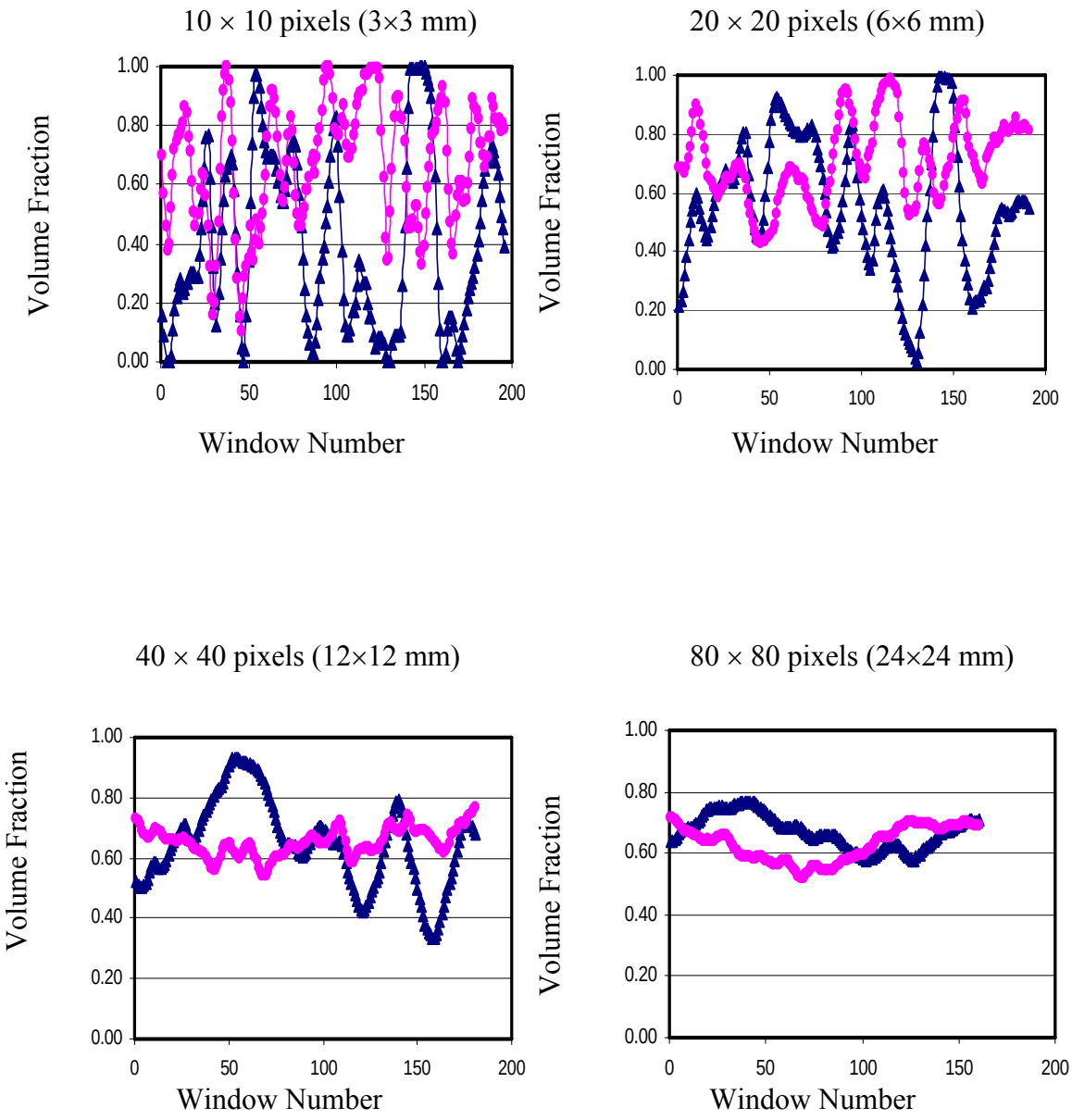

Figure 3.9. Volume Fraction of Particles for Different Window Sizes.

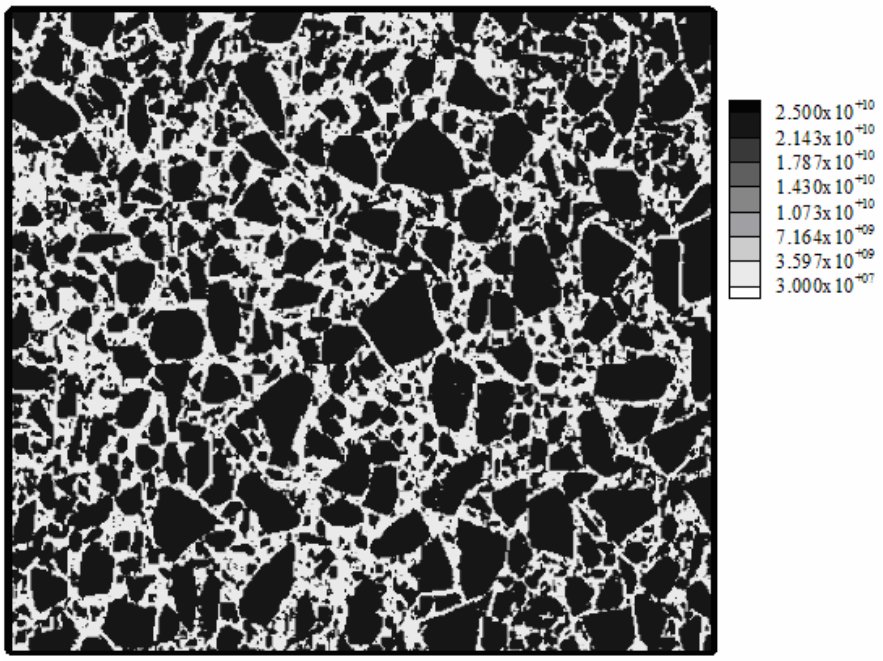

(a) Individual Constituent Properties

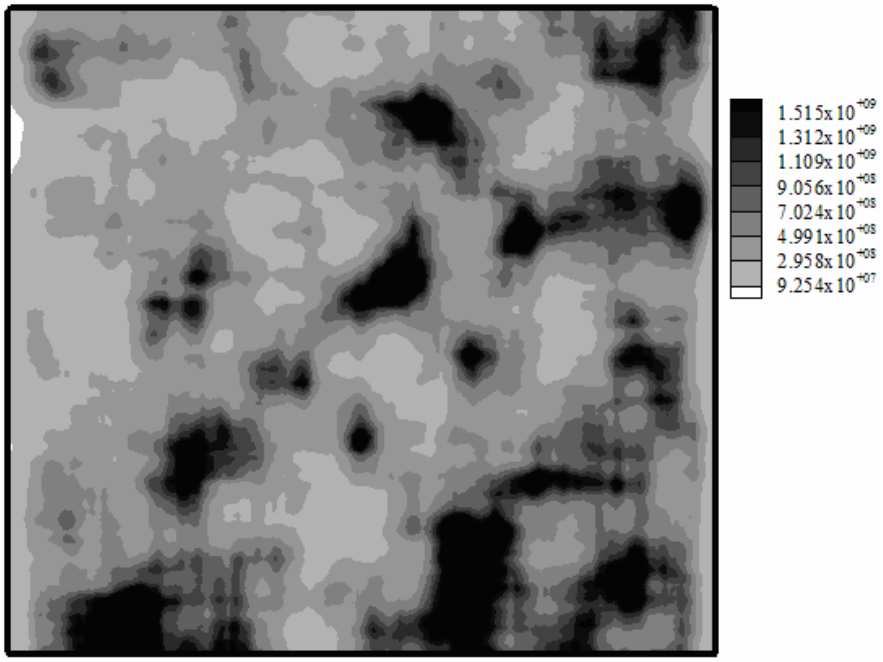

(b) Effective Properties

Figure 3.10. Young's Modulus Distribution for Microstructures with Individual Constituent Properties and Effective Properties.

FE analysis using the effective properties also has a numerical advantage over using the individual constituent properties. The several orders of magnitude difference in the moduli of the aggregate and binder can cause a numerical instability in the FE solution (Somadevan 2000). Using the effective material properties reduces the difference in material properties between adjacent elements, and consequently, eliminates this numerical limitation.

As discussed in the derivation of the constitutive model in Eqs. (3-2, 3-3, 3-4, 3-5 and 3-6), the value of the characteristic length scale, l_c depends on the microstructure distribution. The moving window technique is used to analyze the microstructure distribution and calculate l_c. Fig. 3.11 presents a schematic diagram of the application of the moving window technique. The method starts by converting an image to a two-dimensional text array where 1 indicates a pixel that belongs to the aggregate phase and 0 refers to a pixel that belongs to the matrix. The average volume fraction over the RVE domain at position vector x is given as:

$$\bar{g} = \frac{1}{V} \int_{V_{Ref}} g(x-r)dV \tag{3-15}$$

where g is the percentage of particles within the moving window and $\bar{g}$ is the average percentage of particles in the whole microstructure represented by an image. The Taylor's series expansion around x gives:

$$\bar{g} = g(x) + l_c^2 \nabla^2 g \tag{3-16}$$

where $g(x)$ is found by averaging the volume fraction within each window in the RVE. $\nabla^2 g$ is found by applying the central difference procedure between three adjacent windows in the horizontal direction. l_c is calculated for every moving window, and then an average value is calculated to represent the microstructure.

l_c for the different mixes is shown in Table 3.2. As the range of aggregate sizes becomes smaller, the probability for the moving windows to have more uniform percentages of particles increases, and consequently, l_c becomes smaller. However, variation in the concentration of aggregates among windows increases as the aggregate size distribution becomes wider. Consequently, l_c increases as the particle size distribution becomes wider. This can be seen in Table 3.2, where l_c for the 19 mm NMAS mixes is higher than that for the 9.5 mm NMAS mixes. The wide range of l_c values in Table 3.2 indicates the sensitivity of this parameter to microstructure distribution. However, more mixes with different microstructure distributions are needed to establish a conclusive relationship between particle size distribution and l_c.

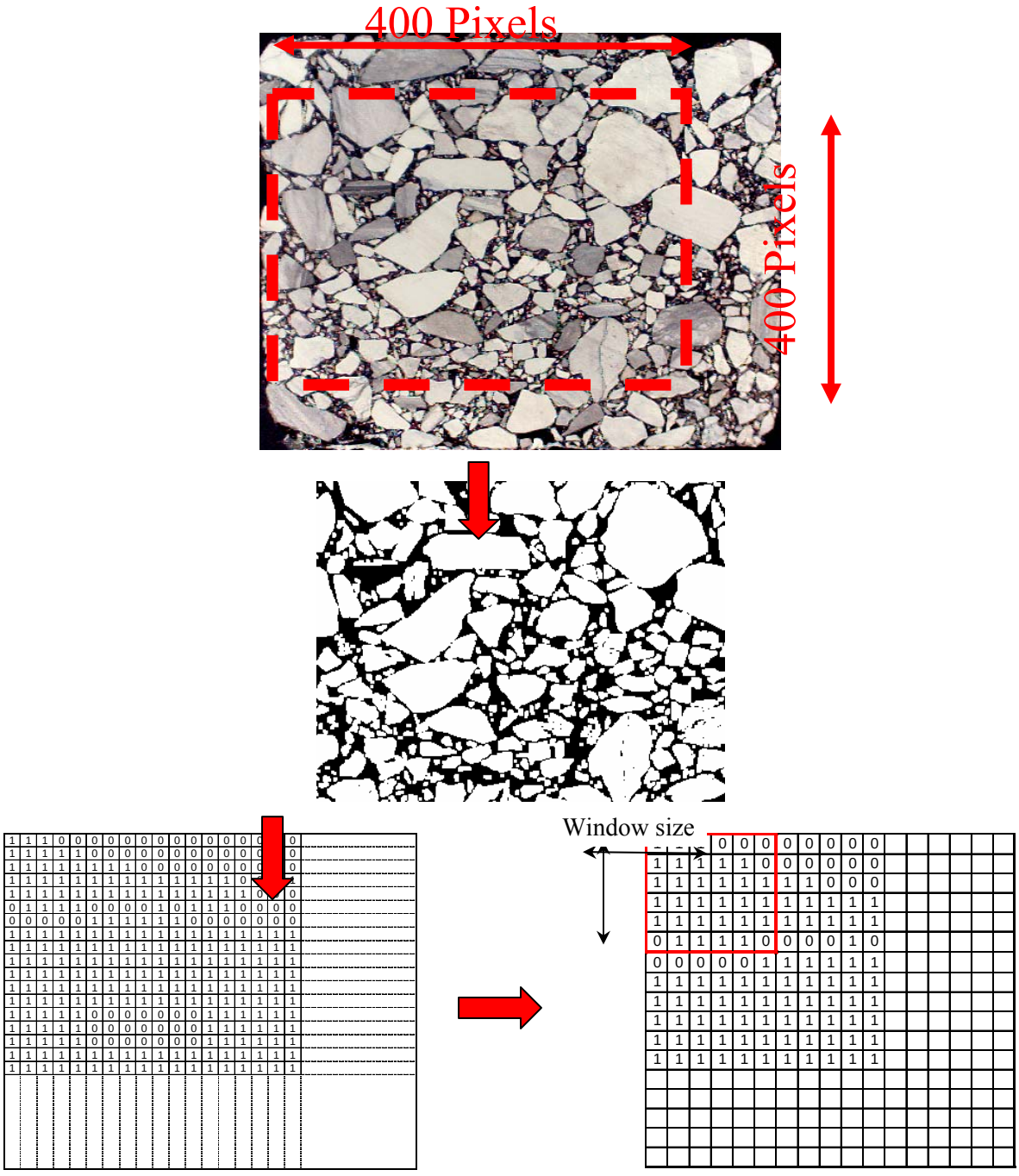

Figure 3.11. Schematic Diagram of the Application of the Moving Window.

Table 3.2. Results of Microstructure Analysis of Asphalt Mixes.

Mix	NMAS (mm)	Characteristic Length Scale l_c (mm)	Specific Surface area "s" (1/mm)	Mean Free Path "r_c" (mm)	Effective Particle Size "r_g" (mm)	Average Percentage of Particles "$\overline{f}$"	$\overline{f}^{2*}$	Measured $\overline{f}^{2**}$
A	9.5	4.11	0.60	1.51	5.40	0.660	0.436	0.433
B	19	5.19	0.50	1.69	9.90	0.670	0.450	0.450
C	19	5.28	0.47	1.97	8.40	0.611	0.373	0.365
D	9.5	3.19	0.67	1.41	3.90	0.625	0.391	0.383
E	9.5	2.79	0.61	1.54	4.80	0.672	0.452	0.454
F	19	4.72	0.55	1.59	9.00	0.718	0.516	0.509

* Using direct measurement of percentage of particles.
** Evaluated using graphical analysis of Figure 3.12.

Autocorrelation Function

The autocorrelation function (ACF) describes the relative arrangement of different phases in a composite material. It evaluates the probability of locating two points of the same material, whether aggregate or matrix, separated by a certain vector. It is assumed that the microstructure of asphalt mixes is statistically homogeneous, and consequently, ACF depends on the average difference in the coordinate values between two points rather than the locations of these points. In addition, the directional distribution of particles is not of interest in this study, and the ACF is taken as a function of the magnitude of the vector rather than its direction. Consequently, the two-point ACF is given as (Berryman and Blair 1986):

$$S(i,j)=\sum_{x=1}^{M-i}\sum_{y=1}^{N-j}\frac{f(x,y)\times f(x+i,y+j)}{(M-i)(N-j)} \tag{3-17}$$

where $f(x,y)=1$ if a pixel at point (x,y) is located within the aggregate phase, and $f(x,y)=0$ otherwise. i and j are the distances between any two pixels in two orthogonal coordinate axes. M and N are the number of pixels in the HMA microstructure image in two orthogonal coordinate axes.

The ACF carries important information about the microstructure distribution. Debye et al. (1957) and Berryman and Blair (1986) have shown that the following microstructure features can be estimated from the ACF (Fig. 3.12):

$$S(0)=\overline{f}, \qquad \lim_{r\to\infty}S(r)=\overline{f}^{2}, \quad S'(0)=-\frac{s}{4}, \quad r_c=\frac{4\overline{f}(1-\overline{f})}{s} \tag{3-18}$$

where $\overline{f}$ is the average volume fraction of aggregate particles, $r = \sqrt{i^2 + j^2}$ is the distance between two points in the microstructure, s is the specific surface area, and r_c is the effective distance between particles (mean free path). The effective particle size, r_g, can also be determined from the ACF as shown in Fig. 3.12.

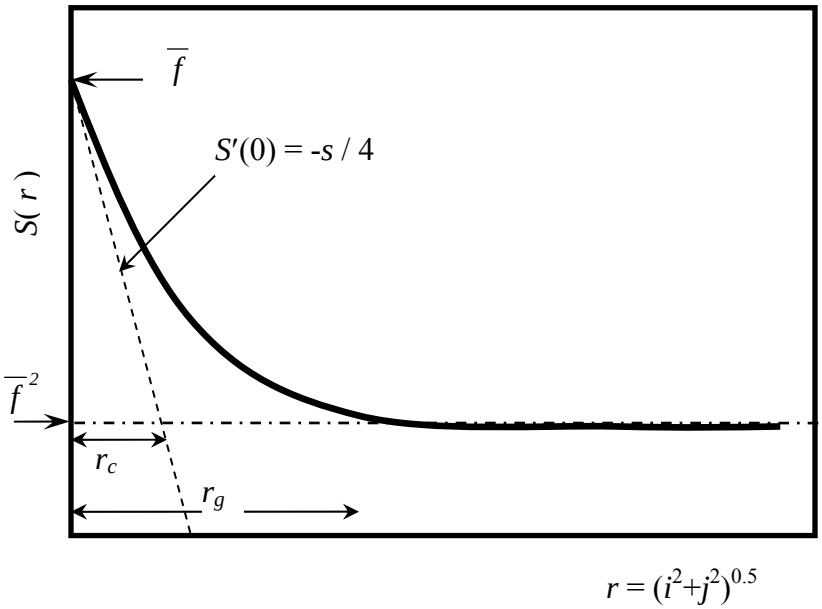

Figure 3.12. Illustration of the Autocorrelation Function.

Fig. 3.13 shows the trend of the correlation function for all mixes. A three-dimensional plot of the ACF distribution for two mixes assuming periodic microstructure is given in Fig. 3.14. According to the results in Table 3.2 and Figs. 3.13 and 3.14, mixes with 19 mm NMAS have higher r_g values than the 9.5 mm NMAS mixes (*A* vs. *B*) and (*E* vs. *F*). In addition, coarse-graded mixes have higher r_g values than the fine-graded mixes (*A* vs. *D*). There are also differences between gravel and limestone mixes with similar particle size distributions. Limestone mixes have higher values for r_c and r_g and lower values for s than gravel mixes. These results can be interpreted by the fact that limestone aggregate are more elongated (or less spherical) and the particles tend to be oriented more toward the horizontal in a mix than gravel aggregates. Therefore, the ACF measured in the horizontal direction gives larger effective length for limestone aggregates. This shows that the parameters from the ACF can be used to reflect the length scales associated not only with the size of particles but with their shape as well.

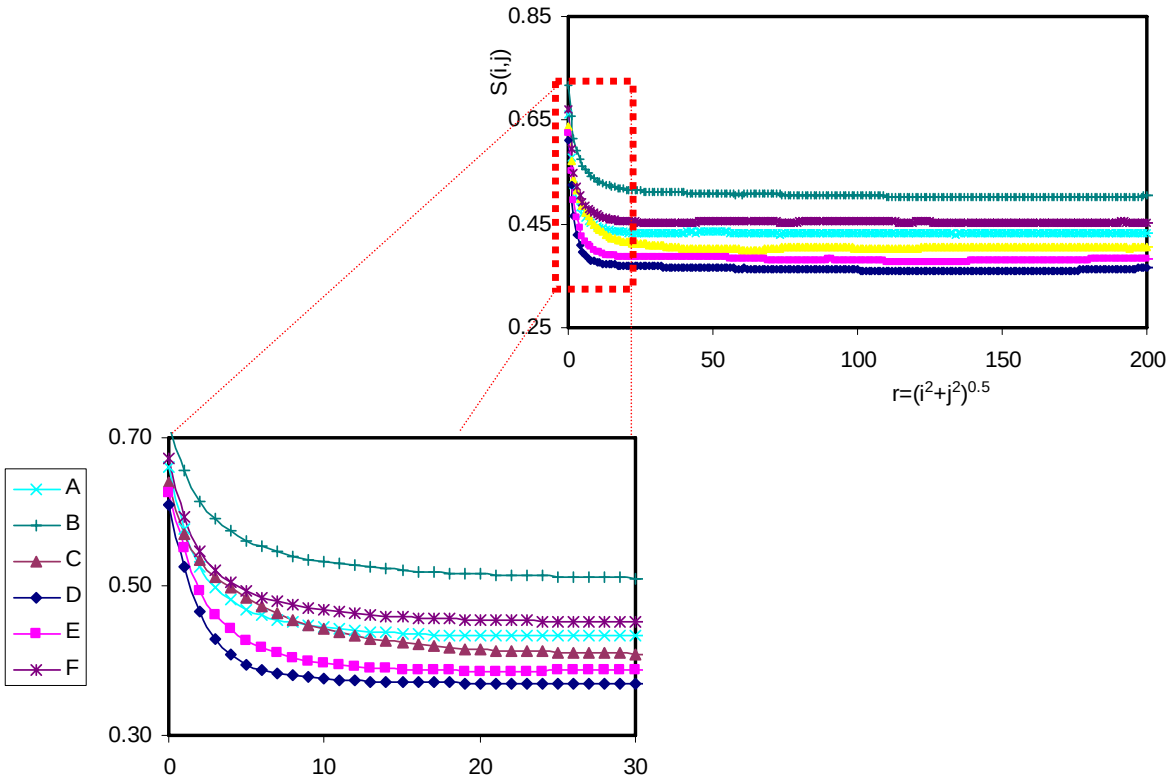

Figure 3.13. Autocorrelation Function for Different Mixes.

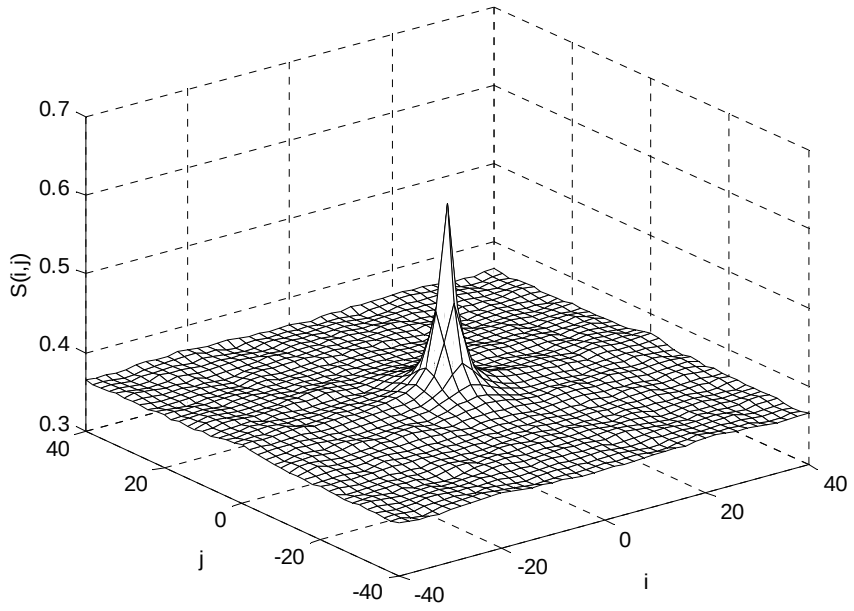

a) Mix "*D*"

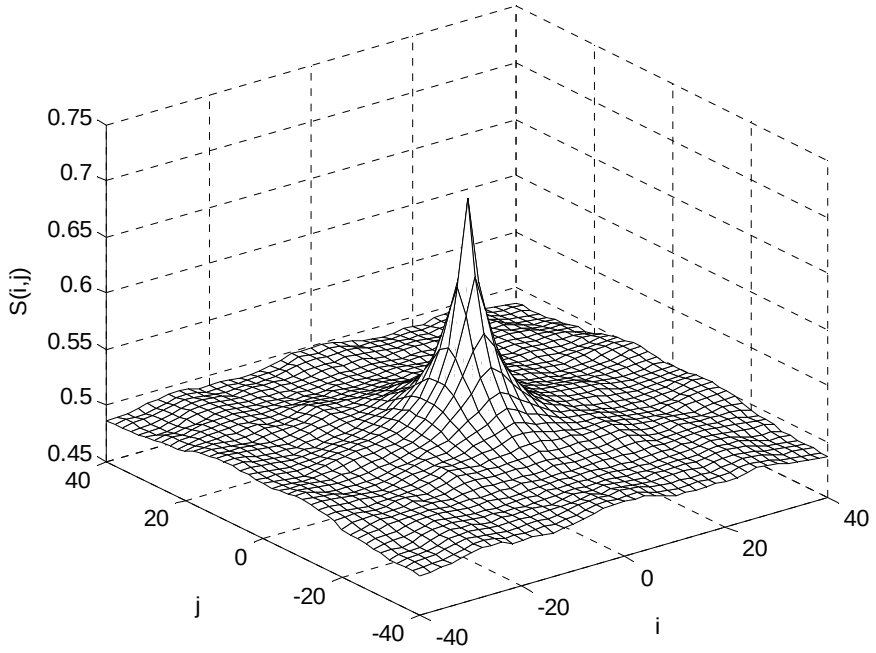

b) Mix "*C*"

Figure 3.14. Three-Dimensional Representation for the Autocorrelation Function.

Fig. 3.15 shows the relationship for the length scale parameters computed by the moving window and ACF methods. The results of the two methods have good agreement and either method can be applied to determine l_c for strain gradient theory.

HMA Microstructure FE Analysis and Results

The analyses of HMA microstructure are conducted using three approaches: (1) each element is assigned the elastic properties of the constituent that the element belongs to (conventional model), (2) each element is assigned effective local properties without strain gradients and characteristic length scales, and (3) each element is assigned effective local properties with the strain gradients and characteristic length scales. The FE model is subjected to uniaxial displacement at the top, and is fixed at the bottom from translation and rotation displacement. It is worth mentioning that FE analysis with strain gradients did not experience any convergence problems, and a maximum of three iterations were needed for the solution to converge using the procedure in Fig. 3.1.

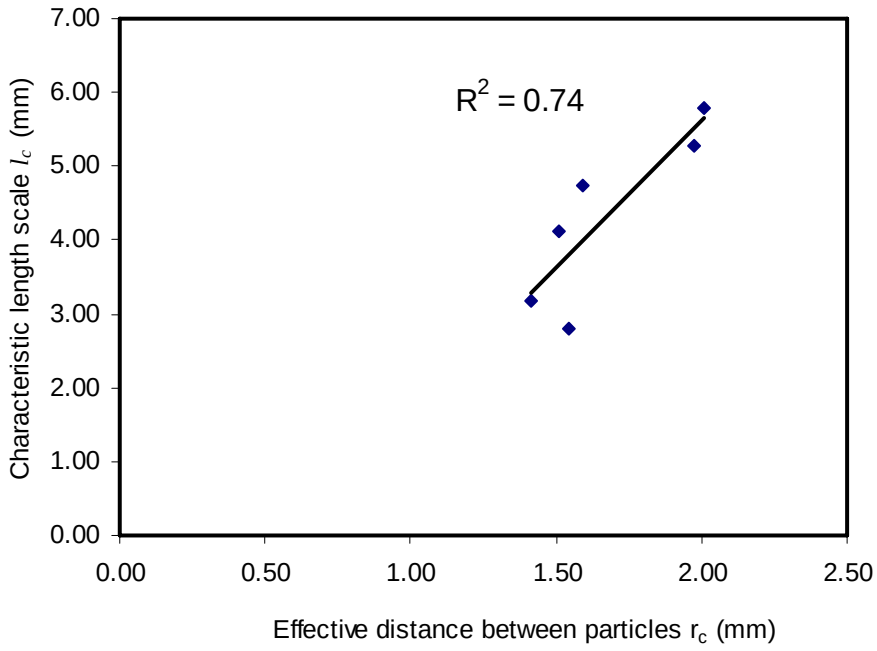

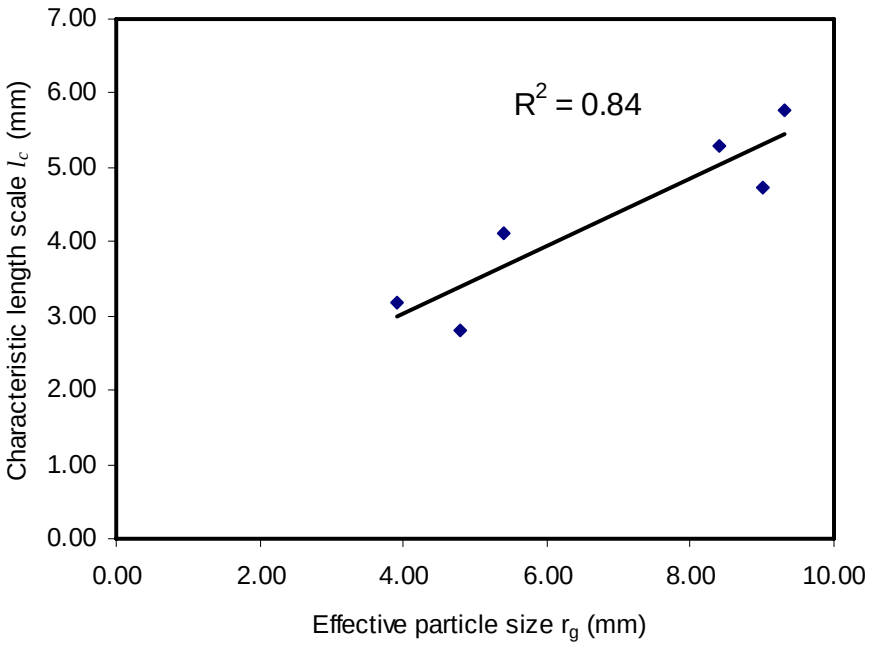

Figure 3.15. Correlations Between the Characteristic Length Scale (l_c), Effective Distance Between Particles (r_c), and Effective Particle Size (r_g).

Fig. 3.16 shows vertical strain distributions using approaches 1 and 2 described above for mix *A*. The conventional model (approach 1) produces high strain values in the thin film binder elements and low strain values in the elements occupied by aggregate particles. On the other hand, the model with effective material properties (approach 2) yields more uniform strain distribution.

Young's moduli are determined using the three approaches. These values are compared to experimental measurements of dynamic modulus at 10 Hz (Dessouky et al. 2004) and a temperature of 40°C. This comparison is not intended to evaluate the equality between FE results and measurements since the measurements are frequency dependent, but rather to determine how the analysis and experiments rank these mixes. The comparison is shown in Fig. 3.17 in terms of the ratio of the modulus of each mix to that of mix *B*. Measurements show that approaches 1 and 2 do not rank the Young's moduli of the mixes in the same order as the experimental measurements. However, approach 3, which combines the use of effective properties and strain gradients, ranks the mixes similar to the experimental measurements.

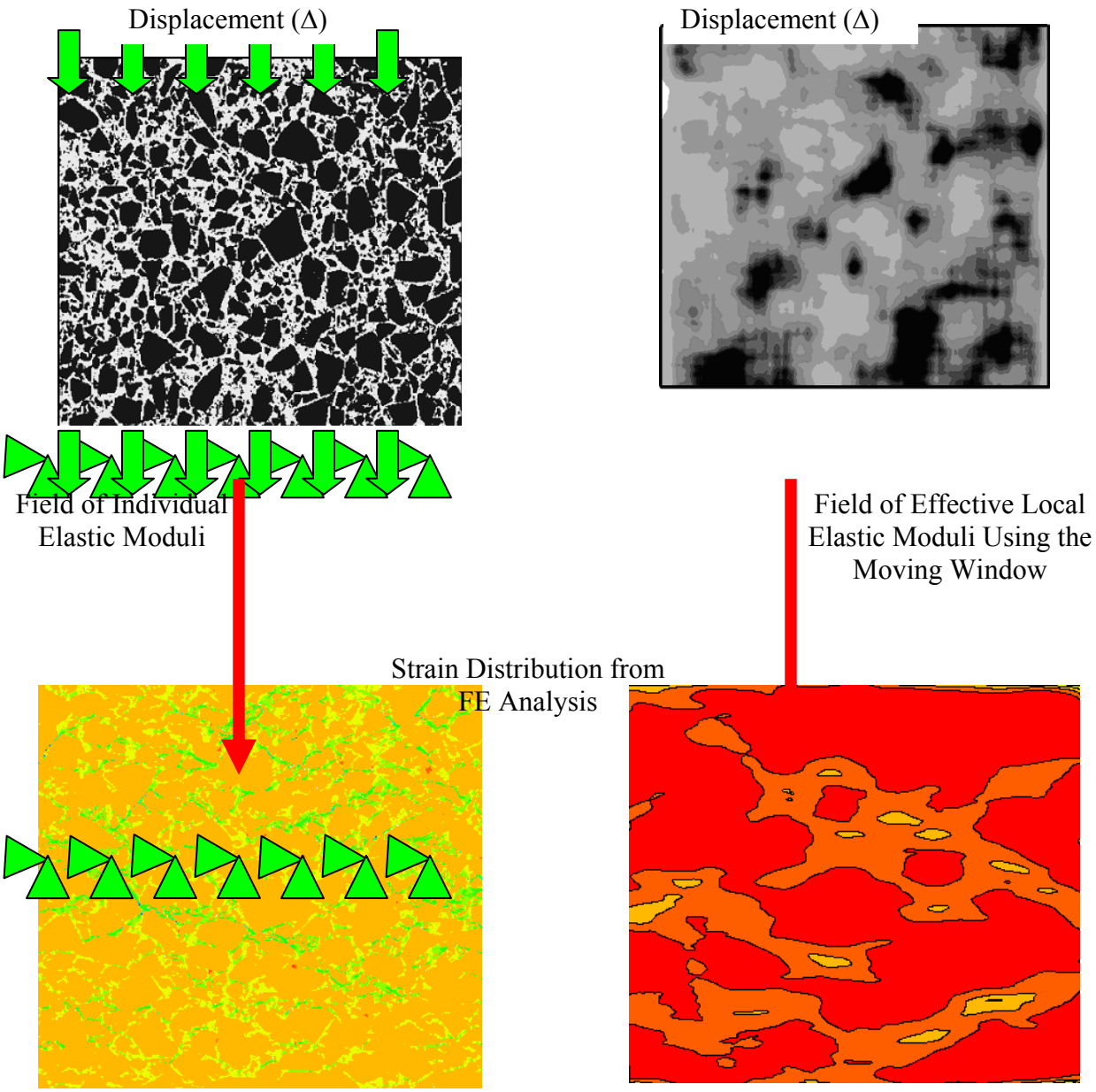

Figure 3.16. Vertical Strain Contours for Microstructure Using Individual Properties of Constituent and Effective Material Properties.

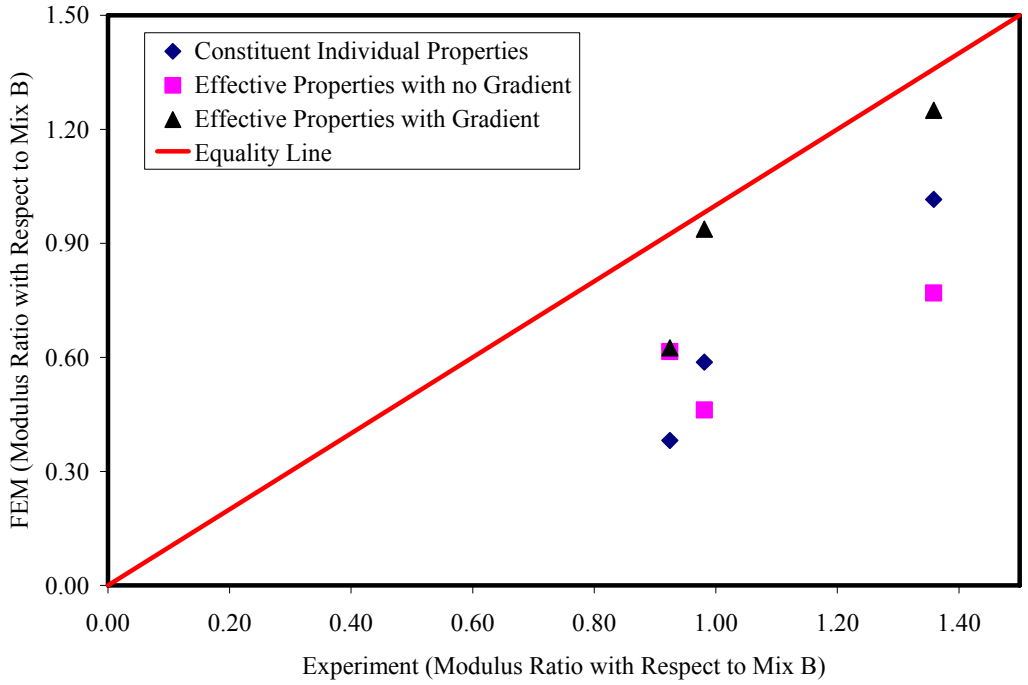

Figure 3.17. Moduli for Models with Different Microstructure Material Properties (Each Point Represents the Ratio of the Modulus of Mix *A* to the Modulus of Mix *B*)

SUMMARY

A methodology for microstructure analysis of HMA is presented in this chapter. The methodology is based on using effective material properties that capture the influence of percentage of particles on the local microscopic response. Strain gradient elasticity is employed in the FE analysis to capture the influence of the material length scale on material response. Experimental procedures are developed to determine the material characteristic length scale using the moving window technique and the ACF.

The results show that the developed methodology is successful in overcoming some of the limitations of using the individual properties of the constituents in the FE analysis of HMA microstructure. For example, this new methodology reduces mesh size dependency and reduces sensitivity of the response to small changes in microstructure caused by image capturing and processing. It also reduces the risk of numerical instability that can be caused by the several orders of magnitude difference in stiffness between adjacent elements of the microstructure. In addition, the methodology captures the influence of HMA length scales on the microscopic and macroscopic responses. The results show that the developed methodology yields HMA effective properties that are more consistent with experimental measurements.

CHAPTER IV

MICROSTRUCTURAL ELASTO-VISCO-PLASTIC CONTINUUM MODEL FOR HOT MIX ASPHALT

INTRODUCTION

As discussed in Chapter II of this report, rutting in hot mix asphalt (HMA) develops gradually as the number of load applications increases. It is caused by a combination of densification (decrease in volume and hence increase in density) and shear deformation. The visco-plastic continuum models available in the literature do not explicitly consider the influence of microstructure distribution on material response. The main objective of this chapter is to develop an elasto-visco-plastic microstructure model that accounts for important microstructure properties such as anisotropy and damage.

The new model builds upon the formulation developed by Tashman (2003), but it is expanded to include the elastic response of the material and to account for the influence of stress path direction. In addition, the procedure to account for anisotropy in the constitutive relationship is more simplified. Therefore in summary, the new model accounts for the following phenomena:

- Elastic response prior to reaching the yielding stress threshold;
- Shear as the dominant stress causing permanent deformation;
- Dilation and hydrostatic pressure dependency of the material;
- Stress path dependency of the visco-plastic response;
- Work hardening/softening of the material;
- Aggregate directional distribution in the microstructure; and
- Damage in terms of cracks and air voids.

DEVELOPMENT OF ELASTO-VISCO-PLASTIC MODEL

Abdulshafi and Majidzadeh (1985), Scarpas et al. (1997a) Lu and Wright (1998), Seibi et al. (2001), and Collop et al. (2003), among others, are examples of research that related HMA response to the presence of elastic, visco-elastic, visco-plastic, and plastic components under load application, where the presence of each is mainly affected by temperature and loading rate. In the new model, material response is assumed to have an elastic recoverable component and a visco-plastic irrecoverable component at the high temperatures associated with permanent deformation. The total strain rate $\dot{\varepsilon}$ is decomposed into

$$\dot{\varepsilon}_{ij} = \dot{\varepsilon}_{ij}^{e} + \dot{\varepsilon}_{ij}^{vp} \tag{4-1}$$

where the superscript (e) refers to the elastic part and (vp) refers to the visco-plastic part. A simple approach has been followed by many researchers in which constitutive relationship is developed for each strain component without coupling between the elastic and visco-plastic components. The elastic strain component can be defined according to Hook's law as follows:

$$\dot{\sigma}_{ij} = D_{ijkl}\dot{\varepsilon}^{e}_{kl} \tag{4-2}$$

where $\dot{\sigma}$ is the stress rate tensor and D_{ijkl} is the fourth-order elastic stiffness tensor.

By inserting Eq. (4-1) into Eq. (4-2) one may obtain the rate form of the constitutive equation as follows:

$$\dot{\sigma}_{ij} = D_{ijkl}\left(\dot{\varepsilon}_{kl} - \dot{\varepsilon}^{vp}_{kl}\right) \tag{4-3}$$

For axisymmetric configuration, the stiffness matrix reduces to the following expression:

$$[D] = \frac{E(1-\nu)}{(1+\nu)(1-2\nu)}\begin{bmatrix} 1 & \frac{\nu}{1-\nu} & 0 & \frac{\nu}{1-\nu} \\ \frac{\nu}{1-\nu} & 1 & 0 & \frac{\nu}{1-\nu} \\ 0 & 0 & \frac{1-2\nu}{2(1-\nu)} & 1 \\ \frac{\nu}{1-\nu} & \frac{\nu}{1-\nu} & 0 & 1 \end{bmatrix} \tag{4-4}$$

where E is Young's modulus and ν is Poisson's ratio.

The visco-plastic component dominates the response for the material at higher magnitudes of stress and higher temperatures. The visco-plastic strain rate component is defined through the following flow rule:

$$\dot{\varepsilon}^{vp}_{ij} = \dot{\gamma}^{vp}\frac{\partial g}{\partial \sigma_{ij}} \tag{4-5}$$

where $\dot{\gamma}^{vp}$ is a visco-plastic multiplier that is nonzero only when plastic deformation occurs, and g is a visco-plastic potential function. The potential surface is a surface in stress space containing the actual stress state and in case of the associated flow rule it coincides with the yield surface f:

$$g(\sigma'_{ij}) = f(\sigma'_{ij}) \tag{4-6}$$

Hence, the associated flow rule becomes

$$\dot{\varepsilon}^{vp}_{ij} = \dot{\gamma}^{vp}\frac{\partial f}{\partial \sigma_{ij}} \tag{4-7}$$

The gradient $\frac{\partial f}{\partial \sigma_{ij}}$ indicates the direction of the visco-plastic strain increment normal to the yield surface in the associated flow rule, while the magnitude of the strain vector is determined by the loading multiplier $\dot{\gamma}^{vp}$.

Perzyna's theory replaces the classical plastic flow rule by incorporating an overstress function and a viscosity parameter that relate the rate of visco-plastic strain to the current stresses and loading history. Analogous to the classical theory of incremental plasticity, the visco-plastic strain rate is computed by means of a postulated flow rule as follows (Perzyna 1966):

$$\dot{\varepsilon}_{ij}^{vp} = \Gamma \cdot < \phi(f) > \cdot \frac{\partial g}{\partial \sigma_{ij}} \tag{4-8}$$

where $\Gamma \cdot < \phi(f) >$ specifies the magnitude of the vector $\dot{\varepsilon}^{vp}$, Γ is a viscosity parameter that can be a constant or time-dependent, and ϕ is an overstress function that is typically taken as a power function of *f*. The visco-plastic potential and yield surfaces are assumed in this study to take the same form but with different material properties, as explained subsequently. In the above expressions, "$< \cdot >$", McCauley brackets, imply that:

$$< \phi(f) > = \begin{cases} 0, & \phi(f) \le 0 \\ \phi(f) = f^N, & \phi(f) > 0 \end{cases} \tag{4-9}$$

where *N* is a rate sensitivity parameter to be determined experimentally.

Eqs. (4-8 and 4-9) indicate that visco-plastic strain will take place only if the overstress function exceeds zero. The flow rule given by Perzyna is the necessary kinematic assumption postulated for visco-plastic deformation or plastic flow. Since it may be represented by a vector in strain space, the flow rule in Eq. (4-8) therefore also defines the direction of the visco-plastic strain increment.

Extended Drucker-Prager Yield Surface

The yield function determines a surface in stress space defined as follows:

$$f = \overline{F}(\sigma_{ij}) - \kappa = 0 \tag{4-10}$$

The yield surface f is defined as the geometric locus of states of stress corresponding to the same level of viscous flow. $\overline{F}(\sigma_{ij})$ is a stress-dependent function. To account for the effect of confinement, shear stress and dilative behavior in HMA, an extended Drucker-Prager yield function with hardening is proposed in this study. The conventional Drucker-Prager yield function has been used by a number of researchers to describe the viscous flow behavior of HMA (e.g., Abdulshafi

and Majidzadeh 1985; Seibi et al. 2001; Oeser and Moller 2004). The extended Drucker-Prager model is presented in the $I_1 - \tau$ space as shown in Fig. 4.1 (ABAQUS 2004, Park et al. 2001)

$$f = \tau - \alpha I_1 - \kappa \tag{4-11}$$

where τ is the deviatoric shear stress, I_1 is the hydrostatic stress, and α and κ are material properties. α is a parameter that reflects the material frictional properties of the material and κ is a hardening parameter that reflects the combined effect of the cohesion and frictional properties of the material.

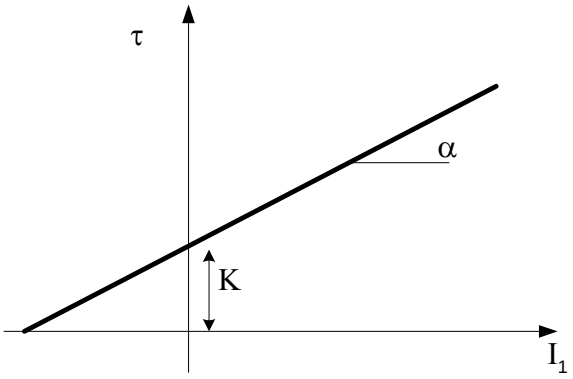

Figure 4.1. Schematic Diagram of the Extended Drucker-Prager Yield Surface .

In the extended model the hydrostatic stress and deviatoric shear stresses are defined as (ABAQUS 2004)

$$\begin{aligned} I_1 &= \frac{1}{3} trace(\sigma) = \frac{1}{3}\sigma_{ii} \\ \tau &= \frac{\sqrt{J_2}}{2}\left[1 + \frac{1}{d} + \left(1 - \frac{1}{d}\right)\frac{J_3}{J_2^{3/2}}\right] \end{aligned} \tag{4-12}$$

where

$$\begin{aligned} J_2 &= \frac{3}{2} S_{ij} S_{ji} \\ J_3 &= \frac{9}{2} S_{ij} S_{jk} S_{ki} \end{aligned} \tag{4-13}$$

S_{ij} is defined as the deviatoric stress tensor and is expressed as

$$S_{ij} = \sigma_{ij} - \frac{1}{3}\sigma_{kk}\delta_{ij} \tag{4-14}$$

δ_{ij} is the Kronecker delta, where its components are 1 if $i = j$ and 0 if $i \neq j$. I_1, J_2 and J_3 are the first stress invariant, second deviatoric stress invariant, and third deviatoric stress invariant, respectively. These invariants account for the effect of confinement, the dominant shear stress causing the visco-plastic deformation, and the direction of stress path, respectively. d is a material parameter representing the sensitivity of yield behavior to the hydrostatic pressure I_1. In uniaxial compression, Eq. (4-12b) indicates that $\frac{J_3}{J_2^{3/2}} = 1$ and $\tau = \sqrt{J_2}$, where $\tau = \frac{\sqrt{J_2}}{d}$ in uniaxial tension. To ensure convexity of the yield surface d ranges between 0.778 and 1. d value less than 1 indicates that the strength of the material in tension is lower than that in compression, as shown in Fig. 4.2. When d = 1, the dependence on the third deviatoric stress invariant vanishes and the Mises circle is recovered in the deviatoric plane.

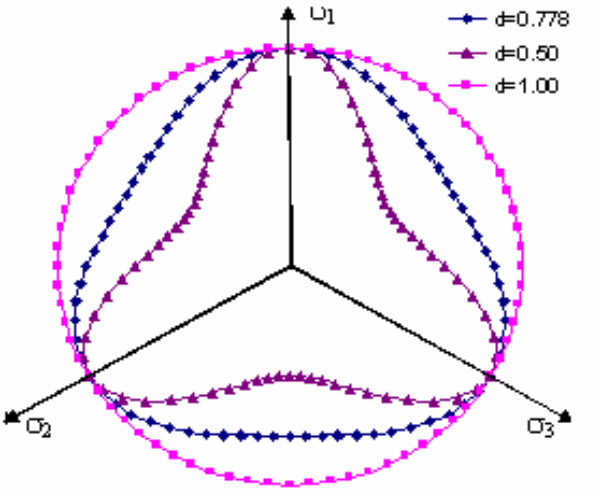

$$\tau = \frac{\sqrt{J_2}}{2}\left[1 + \frac{1}{d} + \left(1 - \frac{1}{d}\right)\frac{J_3}{J_2^{3/2}}\right]$$

Figure 4.2. Shape of the Yield Surface at the Deviatoric Plane as a Function of d (ABAQUS 2004; Park et al. 2001).

The influence of the d parameter on the model response is illustrated in Fig. 4.3. Consider a point that is under confining pressure and is represented by point A. Once the point is subjected to an increase in axial stress, both the first stress invariant and the second deviatoric stress invariant will increase with stress path until it starts to yield at point B. Conversely, if the specimen is subjected to a decrease in the axial stress (extension test), the stress path will be represented by the path AC and the point will yield under the stress state represented by point C. Even under the conventional Drucker-Prager yield function, the yield stress in compression will be higher than the yield stress in tension simply because the confinement at points B and C are different. In the modified model represented by Eq. (4-11), the yield stress under tension is further reduced as the slope (α') and the intercept (κ') of the yield surface in the $I_1 - \sqrt{J_2}$ plane are multiplied by d.

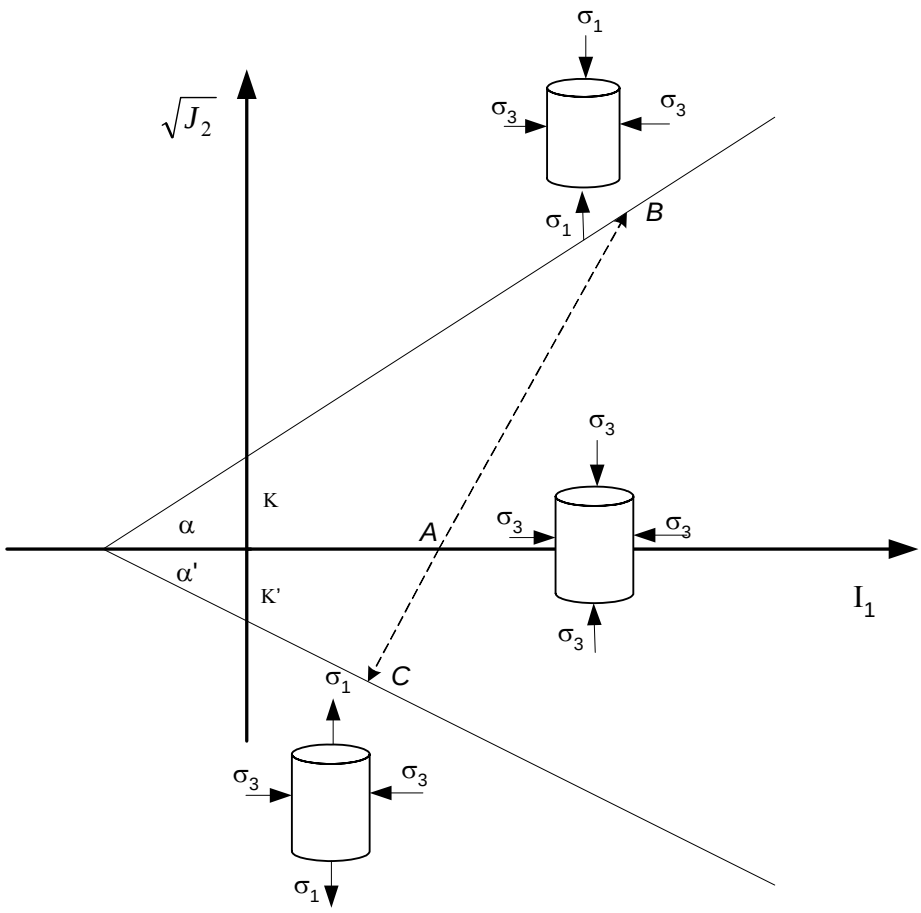

Figure 4.3. Illustration of the Influence of Stress Path on the Yielding Point.

An important factor governing the viscous behavior of a material is the phenomenon of work hardening. In simple terms, the phenomenon occurs during plastic deformation of the material at a microscopic level due to changing interactions in the aggregate-aggregate and aggregate-binder interfaces as the degree of deformation increases. Basically, the larger the number of particle contacts produced, the larger their interaction and hence the larger the stresses required for material yielding. When the stress level approaches the yield point, the yield surface is pushed outward and causes increasing in surface volume. This growing mechanism can be defined by a hardening evolution law.

Material hardening can be captured by the evolution of α, κ or both, Tan et al. (1994) concluded that α remains almost constant as the material undergoes permanent deformation, while κ value evolves. This conclusion is supported by the analyses conducted on experimental measurements used in this study and presented in Chapter VI. The general form for the evolution of κ is a function of effective visco-plastic strain. The specific form determined in this study and based on experimental measurements is presented in Chapter VI.

MICROSTRUCTURE CHARACTERIZATION

Anisotropy

It is well documented in the literature that unbound granular materials display significant anisotropic behavior because of the preferred distribution of particles (e.g., Oda and Nakayama 1989; Li and Dafalias 2000). Tobita and Yanagisawa (1988) stated that a constitutive model with anisotropic dependency can account for more aspects of deformation features of geomaterials than conventional plasticity theory because it represents information about anisotropic internal structure. Oda and Nakayama (1989) summarized the three sources of anisotropy in granular materials: anisotropic distribution of contact normals, which is due to particle interactions; preferred orientation of void spaces; and preferred orientation of nonspherical particles. Oda et al. (1985) observed that the first two sources can be significantly effective during low levels of deformation, while the last source dominates the behavior at later stages of deformation.

HMA microstructure distribution can be measured using an image analysis technique (IAT), which is the process of converting an image into a digital form and applying various mathematical procedures to extract significant information from the image. Masad et al. (1998, 1999a, and 1999b) developed automated computer image analysis techniques to analyze the internal structure of HMA. The techniques were successfully implemented to evaluate different laboratory compaction procedures. Tashman et al. (2001) developed an IAT to quantify the microstructure of HMA based on aggregate orientation, aggregate gradation, aggregate contacts, aggregate segregation, and air void distribution.

In this study, microstructure directional distribution is formulated based on particle orientation distribution. This choice is motivated by a number of factors discussed by Masad et al. (2003). First, particle orientation resists reorientation under loading, and consequently, inherent anisotropy is better preserved in a formulation that accounts for particle orientation (e.g., Oda et al. 1985; Tobita 1989). This phenomenon has been captured experimentally by Tashman (2003) as shown in Fig. 4.4. Second, previous experimental measurements of directional quantities have shown that it is easier and more practical to measure particle orientation than particle contacts (Masad et al. 2002). Third, particle preferred orientation is directly related to the deviation of particle shape from a spherical reference. Such a relationship offers the opportunity to predict the anisotropy level based on measurements of particle shape without the need to conduct microstructure measurements (Masad et al. 2003).

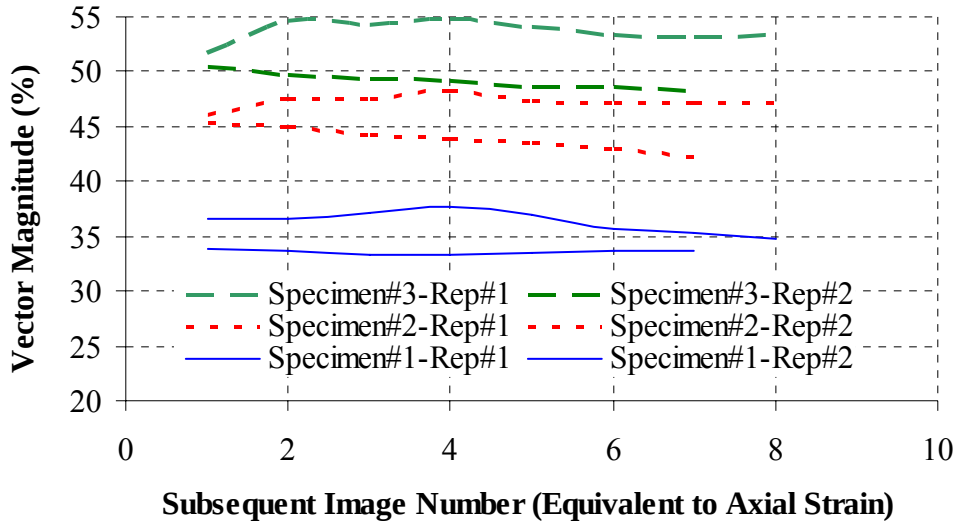

Figure 4.4. Effect of Deformation on the Vector Magnitude (after Tashman 2003).

Tashman et al. (2001) measured aggregate directional distribution in HMA, where the orientation of an aggregate particle is defined by the angle between its major axis and a horizontal line on the scanned image. The major axis length is defined by the greatest distance between two edge points of the boundary contour. Masad et al. (1998) reported that aggregate orientation in HMA exhibits inherent transverse anisotropy with respect to the horizontal direction. The major axes of particles tend to be oriented in the horizontal direction, and consequently, the horizontal plane represents the major principal direction and the vertical plane represents the minor principal direction.

The directional distribution of particles has been quantified on images of vertical sections of HMA by using the vector magnitude, Δ (e.g., Masad et al. 1998; Tashman et al. 2001):

$$\text{Vector Magnitude}(\Delta) = \frac{100}{n}\sqrt{\left(\sum \sin 2\theta_k\right)^2 + \left(\sum \cos 2\theta_k\right)^2} \quad (\%) \qquad (4\text{-}15)$$

where θ_k is the orientation of the major axis of an individual aggregate on an image from -90^o to $+90^o$ measured from the horizontal direction (the positive sign indicates that the angle is measured counterclockwise from the horizontal direction, as shown in Fig. 4.5) and n is the number of aggregates on that image. Theoretically, the value of Δ ranges between 0 and 1, and practically it varies from 0 to 0.5 for HMA. A value of 0 indicates the aggregates are completely randomly distributed, which reflects an isotropic distribution, and a value of 1 indicates the aggregates are all oriented in the same direction.

Oda et al. (1985) and Tobita (1989) introduced a microstructure tensor that aimed to describe the particle orientation in the material response.

$$F_{ij} = \int_{\Omega} m_i m_j E(m) d\Omega \qquad (i, j = 1, 2) \tag{4-16}$$

where m_i (i = 1, 2) are components of a unit vector m projected on the orthogonal reference axes x_i (i = 1, 2); Ω is a solid angle corresponding to the two-dimensional plane ($\Omega = 2\pi$); and $E(m)$ is a probability density function that describes the spatial distribution of the vector m. Given the transverse anisotropic distribution of particles in HMA, the F_{ij} tensor can be presented in diagonal form by three principal values: F_1, F_2, and F_3, as follows (Oda and Nakayama 1989):

$$[F] = \begin{bmatrix} F_1 & 0 & 0 \\ 0 & F_2 & 0 \\ 0 & 0 & F_3 \end{bmatrix} = \frac{1}{3+\Delta} \begin{bmatrix} 1-\Delta & 0 & 0 \\ 0 & 1+\Delta & 0 \\ 0 & 0 & 1+\Delta \end{bmatrix} \tag{4-17}$$

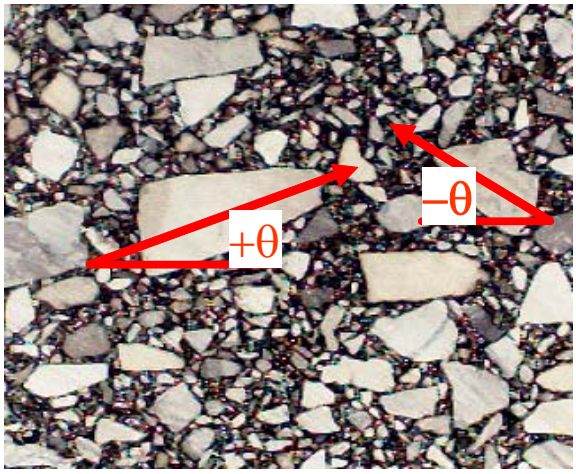

Figure 4.5. Schematic Diagram of Anisotropy in a Conventional HMA Microstructure.

Microstructure directional distribution is accounted for within the framework of the representation theorem of isotropic functions such that the principle of material objectivity or frame indifference is satisfied (Tobita 1989). An effective stress tensor is introduced that combines the stress tensor and the microstructure distribution tensor as follows:

$$\bar{\sigma}_{ij} = \frac{3}{2}\left[\sigma_{ik} F_{kj} + F_{ik} \sigma_{kj}\right] \tag{4-18}$$

where $\bar{\sigma}_{ij}$ is the modified stress tensor that considers the material anisotropy. The formulation for the effective stress tensor can involve higher-order microstructure tensors. However, for simplicity, only the second-order microstructure tensor is considered.

Damage

Damage models describe material weakening caused by formation of air voids and propagation of cracks that consequently may lead to material failure. A new discipline has been developed recently to investigate the growth of microcracks and the mechanical behavior of damaged materials by representing the effect of distributed cracks in terms of certain mechanical variables (Murakami 1983). This method is called continuum damage mechanics (CDM), in which damage is defined as a microstructural change that induces some deterioration in the material. Kachanov (1958) introduced the concept of the effective stress theory, which has been successfully implemented to describe damage in terms of crack nucleation and growth within the framework of CDM.

The effective stress theory indicates that material damage can be characterized mainly by the decrease in the load-carrying effective area caused by the development of microscopic cracks and cavities (Murakami 1988). The theory postulates that a damaged material subjected to a state of stress can be represented by a perfect material subjected to a fictitious stress. The fictitious stress is equal to the stress applied to the damaged material magnified by the decrease in the load-carrying effective area as shown in Eq. (4-19). This magnification factor is referred to as the damage parameter and is an indication of the material state of damage.

$$\sigma_{ij}^{e} = \frac{1}{1-\xi}\sigma_{ij} \tag{4-19}$$

where ξ is an internal variable that accounts for the effect of damage in terms of cracks and air voids that varies from 0 for presently undamaged material to 1 for a completely damaged phase. Pioneering work by Desai (1998) proposed to adopt the notion that damage is a function of confining pressure and effective visco-plastic strain as follows:

$$\xi = \xi(I_1, \varepsilon_{vp}) \tag{4-20}$$

Implementing the modified stress tensor using Eq. (4-18) and the effective stress theory in Eq. (4-19) into the extended Drucker-Prager yield function Eq. (4-11), the invariants $\bar{I}_1^e, \bar{J}_2^e$ and $\bar{J}_3^e$ become as follows:

$$\begin{aligned} \bar{I}_1^e &= \frac{1}{3} trace(\bar{\sigma}^e) = \frac{1}{1-\xi}\cdot\sigma_{ik}F_{ki} \\ \bar{J}_2^e &= \frac{3}{2}\cdot\frac{1}{(1-\xi)^2}\cdot\bar{S}_{ij}\bar{S}_{ji} \\ \bar{J}_3^e &= \frac{9}{2}\cdot\frac{1}{(1-\xi)^3}\cdot\bar{S}_{ij}\bar{S}_{jk}\bar{S}_{ki} \end{aligned} \tag{4-21}$$

and the extended Drucker-Prager yield function is modified to the form

$$f = \bar{\tau}^e - \alpha \bar{I}_1^e - \kappa \tag{4-22}$$

Assuming a power law function for the viscous flow, Eq. (4-22) and Eq. (4-8) lead to

$$< \phi(f) > = \begin{cases} 0, & \left(\bar{\tau}^e - \alpha \bar{I}_1^e - \kappa\right) \le 0 \\ \left(\bar{\tau}^e - \alpha \bar{I}_1^e - \kappa\right)^N, & \left(\bar{\tau}^e - \alpha \bar{I}_1^e - \kappa\right) > 0 \end{cases} \tag{4-23}$$

The modified stress tensor modified for anisotropy and damage is used instead of the stress tensor in the constitutive relationship shown in Eq. (4-3). Therefore, the influences of anisotropy and damage are reflected in the elastic and visco-plastic deformation of the material.

PLASTIC POTENTIAL FUNCTION

It is well documented in the literature that granular materials exhibit nonassociative behavior in which the yield surface and the potential surface do not coincide. Experimental observations indicate that the associated flow rule produces more dilation than experimental measurements (e.g., Zeinkiewicz et al. 1975; Oda and Nakayama 1989). It follows that a dilation parameter of a value less than α should be incorporated in the model. It is assumed as shown in Fig. 4.6 that the potential surface takes the same linear form of the yield surface but with smaller slope β which influences the proportions of the volumetric and deviatoric strains.

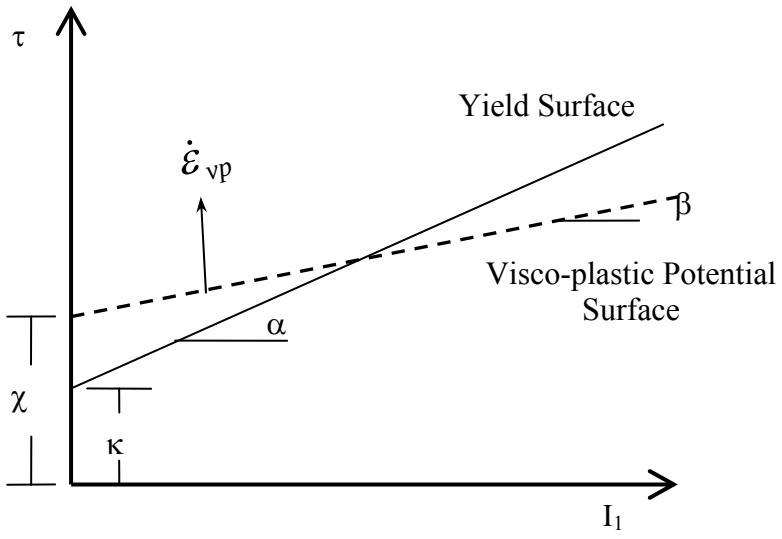

Figure 4.6. Relationship Between Slopes of the Yield Surface and the Potential Surface.

In order to evaluate the gradient operator for the potential function $\frac{\partial g}{\partial \sigma_{ij}}$ in the constitutive Eq. (4-8), a triaxial state of stress is utilized. According to Eqs. (4-17 and 4-18), the principal state of stresses for the triaxial setup is expressed as

$$\bar{\sigma}_{ij} = \begin{bmatrix} \bar{\sigma}_1 & 0 & 0 \\ 0 & \bar{\sigma}_3 & 0 \\ 0 & 0 & \bar{\sigma}_3 \end{bmatrix} = \frac{3}{3+\Delta} \begin{bmatrix} (1-\Delta)\sigma_1 & 0 & 0 \\ 0 & (1+\Delta)\sigma_3 & 0 \\ 0 & 0 & (1+\Delta)\sigma_3 \end{bmatrix} \tag{4-24}$$

and the modified invariants as defined by Eq. (4-21) are given in the form

$$\begin{aligned} \bar{J}_2^e &= \frac{1}{(1-\xi)^2}(\bar{\sigma}_1 - \bar{\sigma}_3)^2 \\ \bar{J}_3^e &= \frac{1}{(1-\xi)^3}(\bar{\sigma}_1 - \bar{\sigma}_3)^3 \end{aligned} \tag{4-25}$$

Substituting Eq. (4-25) into Eq. (4-12b) one obtains

$$\bar{\tau}^e = \frac{\sqrt{\bar{J}_2^e}}{2(1-\xi)}\left[1 + \frac{1}{d} + \left(1 - \frac{1}{d}\right)\frac{\bar{J}_3^e}{\left(\bar{J}_2^e\right)^{3/2}}\right] \tag{4-26}$$

The gradient of the potential surface can be expressed with respect to the stress dependent variables to become

$$\frac{\partial g}{\partial \sigma_{ij}} = \frac{\partial \bar{\tau}^e}{\partial \sigma_{ij}} - \beta \frac{\partial \bar{I}_1^e}{\partial \sigma_{ij}} \tag{4-27}$$

Considering β and κ as stress-independent parameters, the derivatives of the invariants with respect to the stress can be expressed as follows:

$$\begin{aligned} \frac{\partial \bar{I}_1^e}{\partial \sigma_{ij}} &= \frac{1}{1-\xi} F_{ij} \\ \frac{\partial \bar{J}_2^e}{\partial \sigma_{ij}} &= \frac{1}{(1-\xi)^2}\bar{J}_2{}' = \frac{1}{(1-\xi)^2} \cdot \frac{9}{2} \cdot \left[\bar{S}_{ik} F_{kj} + F_{ik} \bar{S}_{kj}\right] \\ \frac{\partial \bar{J}_3^e}{\partial \sigma_{ij}} &= \frac{1}{(1-\xi)^3}\bar{J}_3{}' = \frac{1}{(1-\xi)^3} \cdot \frac{27}{2} \cdot \left[\frac{3}{2}\left(\bar{S}_{ik}\bar{S}_{kn}F_{nj} + F_{ik}\bar{S}_{kn}\bar{S}_{nj}\right) - \frac{2}{3}\bar{J}_2 F_{ij}\right] \end{aligned} \tag{4-28}$$

Substituting Eq. (4-28) into Eq. (4-27) the derivative of the yield function becomes

$$\frac{\partial g}{\partial \sigma_{ij}} = \frac{1}{2(1-\xi)}\left[\left(1+\frac{1}{d}\right)\frac{\bar{J}_2^{'}}{2\sqrt{\bar{J}_2}} - \left(1-\frac{1}{d}\right)\frac{\bar{J}_3^{'}\bar{J}_2 - \bar{J}_3\bar{J}_2^{'}}{\bar{J}_2^2} - 2\beta F_{ij}\right] \tag{4-29}$$

By decomposing Eq. (4-29) the components of the gradient $\frac{\partial g}{\partial \sigma_{ij}}$ are expressed in the following forms:

$$\begin{aligned}
&\frac{\partial g}{\partial \sigma_{11}} = 3\cdot\frac{1}{1-\xi}\cdot\frac{1-\Delta}{3+\Delta}\cdot\left(\frac{1}{d}-\frac{\beta}{3}\right)\\
&\frac{\partial g}{\partial \sigma_{22}} = \frac{\partial g}{\partial \sigma_{33}} = 3\cdot\frac{1}{1-\xi}\cdot\frac{1+\Delta}{3+\Delta}\cdot\left(-\frac{1}{2d}-\frac{\beta}{3}\right)\\
&\frac{\partial g}{\partial \sigma_{12}} = \frac{\partial g}{\partial \sigma_{13}} = \frac{\partial g}{\partial \sigma_{23}} = 0
\end{aligned} \tag{4-30}$$

EFFECTIVE STRESS AND EFFECTIVE VISCO-PLASTIC STRAIN

In order to evaluate the hardening and damage parameters explained previously, an expression for effective stress and effective visco-plastic strain is required. Chen and Han (1988) indicated that to evaluate effective stress the stress function $F(\sigma_{ij})$ defined in Eq. (4-10) is employed. For a uniaxial compression state of stress effective stress is reduced to the uniaxial stress σ_1. Chen and Han (1988) showed that $\bar{F}(\sigma_{ij})$ can be defined as a power law function in terms of effective stress

$$\bar{F}(\sigma_{ij}) = \bar{\tau}^e - \alpha\bar{I}_1^e = C\left(\sigma_{ef}\right)^m \tag{4-31}$$

where C and m are constant coefficients. Following similar manipulation using a uniaxial state in Eq. (4-18) and the modified invariants in Eq. (4-21) one can obtain

$$\begin{aligned}
&\bar{I}_1^e = \frac{1}{1-\xi}\cdot\frac{1-\Delta}{3+\Delta}\sigma_{ef}\\
&\bar{J}_2^e = \frac{3}{2}\cdot\frac{1}{(1-\xi)^2}\cdot\left(\frac{1-\Delta}{3+\Delta}\right)^2\left(\sigma_{ef}\right)^2\\
&\bar{J}_3^e = \frac{9}{2}\cdot\frac{1}{(1-\xi)^3}\cdot\left(\frac{1-\Delta}{3+\Delta}\right)^3\left(\sigma_{ef}\right)^3
\end{aligned} \tag{4-32}$$

By inserting Eq. (4-32) into Eq. (4-31) one can solve for the constants

$$C = 3 \cdot \frac{1}{1-\xi} \cdot \frac{1-\Delta}{3+\Delta} \cdot \left(\frac{1}{d} - \frac{\alpha}{3} \right) \tag{4-33}$$

$$m = 1$$

and effective stress is found to be

$$\sigma_{ef} = \frac{1}{3} \cdot \frac{3+\Delta}{1-\Delta} \cdot \frac{\bar{\tau} - \alpha \bar{I}_1}{\left(\frac{1}{d} - \frac{\alpha}{3} \right)} \tag{4-34}$$

Chen and Han (1988) also emphasized a methodology for finding the effective visco-plastic strain by using the principle of visco-plastic work per unit volume assuming a homogeneous stress function in the form of

$$\dot{W}_{vp} = \Gamma < \phi(f) > m\bar{F} = \sigma_{ef} \dot{\varepsilon}_{vp} \tag{4-35}$$

and from Eq. (4-8)

$$\Gamma < \phi(f) >= \frac{\sqrt{\dot{\varepsilon}_{ij}^{vp} \dot{\varepsilon}_{ij}^{vp}}}{\sqrt{\frac{\partial g}{\partial \sigma_{ij}} \frac{\partial g}{\partial \sigma_{ij}}}} \tag{4-36}$$

Substituting Eqs. (4-27, 4-30, 4-31, 4-33, 4-34, and 4-36) into (4-35) yields:

$$\dot{\varepsilon}_{vp} = \frac{1}{\left[1 + 2 \cdot \left(\frac{1+\Delta}{1-\Delta} \right)^2 \left(\frac{\frac{1}{2d} + \frac{\beta}{3}}{\frac{1}{d} - \frac{\beta}{3}} \right)^2 \right]^{1/2}} \cdot \sqrt{\dot{\varepsilon}_{ij}^{vp} \dot{\varepsilon}_{ij}^{vp}} \tag{4-37}$$

It can be shown that for the triaxial state of stresses, Eq. (4-37) is reduced to uniaxial visco-plastic strain rate $\dot{\varepsilon}_{11}^{vp}$, and effective visco-plastic strain obtained by integrating Eq. (4-37) over time.

EFFECT OF ANISOTROPY ON MATERIAL DILATION

The anisotropic distribution of particles affects the relative sliding of particles, and hence it influences the dilation of granular materials. The relationship between anisotropy and dilation has been studied experimentally by several researchers (e.g., Oda 1972; Wan and Guo 2004). This section offers an analytical derivation of the relationship between the level of anisotropy and dilation.

The slope of the potential function for an isotropic material ($\Delta = 0$, $d = 1$) is defined by the slope β. In the modified stress space $\bar{I}_1 - \tau$, the slope of the plastic potential function is β^*, which is defined as the ratio of the volumetric strain rate $\dot{\varepsilon}_v^{vp}$ to the deviatoric strain rate $\dot{\varepsilon}_d^{vp}$ as follows:

$$\beta^* = -\frac{\dot{\varepsilon}_v^{vp}}{\dot{\varepsilon}_d^{vp}} \tag{4-38}$$

where

$$\begin{aligned} \dot{\varepsilon}_v^{vp} &= \dot{\varepsilon}_{11}^{vp} + 2\dot{\varepsilon}_{33}^{vp} \\ \dot{\varepsilon}_d^{vp} &= \frac{2}{3}\left(\dot{\varepsilon}_{11}^{vp} - \dot{\varepsilon}_{33}^{vp}\right) \end{aligned} \tag{4-39}$$

after manipulations using Eqs. (4-8, 4-30, and 4-39) and substituting into Eq. (4-38) it follows that

$$\beta^* = 3 \cdot \frac{\beta + \Delta\left(\frac{2}{d} - \frac{\beta}{3}\right)}{\frac{3}{d} - \Delta\left(\frac{1}{d} - \frac{4}{3}\beta\right)} \tag{4-40}$$

where for an isotropic material Eq. (4-40) reduces to β.

Fig. 4.7 shows the relationship between β^* and β. It can be seen that dilation increases with an increase in anisotropy represented by the Δ value. This is an important finding, as it captures the experimental measurements made by other researchers on granular materials. For example, Oda (1972) found that maximum dilation was obtained when particles were oriented in the horizontal direction while the major principal stress was imposed in the vertical direction. It is found in recent experimental measurements that Wan and Guo (2004) agreed with Oda's results.

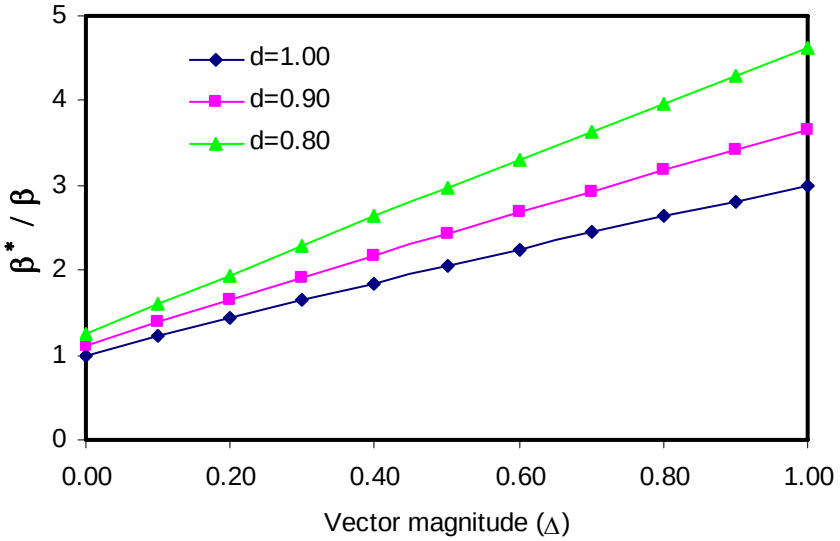

Figure 4.7. Relationship Between Dilation Parameters at Different Anisotropy Levels.

The dilation parameter β can be determined experimentally for the triaxial case using the ratio of lateral and uniaxial visco-plastic strain rate. Using Eqs. (4-8, and 4-30) the visco-plastic strain rate ratio can be given as:

$$\text{Viscoplastic Strain Rate Ratio} = \frac{-\dot{\varepsilon}_{33}^{vp}}{\dot{\varepsilon}_{11}^{vp}} = \frac{-\left(\frac{\partial g}{\partial \sigma_{33}}\right)}{\left(\frac{\partial g}{\partial \sigma_{11}}\right)} = \frac{(1+\Delta)}{(1-\Delta)} \cdot \frac{\left(\frac{1}{2d}+\frac{\beta}{3}\right)}{\left(\frac{1}{d}-\frac{\beta}{3}\right)} \qquad (4\text{-}41)$$

SUMMARY

This chapter includes the development of a microstructure elasto-visco-plastic nonassociated continuum model that links microstructure properties in terms of aggregate orientation and nucleation of voids to visco-plastic deformation of a material. The model was developed within the continuum framework and it has elastic and visco-plastic components. Hook's law is used to evaluate the elastic strain, while an extended Drucker-Prager yield surface is implemented to account for the visco-plastic component. The model has a damage parameter to account for the effect of void growth in softening the material and also has an anisotropy parameter to account for the aggregate distribution within the microstructure. The model also accounts for the dependency of HMA response on stress path direction by using the yield stress ratio parameter *d*.

The aggregate distribution is described by the vector magnitude (Δ), which quantifies the material anisotropy. Nucleation of air voids and microcracks is accounted for by a damage parameter based

on the effective stress theory. The damage parameter is found to be a function in effective visco-plastic strain and hydrostatic pressure. Material hardening as a result of microstructure constituent interaction is modeled using a hardening parameter that depends on effective visco-plastic strain. The effect of anisotropy is included in the elastic and visco-plastic components of the model, while damage is considered only in the visco-plastic phase.

The visco-plastic model was used to develop an analytical relationship between dilation and anisotropy. It was found that material dilation increases as the level of anisotropy increases.

CHAPTER V

FINITE ELEMENT IMPLEMENTATION AND PARAMETRIC ANALYSIS OF THE ELASTO-VISCO-PLASTIC CONTINUUM MODEL

INTRODUCTION

The advantage of using continuum modeling is the feasibility of its implementation in finite element (FE) analysis. The model is expressed in a time-step framework, and thus the concept of the viscous phenomenon is implemented through an incremental step.

Numerical integration including explicit and implicit methods of time integration for rate-dependent materials like hot mix asphalt (HMA) has been presented in many studies. Hughes and Taylor (1978), Peirce et al. (1984), Yoshimura et al. (1987), Szabo (1990), Auricchio and Taylor (1995), Marin and Mcdowel (1997), and Alfano et al. (2001) are examples of work that developed an integration algorithm for elasto-visco-plasticity problems.

Hughes and Taylor (1978) proposed an application for implicit methods that requires inversion of a compliance matrix. Peirce et al. (1984) proposed a one-step forward gradient time integration scheme that leads to a tangent stiffness type method for rate-dependent materials. Yoshimura et al. (1987) presented two alternate tangent modulus FE methods using a midpoint radial return implicit algorithm for rate-dependent visco-plastic material. Szabo (1990) compared different time integration algorithms and proposed a new method for calculating effective visco-plastic strain increments. Auricchio and Taylor (1995) proposed what is socalled a generalized visco-plastic model that has a visco rate-dependent behavior bounded by two rate-independent plasticity models. Marin and Mcdowel (1997) presented kinetic equation and dynamic yield surface approaches for a semi-implicit constitutive integration procedure for rate-dependent materials. Alfano et al. (2001) developed a general solution for solving elasto-visco-plastic problems by replacing the consistency condition with a relation between the visco-plastic multiplier and the viscous flow.

Elasto-visco-plasticity problems have made significant progress in the computational treatment of the relevant boundary value problem. Numerical algorithms for constitutive models have been mainly derived using plasticity theory and rely on classical operator methodology based on elastic prediction and plastic correction phases. One of the main tasks of computational plasticity is to integrate the rate equations ensuing from elasto-plasticity and visco-plasticity in a consistent, accurate, and efficient fashion (Heeres 2001). Simo and Hughes (1998) indicated that the numerical solution of elastic-visco-plastic boundary value problems is based on an iterative solution of the discretized momentum balance equations. They summarized the load/time-step solution into three main steps if the converged configuration at step n is given:

1. compute a new configuration for step (n+1) via an incremental motion that is used to compute incremental strains $\Delta\varepsilon$ at every stress point using the discretized momentum equations,

2. Update the state variables such as stress and internal paramters (σ_{n+1}, ϕ_{n+1}) and the visco-plastic strain component ε_{n+1}^{vp} by integration of the local constitutive equations for the given incremental strains $\Delta\varepsilon$, and
3. Check the balance of momentum using the new computed stresses and, if violated, iterations are performed by returning to step 1.

Step 2 is considered the central problem of computational plasticity, since it plays the main role of the constitutive equations in the computations. In FE analysis the elasto-visco-plastic constitutive equations are usually incorporated through a separate set of constitutive subroutines. The purpose of these subroutines at given a deformation history is to integrate the elastic-visco-plastic constitutive equations to return the corresponding stress history at every stress point.

This chapter includes implementation of the elasto-visco-plastic constitutive model in FE analysis using an implicit numerical integration algorithm, called Euler backward predictor, carried out in a time-step control. The equations that govern the evolution of stress, internal variables, inelastic deformation, and nonlinear parameters are discretized in an incremental format. The algorithm is an elaborating of the elasto-visco-plastic constitutive model presented previously in Chapter IV. The model is implemented in FE ABAQUS software to establish material behavior under a variety of loading and boundary conditions. Furthermore, the FE program is used to conduct a parametric analysis of the developed model to investigate the effect of model parameters, such as anisotropy, damage, hardening, stress path direction, and loading conditions, such as confinement, and loading rate, on the macroscopic visco-plastic deformation of HMA.

Currently the FE method is being utilized in several engineering problems for the purpose of understanding the role and contribution of engineering properties (e.g., material stiffness, material strength, and fracture energy) of the constituent materials of the composite in macroscopic response (e.g., deflections, load carrying, capacity, etc.).

A number of studies related to pavement analysis have been conducted using FE codes. ABAQUS is one of the most versatile FE programs and has been successfully implemented by Zaghloul and White (1993), Seibi et al. (2001), Papagiannakis et al. (2002), and others. ABAQUS is a general-purpose, two and three-dimensional, dynamic, production-oriented FE code designed to address linear and nonlinear structural problems. It provides a powerful and efficient way to analyze the nonlinear response of pavements to various loading patterns and allows for the following which can be used to simulate pavements:

- Complex and simple geometries;
- Various boundary conditions and interactions among constituents;
- Various loading conditions (static, dynamic, uniform and non-uniform contact pressure); and
- Various linear and nonlinear material properties for HMA.

The subroutine to define the material constitutive equation used by ABAQUS is called the user-defined material subroutine (UMAT). This subroutine facilitates incorporating of different models

without affecting the main code of the program. The advantage of using UMAT is to define the material's mechanical behavior.

DISCRETE FORMULATION OF THE CONTINUUM MODEL

This section describes the development of a numerical scheme for the constitutive model. The scheme relies on the classical operator split methodology based on elastic predictor and plastic correction phases. A fully implicit integration scheme is adopted to ensure accuracy and stability; thus, a backward Euler scheme for the time integration of the elasto-visco-plastic model is used. In the case of fully coupled elasto-visco-plastic behavior, the Newton-Raphson iterative scheme is associated to define available initial solutions. The proposed constitutive model is decomposed into elastic and visco-plastic strain components in incremental form as presented in Chapter IV:

$$\Delta\varepsilon = \Delta\varepsilon^{e} + \Delta\varepsilon^{vp} \tag{5-1}$$

where the elastic strain increment component can be defined according to Hooke's law and the visco-plastic strain rate is defined using Perzyna's visco-plastic model and a nonassociative flow rule as follows:

$$\Delta\sigma = D : \Delta\varepsilon^{e} \tag{5-2}$$

$$\Delta\varepsilon^{vp} = \Gamma \cdot < \phi(f) > \cdot \frac{\partial g}{\partial \sigma} \cdot \Delta t \tag{5-3}$$

and hence the stress increment is given by

$$\Delta\sigma = D : \left(\Delta\varepsilon - \Gamma \cdot < \phi(f) > \cdot \frac{\partial g}{\partial \sigma} \cdot \Delta t \right) \tag{5-4}$$

The numerical algorithm associated with the elasto-visco-plastic computation is based on the return mapping algorithm, which leads to an elastic predictor-visco-plastic corrector sequence. In elasto-visco-plasticity, the problem is solved by subdividing the time frame interval into a finite number of time steps. Let t be a fictitious time quantity. At time t_n it is assumed that the total ε_n and visco-plastic strain ε_n^{vp}, the stress fields σ_n, and the state variables κ_n, are converged and known at the initial time; that is,

$$\left\{ \varepsilon_n, \varepsilon_n^{vp}, \sigma_n, \kappa_n \right\} \qquad \text{Given parameters at time } t_n \tag{5-5}$$

Assuming the incremental displacement field $u_{n+1} - u_n$ is known, the basic problem is to update the fields described in Eq. (5-5) to t_{n+1} in a manner consistent with the elasto-visco-plastic constitutive equations. To integrate these equations over time, the general methodology of a return mapping algorithm for a time-dependent problems is integrated. At the initial time step, the trial elastic stress is computed using the elastic predictor problem that elaborates initial conditions known from the preceding time step. If the trial stress is located inside the yield surface then an elastic response

occurs, whereas a stress state outside the yield surface implies development of visco-plasticity. At this stage the visco-plastic corrector problem is solved by mapping the trial stress to the yield surface to maintain consistency.

The algorithmic value of a visco-plastic strain increment over a time interval $\Delta t = t_{n+1} - t_n$ can be defined as

$$\Delta\varepsilon^{vp} = \varepsilon^{vp}_{n+1} - \varepsilon^{vp}_{n} = \Delta t\left\{(1-\theta)\dot{\varepsilon}^{vp}_{n} + \theta\dot{\varepsilon}^{vp}_{n+1}\right\} \tag{5-6}$$

where $\dot{\varepsilon}^{vp}$ is the driven strain and θ is a coefficient that determines the integration scheme state. θ ranges between 0, for an explicit integration scheme, and 1, for fully implicit or backward Euler integration scheme. A mid-point rule is recovered if θ = 0.5, but it holds only for small strain increments. Rather the fully implicit scheme also ensures stability and accuracy for large strain increments. Therefore, throughout this chapter, the backward Euler scheme is adopted for the integration algorithm.

By using Eqs. (5-3, 5-4, and 5-6) the continuum model of evolution may be written in the following discrete form:

$$\begin{aligned}
&\varepsilon_{n+1} = \varepsilon_n + \Delta\varepsilon_{n+1} \\
&\sigma_{n+1} = D\ \left(\varepsilon_{n+1} - \varepsilon^{vp}_{n+1}\right) \\
&\varepsilon^{vp}_{n+1} = \varepsilon^{vp}_{n} + \Delta t\cdot\Gamma\left\langle\phi\left(f_{n+1}(\sigma,\varepsilon_{vp})\right)\right\rangle\frac{\partial g_{n+1}(\sigma,\varepsilon_{vp})}{\partial\sigma} \\
&\left(\varepsilon_{vp}\right)_{n+1} = \left(\varepsilon_{vp}\right)_{n} - \Delta t\cdot\Gamma\left\langle\phi\left(f_{n+1}(\sigma,\varepsilon_{vp})\right)\right\rangle\frac{\partial g_{n+1}(\sigma,\varepsilon_{vp})}{\partial\varepsilon_{vp}}
\end{aligned} \tag{5-7}$$

where D is the elastic stiffness matrix, and f and g are the yield and potential functions, respectively. ε_{vp} is the effective visco-plastic strain, which is necessary to update the internal state variable of the model evolutions.

A time-step-dependent visco-plastic consistency parameter is introduced that, according to the viscous flow in Eq. (5-3) it takes the form:

$$\dot{\gamma}^{vp} = \Delta t\cdot\Gamma\left\langle\phi\left(f_{n+1}(\sigma,\varepsilon_{vp})\right)\right\rangle \tag{5-8}$$

The algorithm starts by finding a trial value for f^{t}_{n+1}

$$f^{t}_{n+1} = F(\sigma^{t}_{n+1}) - \kappa\left(\varepsilon^{t}_{vp}\right)_{n+1} \tag{5-9}$$

where the trial stress can be given by:

$$\sigma_{n+1}^{t} = D : (\varepsilon_{n+1} - \varepsilon_{n}^{vp}) \tag{5-10}$$

Before the model evolution can be established, it is necessary to define the initiation of the viscous flow by introducing the following condition:

$$f_{n+1}^{t} = \begin{cases} = 0 \Leftrightarrow \text{Possibility for viscoplastic response} \\ < 0 \Leftrightarrow \text{Elastic response} \end{cases} \tag{5-11}$$

$f_{n+1}^{t} \le 0$ implies that elastic response occurs; hence, all the unknowns at t_{n+1} are set equal to the initial conditions. The trial value $f_{n+1}^{t} > 0$, which is nonadmissible during the visco-plastic flow, leads to a positive value for $\dot{\gamma}^{vp}$; hence, a visco-plastic correction is required (e.g., Ristinmaa and ottosen 2000; Alfano et al. 2001).

Analogous to the work by Alfano et al. (2001), who established an equivalent to the consistency condition in the plasticity problem, the following condition is introduced to evaluate the visco-plastic multiplier

$$\chi\left(\dot{\gamma}^{vp}\right) = f_{n+1}\left(\sigma, \varepsilon_{vp}\right) - \Theta\left(\dot{\gamma}^{vp}\right) = 0 \tag{5-12}$$

where

$$\Theta\left(\dot{\gamma}^{vp}\right) = \phi^{-1}\left(\frac{1}{\Delta t \cdot \Gamma}\dot{\gamma}^{vp}\right) \tag{5-13}$$

Substituting Eqs. (5-9, and 5-13) into Eq. (5-12) one gets

$$\chi\left(\dot{\gamma}^{vp}\right) = \frac{1}{1-\xi}\left(\bar{\tau} - \alpha \bar{I}_1\right) - \kappa - \left(\frac{\dot{\gamma}^{vp}}{\Delta t \cdot \Gamma}\right)^{1/N} \tag{5-14}$$

Eq. (5-12) replaces the condition of $f_{n+1} = 0$ in plasticity, and the Newton-Raphson iteration scheme is applied to solve the nonlinear form of this condition. The Newton scheme requires the derivative $\frac{\partial \chi}{\partial \dot{\gamma}^{vp}}$ to be determined, so by applying the chain rule in Eq. (5-14) one can obtain

$$\frac{\partial \chi}{\partial \dot{\gamma}^{vp}} = \frac{\partial F}{\partial \varepsilon_{vp}} \cdot \frac{\partial \varepsilon_{vp}}{\partial \dot{\gamma}^{vp}} - \frac{\partial \kappa}{\partial \varepsilon_{vp}} \cdot \frac{\partial \varepsilon_{vp}}{\partial \dot{\gamma}^{vp}} - \frac{\partial \Theta}{\partial \dot{\gamma}^{vp}} \tag{5-15}$$

Using Eqs. (5-13, and 5-14), the following functions are obtained:

$$\frac{\partial F}{\partial \varepsilon_{vp}} = -\frac{1}{(1-\xi)^2}\left(\bar{\tau} - \alpha \bar{I}_1\right)\frac{\partial \xi}{\partial \varepsilon_{vp}}$$
$$\frac{\partial \Theta}{\partial \dot{\gamma}^{vp}} = \left(\frac{\dot{\gamma}^{vp}}{\Delta t \cdot \Gamma}\right)^{1/N}\left(\frac{1}{\dot{\gamma}^{vp} \cdot N}\right) \tag{5-16}$$

The derivatives $\frac{\partial \xi}{\partial \varepsilon_{vp}}$ and $\frac{\partial \kappa}{\partial \varepsilon_{vp}}$ can be obtained from the evolution law of damage and hardening formulation described later in Chapter VI. By substituting Eq. (5-16) into Eq. (5-15) the derivative function becomes:

$$\frac{\partial \chi}{\partial \dot{\gamma}^{vp}} = \frac{\partial \varepsilon_{vp}}{\partial \dot{\gamma}^{vp}} \cdot \left(\frac{\partial F}{\partial \varepsilon_{vp}} - \frac{\partial \kappa}{\partial \varepsilon_{vp}}\right) - \left(\frac{\dot{\gamma}^{vp}}{\Delta t \cdot \Gamma}\right)^{1/N} \cdot \left(\frac{1}{\dot{\gamma}^{vp} \cdot N}\right) \tag{5-17}$$

Once the visco-plastic multiplier has been determined, the values of the unknowns are updated at time t_{n+1} according to the following:

$$\sigma_{n+1} = D : \left(\varepsilon_{n+1} - \varepsilon^{vp}_{n+1}\right)$$
$$\varepsilon^{vp}_{n+1} = \varepsilon^{vp}_{n} + \dot{\gamma}^{vp} n_{n+1} \tag{5-18}$$
$$\left(\varepsilon_{vp}\right)_{n+1} = \left(\varepsilon_{vp}\right)_{n} + \lambda \dot{\gamma}^{vp}$$

where λ is a scalar quantity that can be determined by using the equality $\dot{\gamma}^{vp} = \frac{\sqrt{\dot{\varepsilon}^{vp} \cdot \dot{\varepsilon}^{vp}}}{\sqrt{\frac{\partial g}{\partial \sigma} \cdot \frac{\partial g}{\partial \sigma}}}$, where $\lambda = \frac{\partial g_{11}(\sigma, \varepsilon_{vp})}{\partial \sigma_{11}}$.

ALGORITHMIC ELASTO-VISCO-PLASTIC TANGENT MODULI

Nagtegaal (1982) pointed out that using the algorithmic tangent moduli in the integration algorithm, as opposed to the continuum moduli, is essential to preserve the quadratic rate of asymptotic convergence that characterizes the iteration procedures in FE analysis. Pioneering work by Alfano et al. (2001) determined that the formulation of the algorithmic tangent moduli is expressed by using linearization of the elastic stress-strain relationship in Eq. (5-4), which yields:

$$d\sigma_{n+1} = D : \left(d\varepsilon_{n+1} - d\varepsilon^{vp}_{n+1}\right) \tag{5-19}$$

$$d\varepsilon^{vp}_{n+1} = \dot{\gamma}^{vp} \frac{\partial^2 g_{n+1}}{\partial^2 \sigma_{n+1}} d\sigma_{n+1} + d\dot{\gamma}^{vp} \frac{\partial g_{n+1}}{\partial \sigma_{n+1}} \tag{5-20}$$

In view of Eqs. (5-19, and 5-20) it follows that

$$d\sigma_{n+1} = \Xi_{n+1} : \left(d\varepsilon_{n+1} - d\dot{\gamma}^{vp} \frac{\partial g_{n+1}}{\partial \sigma_{n+1}} \right) \tag{5-21}$$

where

$$\Xi_{n+1} = \left[D^{-1} + d\dot{\gamma}^{vp} \frac{\partial g_{n+1}}{\partial \sigma_{n+1}} \right]^{-1} \tag{5-22}$$

To evaluate the quantity $d\dot{\gamma}^{vp}$, Eq. (5-12) is linearized so that one can obtain the visco-plastic consistency condition:

$$\frac{\partial g_{n+1}}{\partial \sigma_{n+1}} d\sigma_{n+1} = \frac{d\Theta_{n+1}}{d\dot{\gamma}^{vp}} d\dot{\gamma}^{vp} \tag{5-23}$$

Inserting Eq. (5-23) into Eq. (5-21), $d\dot{\gamma}^{vp}$ can be expressed as:

$$d\dot{\gamma}^{vp} = \frac{\Xi \frac{\partial g_{n+1}}{\partial \sigma_{n+1}} \cdot d\varepsilon_{n+1}}{\Xi \frac{\partial g_{n+1}}{\partial \sigma_{n+1}} \cdot \frac{\partial g_{n+1}}{\partial \sigma_{n+1}} + \frac{d\Theta_{n+1}}{d\dot{\gamma}^{vp}}} \tag{5-24}$$

Inserting Eq. (5-24) into Eq. (5-21), and differentiating with respect to ε_{n+1} yields

$$d\sigma_{n+1} = \left[\Xi - \frac{\Xi \frac{\partial g_{n+1}}{\partial \sigma_{n+1}}}{\Xi \frac{\partial g_{n+1}}{\partial \sigma_{n+1}} \cdot \frac{\partial g_{n+1}}{\partial \sigma_{n+1}} + \frac{d\Theta_{n+1}}{d\dot{\gamma}^{vp}}} \right] d\varepsilon_{n+1} \tag{5-25}$$

Defining

$$\begin{aligned} \Psi_{n+1} &= \Xi \frac{\partial g_{n+1}}{\partial \sigma_{n+1}} \\ \Sigma^{vp}_{n+1} &= \Xi \frac{\partial g_{n+1}}{\partial \sigma_{n+1}} \cdot \frac{\partial g_{n+1}}{\partial \sigma_{n+1}} + \frac{d\Theta_{n+1}}{d\dot{\gamma}^{vp}} \end{aligned} \tag{5-26}$$

and noting that the algorithmic tangent moduli is defined as $\frac{d\sigma_{n+1}}{d\varepsilon_{n+1}}$ it follows that

$$\mathrm{E}^{vp}_{n+1} = \Xi_{n+1} - \frac{1}{\Sigma^{vp}_{n+1}} \Psi_{n+1} \otimes \Psi_{n+1} \tag{5-27}$$

A summary of the integration algorithm for the evolution of the constitutive model is summarized in Figs. 5.1 and 5.2.

1- Assume internal state of strain and compute trial elastic stress

$$\varepsilon^{vp}_{n+1} = \varepsilon^{vp}_{n}$$

$$\varepsilon_{vp} = 0$$

$$\sigma^{t}_{n+1} = D : (\varepsilon_{n+1} - \varepsilon^{vp}_{n})$$

2- Check yield condition

$$f^{t}_{n+1} = F(\sigma^{t}_{n+1}) - \kappa\left(\varepsilon^{t}_{vp}\right)_{n+1}$$

IF $f^{t}_{n+1}\left(\sigma, \varepsilon_{vp}\right) \le 0$

Then $\sigma_{n+1} = \sigma^{t}_{n+1}$

$$\varepsilon^{vp}_{n+1} = \left(\varepsilon^{vp}_{n+1}\right)^{t} = \varepsilon^{vp}_{n} \Rightarrow \text{Go to step 1}$$

ELSE

3- Compute the visco-plastic multiplier using Fig. 5.2.

4- Update visco-plastic strain, effective strain and stress

$$\sigma_{n+1} = D : \left(\varepsilon_{n+1} - \varepsilon^{vp}_{n+1}\right)$$

$$\varepsilon^{vp}_{n+1} = \varepsilon^{vp}_{n} + \dot{\gamma}^{vp} n_{n+1}$$

$$\left(\varepsilon_{vp}\right)_{n+1} = \left(\varepsilon_{vp}\right)_{n} + \lambda \dot{\gamma}^{vp}$$

5- Compute algorithmic elasto-visco-plastic tangent moduli

$$\mathrm{E}^{vp}_{n+1} = \Xi_{n+1} - \frac{1}{\Sigma^{vp}_{n+1}} \Psi_{n+1} \otimes \Psi_{n+1}$$

$$\Psi_{n+1} = \Xi \frac{\partial g_{n+1}}{\partial \sigma_{n+1}}$$

$$\Sigma^{vp}_{n+1} = \Xi \frac{\partial g_{n+1}}{\partial \sigma_{n+1}} \cdot \frac{\partial g_{n+1}}{\partial \sigma_{n+1}} + \frac{d\Theta_{n+1}}{d\dot{\gamma}^{vp}}$$

$$\Xi_{n+1} = \left[(D)^{-1} + d\dot{\gamma}^{vp} \frac{\partial g_{n+1}}{\partial \sigma_{n+1}} \right]^{-1}$$

ENDIF

Figure 5.1. Numerical Integration Scheme for Elasto-Visco-plastic Continuum Model.

1- Initialize

$$\left(\gamma^{vp}\right)^0 = |TOL|$$

$$\left(\varepsilon_{vp}\right)_{n+1}^0 = \left(\varepsilon_{vp}\right)_n$$

2- Iterate

Do until $\left|\chi\left(\dot{\gamma}^{vp}\right)\right| < \text{TOL}$

2.1 Compute $\left(\dot{\gamma}^{vp}\right)^{k+1}$

$$\chi\left(\dot{\gamma}^{vp}\right)^k = \frac{1}{1-\xi}\left(\bar{\tau} - \alpha \bar{I}_1\right) - \kappa\left(\varepsilon_{vp}\right)_{n+1}^k - \left(\frac{\left(\dot{\gamma}^{vp}\right)^k}{\Delta t \cdot \Gamma}\right)^{1/N}$$

$$\frac{\partial \chi}{\partial\left(\dot{\gamma}^{vp}\right)^k} = \frac{\partial \varepsilon_{vp}}{\partial\left(\dot{\gamma}^{vp}\right)^k} \cdot \left(\frac{\partial F}{\partial\left(\varepsilon_{vp}\right)_{n+1}^k} - \frac{\partial \kappa}{\partial\left(\varepsilon_{vp}\right)_{n+1}^k}\right) - \left(\frac{\left(\dot{\gamma}^{vp}\right)^k}{\Delta t \cdot \Gamma}\right)^{1/N} \cdot \left(\frac{1}{\left(\dot{\gamma}^{vp}\right)^k \cdot N}\right)$$

$$\left(\dot{\gamma}^{vp}\right)^{k+1} = \left(\dot{\gamma}^{vp}\right)^k - \frac{\left[\chi\left(\dot{\gamma}^{vp}\right)^k\right]}{\left[\frac{\partial \chi}{\partial\left(\dot{\gamma}^{vp}\right)^k}\right]}$$

2.2 Update effective visco-plastic strain

$$\left(\varepsilon_{vp}\right)_{n+1}^{k+1} = \left(\varepsilon_{vp}\right)_n + \lambda\left(\dot{\gamma}^{vp}\right)^{k+1}$$

Figure 5.2. Newton-Raphson Numerical Scheme to Evaluate the Visco-plastic Consistency Parameter.

FINITE ELEMENT IMPLEMENTATION

ABAQUS was used to develop a quadrilateral two-dimensional four-node axisymmetric FE model. The algorithm described previously was programmed using the FORTRAN language in a user-defined material subroutine in the ABAQUS/Standard FE library, named UMAT. For the purpose of conducting a parametric analysis to study model parameter sensitivity, the FE model geometry with loading and constrained condition is presented in Fig. 5.3. Model constraint is applied on the lower and lateral sides to prevent deformation in the vertical and radial directions, respectively. The upper and opposite sides are left free for applying loading conditions. The model is loaded at a uniform vertical strain rate in addition to a confining pressure. The analysis is conducted in perturbation mode with a time increment. Stress and strain components are recorded at each time step.

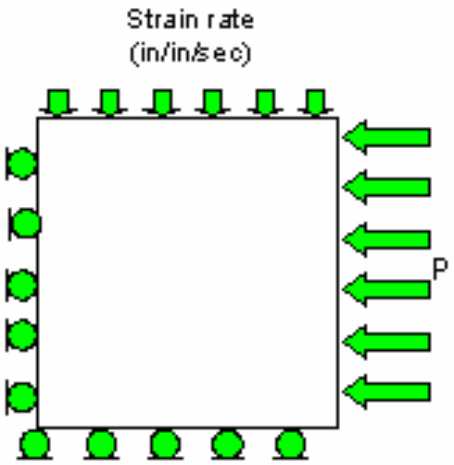

Figure 5.3. FE Geometric Model and Prescribed Boundary Conditions.

Parametric Analysis

Parametric analysis of the constitutive relationship is conducted using the FE model. Parametric analysis is useful to illustrate the efficiency of the constitutive relationship in capturing key features of the behavior of HMA. The parametric analysis illustrates the effects of yield function parameters α, β, d, and κ; microstructure parameters, Δ, and ξ; flow function parameters Γ and N; and loading conditions, such as confinement pressure I_1 and strain rate $\dot{\varepsilon}$, on the model response. In this section the role of each parameter is explained briefly and its influence on the model behavior is discussed. The values of the parameters used in this analysis represent the range of values obtained in Chapter VI based on experimental measurements.

Yield Function Parameters

When a material undergoes viscous deformation the yield surface geometry changes according to the hardening rule that governs this phenomenon. Several hardening rules such as isotropic, kinematic, and mixed hardening can describe the growth of the yield surface. In this study, the model parameter κ describes the isotropic hardening of the material. The parameter controls the size of the yield surface, which increases with increasing κ. κ is a stress-independent parameter, but it is generally defined as a function of the deformation history. Throughout the loading if the material continues to harden the yield surface continues to grow. In a typical stress-strain relationship, the parameter remains constant during the elastic range, in which it reduces to initial hardening ($\kappa = \kappa_o$). However, as soon as the material initiates viscous flow, the hardening increases until the material reaches its ultimate strength ($\kappa = \kappa_n$) as implied in Fig. 5.4(a). In the degradation (softening) phase, once the material starts to soften the hardening stabilizes and the evolution of damage is responsible for the softening of the material. In this study, softening is due to multiplying the κ value by $(1-\xi)$

where ξ is the damage parameter. As shown in Fig. 5.4(b), this parameter controls both the magnitude and location of the ultimate strength.

Fig. 5.5(a) implies that the model parameter α determines the slope of the yield surface, which increases with increasing α. α is a stress-independent parameter, that could be a function of visco-plastic strain and strain rate. α is a parameter that reflects the frictional properties of the material, which increase with increasing α. The evolution of α is the result of changes in the aggregate structure associated with friction and dilation when the material is under confinement. An increase in α causes an increase in the material yielding stress and ultimate strength as shown in Fig. 5.5(b).

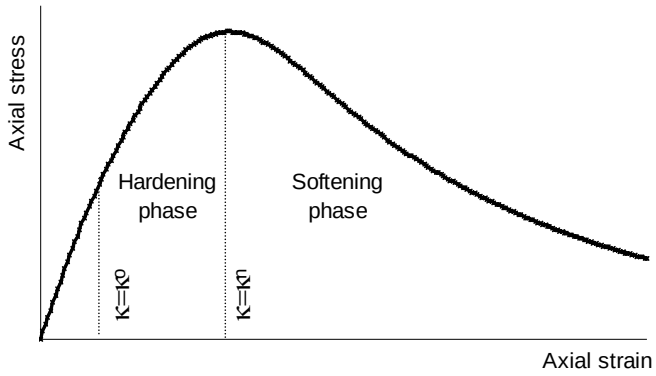

a) Evolution on Typical Stress-Strain Relationship

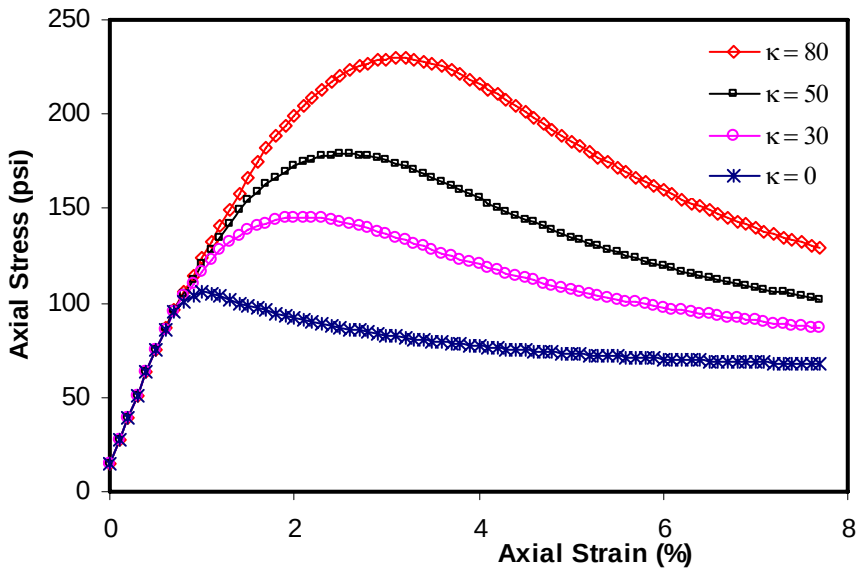

b) Influence on Stress-Strain Relationship

Figure 5.4. Effect of Hardening / Softening Parameter.

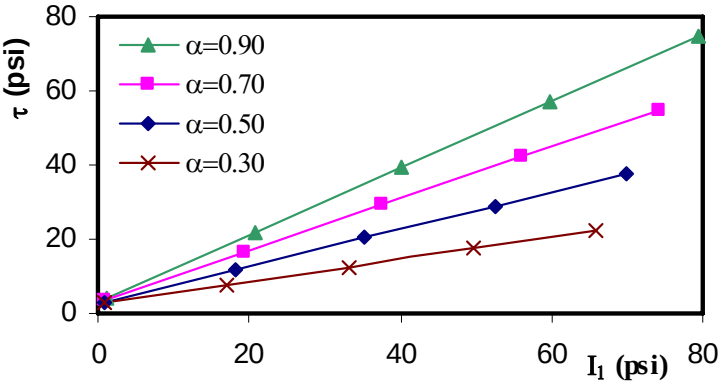

a) Influence on Drucker-Prager Yield Surface

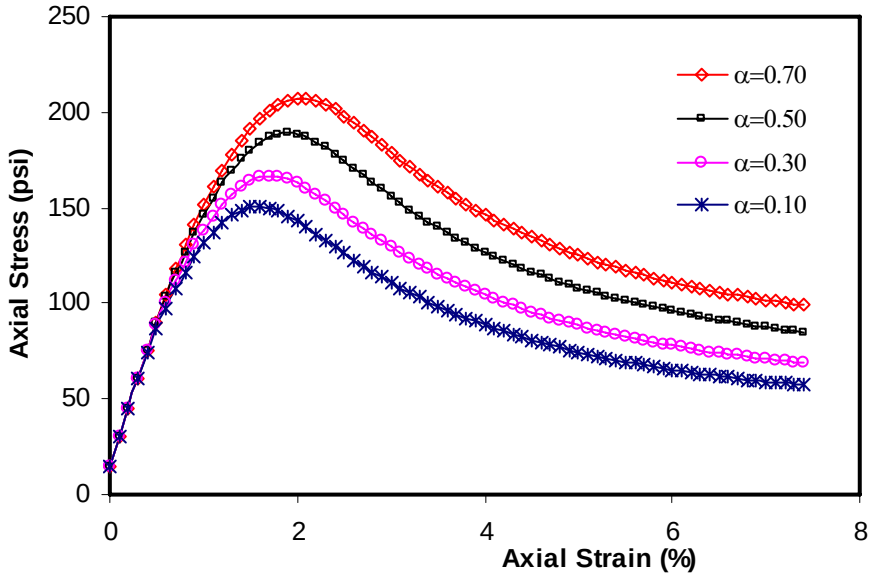

b) Influence on Stress-Strain Relationship

Figure 5.5. Effect of Frictional Parameter .

The parameter β is the slope of the visco-plastic potential surface that is associated with viscous flow. Granular materials in general develop dilation when they are subjected to deviatoric stresses. Experimental observations indicate that the associated flow rule is not applicable for granular materials (e.g., Zeinkiewicz et al., 1975; Oda and Nakayama 1989). Therefore, a potential surface exists and the slope of this surface is determined by the parameter β, which is consequently lower than the slope of the yield surface α. β reflects the dilative potential of the material and therefore, influences the proportions of the volumetric and deviatoric strains. As expected, Fig. 5.6 indicates that as β increases the material exhibits more volumetric change. Recall from Chapter IV, that the dilation parameter in the new model β^* becomes higher than β as the material becomes more anisotropic.

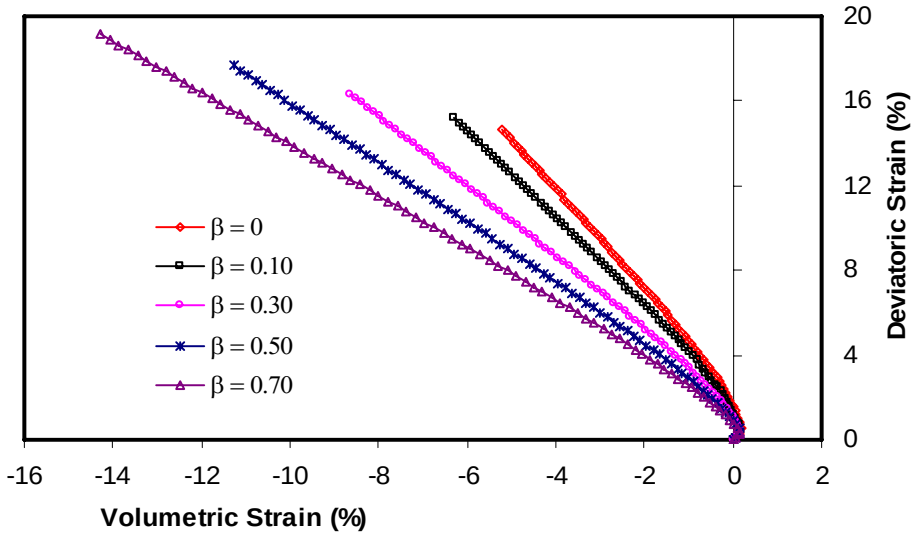

Figure 5.6. Influence of Dilation Parameter on Proportion of Deviatoric and Volumetric Strain.

Microstructure Parameters

Vector magnitude Δ is an internal material parameter that reflects the directional distribution of the microstructure. Δ is a measure of the preferred orientation of particles. Increasing anisotropy increases the percentage of particles oriented in the horizontal direction, leading to more contacts in the vertical direction. Development of contacts increases resistance to deformation in vertical direction. Therefore, Fig. 5.7 illustrates that anisotropy tends to increase the stability of the material in the uniaxial direction.

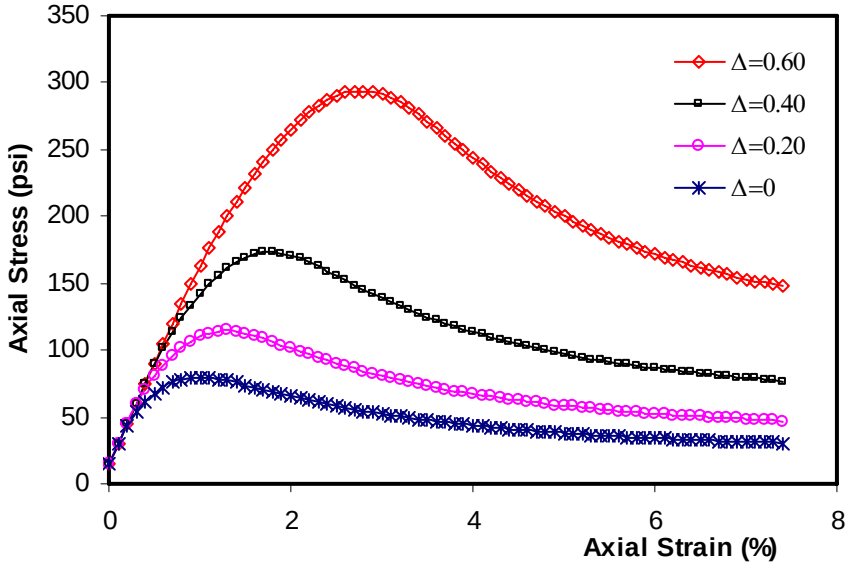

Figure 5.7. Influence of Anisotropy on Stress-Strain Relationship.

The damage parameter ξ accounts for softening of the material due to formation of cracks and air voids associated with viscous flow. ξ is defined based on the effective stress theory as the ratio of the area of voids to the total cross-sectional area of a specimen. The shape of the stress-strain curve in the softening phase reflects the level of damage. Materials with no damage create a stable response represented by an asymptotic response, while those with damage produce a reduction in the stresses; the percentage of the reduction depends on the damage level as illustrated by Fig. 5.8.

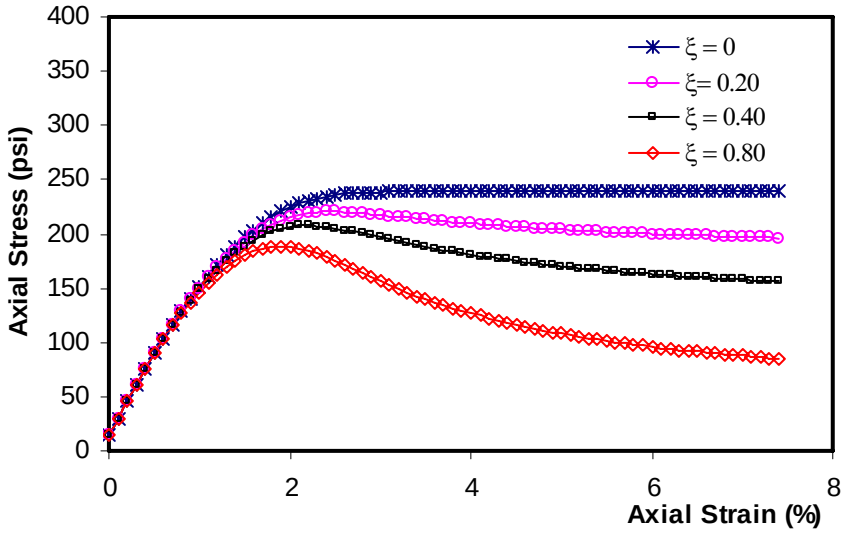

Figure 5.8. Stress-Strain Relationship at Different Damage Levels.

Flow Function Parameters

The viscosity parameter Γ controls the growing rate of the yield surface. It can be seen from Fig. 5.9(a) that a slight change in the viscosity parameter Γ could produce a significant change in the stress-strain relationship. As the parameter decreases, the yield surface size increases and the ultimate strength is reached at a higher strain level. This parameter operates only when the material exhibits visco-plastic flow, and when the condition $\frac{1}{\Gamma} \Rightarrow 0$, the rate-independent elastoplastic model is recovered as shown in Fig. 5.9(b). Γ is associated with the overstress function to account for stresses outside the elastic domain. Fig. 5.9(b) illustrated the influence of the parameter on viscous flow of the material. Visco-plastic strain is found to increase as the viscosity parameter increases. This observation is true as indicated by Eq. (5-3).

The model parameter N controls the shape of the overstress function and the level of the non-linearity of the Perzyna model. Fig. 5.10(a) implies that for $N = 1$ Perzyna model reduces to the linear viscous flow formulation while for $N > 1$ viscous flow becomes non-linear. By definition N is a material constant which accounts for the rate sensitivity of the material. In general, for plastic materials the parameter N ranges from 1 to 10 (Khaleel et al. 2001). A value less than one is not applicable as indicated by Fig. 5.10(b) where no visco-plastic strain is detected in uniaxial and lateral directions.

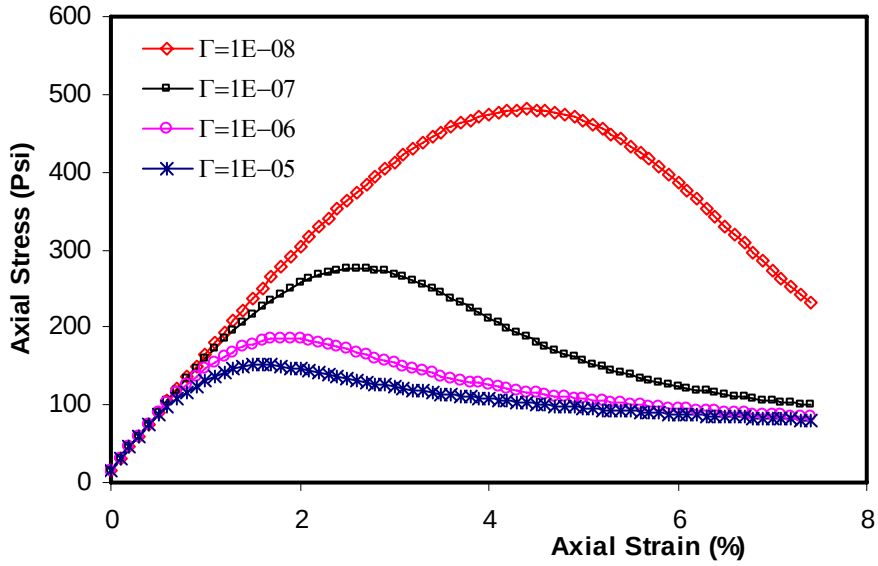

a) Influence on Stress-Strain Relationship

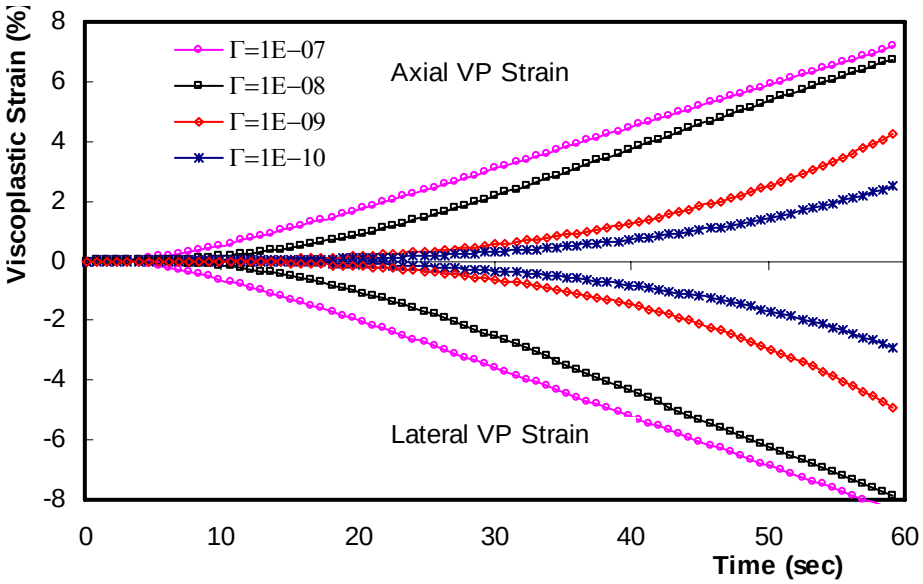

b) Influence on Visco-plastic Deformation

Figure 5.9. Effect of Viscosity Parameter.

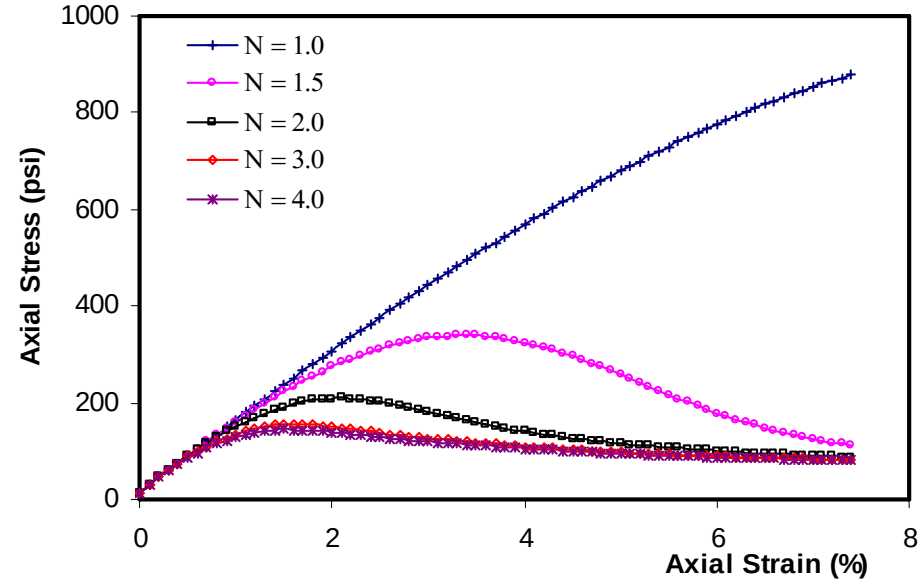

a) Influence on Stress-Strain Relationship

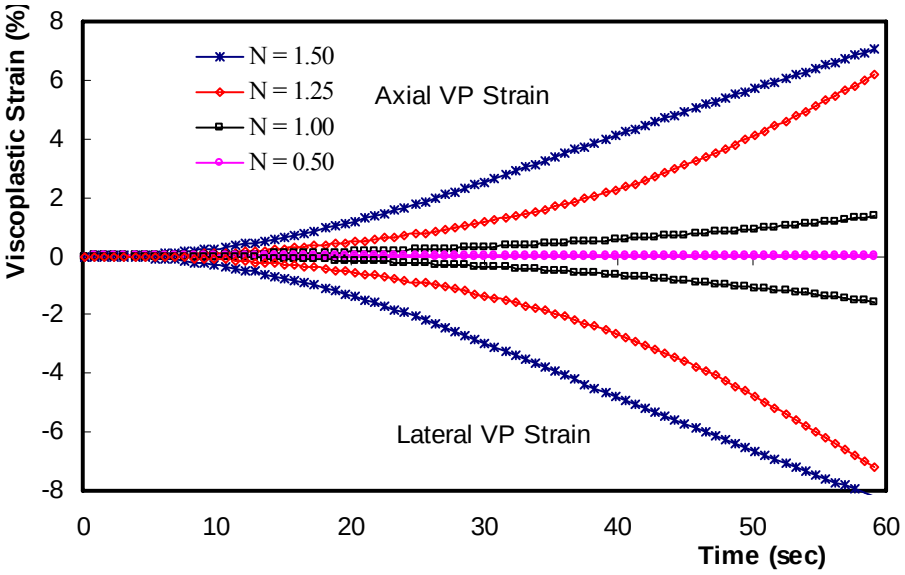

b) Influence on Visco-plastic Deformation

Figure 5.10. Effect of Rate Sensitivity Parameter.

Loading Conditions Effect

The model parameter *d* determines the shape of the yield surface in the deviatoric plane. When *d* = 1 the yield surface is a complete circle analogous to the Von Mises yield surface, and as *d* decreases the surface results in a triangular surface. *d* is a material parameter representing the sensitivity of

yield behavior to the hydrostatic pressure I_1. The parameter d is the ratio of yield stress in uniaxial tension to that in uniaxial compression. The parameter controls the material behavior according to the state of stress. Material under compression or tension shows equal response when $d = 1$ (circular yield surface), while different response is detected at $d = 0.778$, as shown in Fig. 5.11(a). Changes in the value of d may also produce unrealistic shapes for the yield surface. For example, at $d = 0.5$ the surface loses its convexity geometry. Fig. 5.11(b) shows that changes in the anisotropy level control the response in the uniaxial axis σ_1, leaving the lateral axes with minor changes. Appropriate values of the yield stress ratio d alter the compression stress response (if $\theta = 0°$) so that compressive stress is higher than that in tension stress.

The Drucker-Prager yield surface is projected in the deviatoric plane as shown in Fig. 5.11 where ρ is the radius from the origin to the yield surface and θ is the measured angle from the radius to the σ_1-axis. According to the microstructure tensor, anisotropy exhibits directional dependency for all ranges of the angle θ. It also provides yield stress dependency under the same loading condition according to the imposed plane. For example, the tension yield stress at plane $\theta = 60°$ is different from that corresponding to plane $\theta = 180°$. Fig. 5.11(b) shows the projection of the yield surface on the deviatoric plane at $d = 0.778$. The yield stress in the axial direction (direction 1) increases as the material anisotropy increases, while no change in stress is recorded for the radial direction (directions 2 and 3).

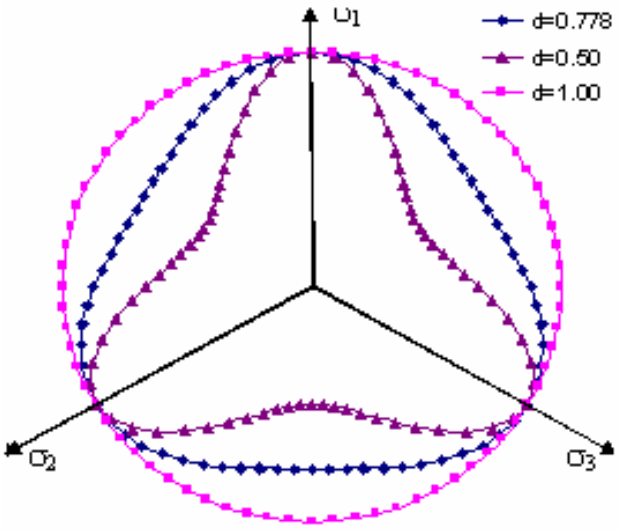

a) Influence of Yield Stress Ratio

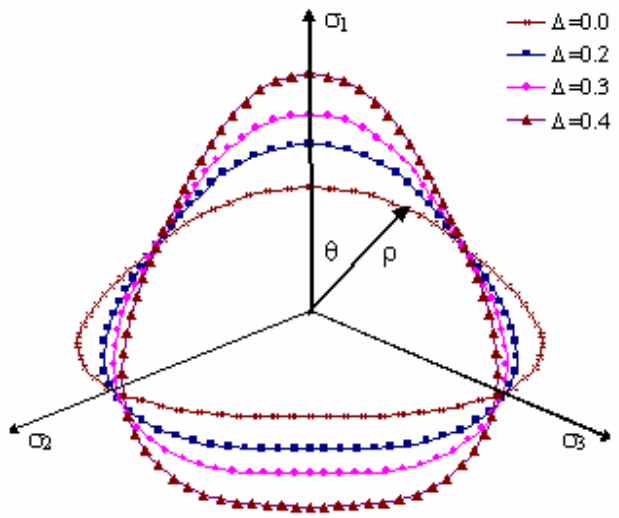

b) Influence of Anisotropy

Figure 5.11. Effect of Yield Stress Ratio and Anisotropy on Yield Surface Geometry at the Deviatoric Plane.

HMA is a rate-dependent material. Its properties such as Young's modulus and ultimate strength are highly dependent on loading rate. Fig. 5.12 shows the dependency of the material on the rate of loading. Increasing the loading rate increases the material strength. The proposed model indicates that the material strength is analogous to the behavior of granular materials. Fig. 5.12 shows the axial stress versus the axial strain and radial strain for different strain rates and indicates that the material is sensitive to the stress path captured by the strength in compression versus tension.

Stresses in general are sustained by aggregate-aggregate and binder-aggregate interactions. Each interaction contributes to the ultimate strength according to the stress path. Aggregate-aggregate interaction carries most of the stress in compression while its contribution against tensile load is minimal. Binder-aggregate contributes to sustain tensile load, but its contribution is relatively small. This observation is noticed in the hardening evolution zone in compression versus tension.

Lateral strain consequently expresses similar behavior to uniaxial strain, as shown in Fig. 5.12(b). Higher strength and relatively more stable response are obtained with compressive loads. Fig. 5.12 indicates that material deterioration starts early in the lateral direction as can be shown in the strain level corresponding to the ultimate strength. This observation can be explained by material anisotropy, as anisotropy increased the stiffness in the uniaxial direction.

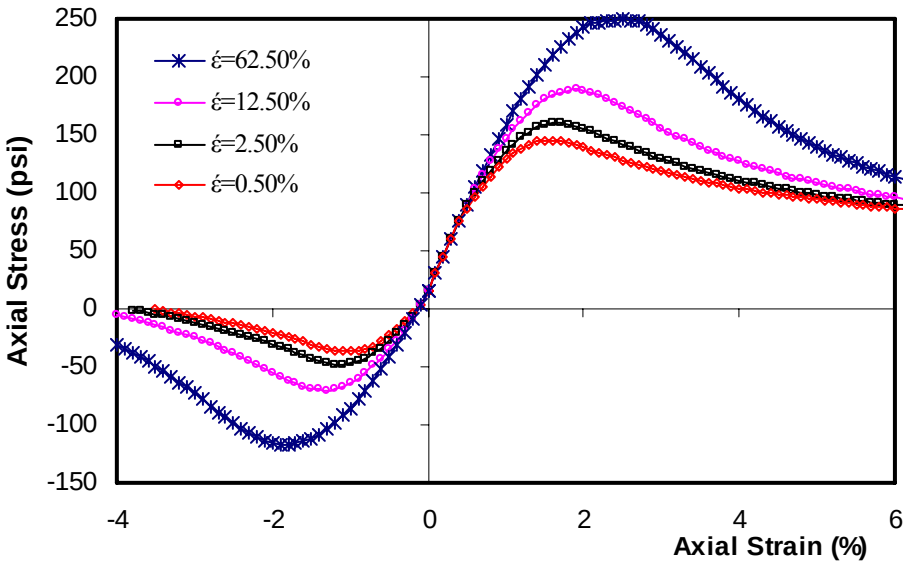

a) Influence on Axial Stress- Axial Strain Relationship

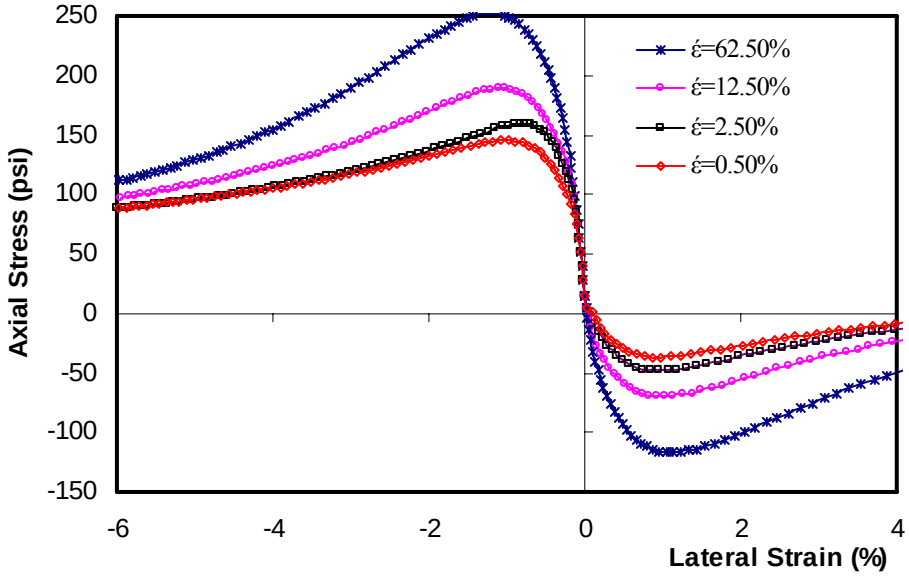

b) Influence on Axial Stress- Lateral Strain Relationship

Figure 5.12. Effect of Strain Rate **.**

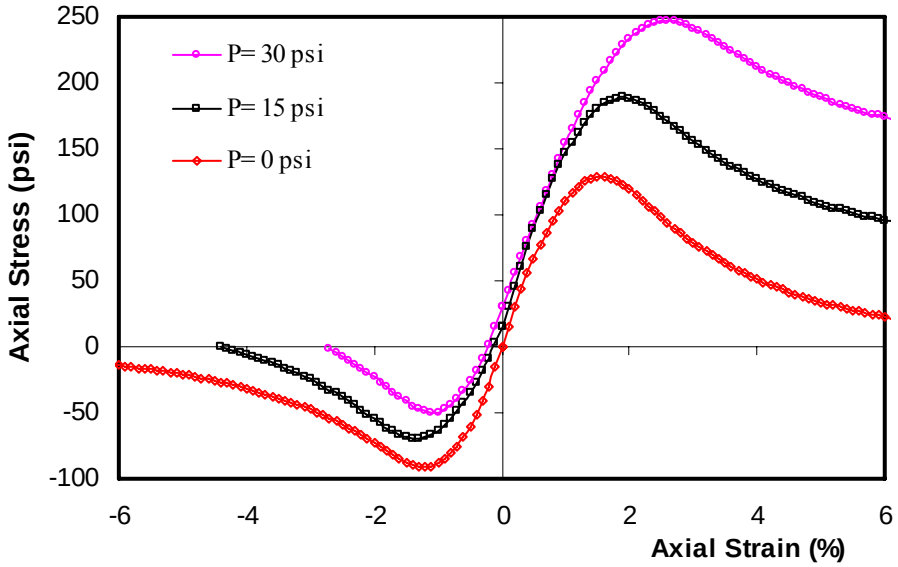

a) Influence on Axial Stress- Axial Strain Relationship

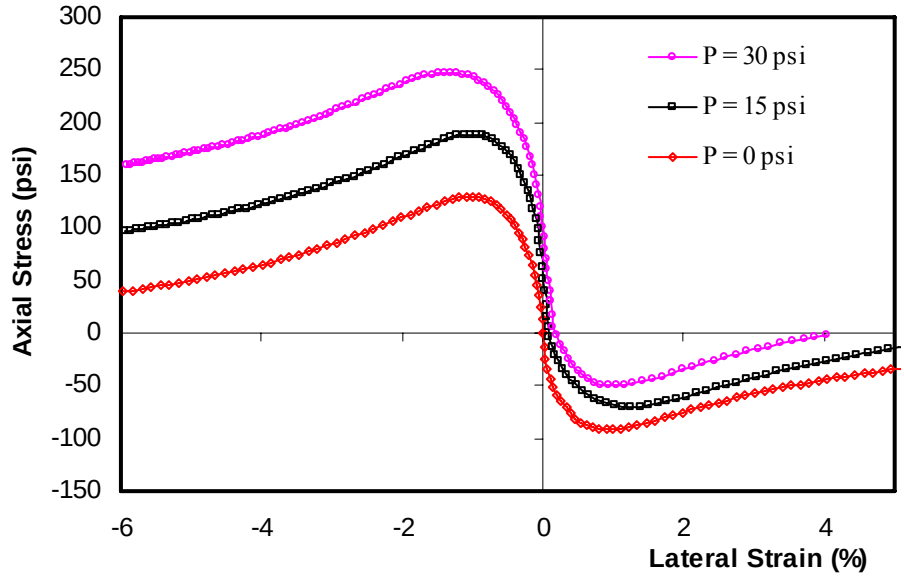

b) Influence on Axial Stress- Lateral Strain Relationship

Figure 5.13. Effect of Confining Pressure .

The material generates different responses under a variety of confining pressures. Confining pressure provides stability to the material to sustain an applied load. On the contrary, when the material undergoes extension stresses the minimum strength is attained when the material is subjected to a high level of confinement as shown by Fig. 5.13. The confining pressure improves the stability of the material during compaction but this stability declines in tension. Lateral strain, on the other hand, behaves similar to uniaxial response. Analogous to the behavior with respect to the rate of loading and recognizing the existence of material anisotropy, the material exhibits more stability in the uniaxial direction.

SUMMARY

The developed elasto-visco-plastic model is incorporated in the UMAT subroutine available in ABAQUS. Implementation of the model in this routine is in the form of a fully implicit algorithm with time-step control for numerical integration of the internal state variables. Implicit integration in the form of the backward Euler scheme provides an efficient local solution to the internal state. The Newton-Raphson iterative scheme is utilized to define available initial solutions. The numerical algorithm associated with the elasto-visco-plastic treatment is based on the return mapping concept, which leads to an elastic predictor-plastic corrector algorithm. The algorithm includes a consistency condition analogous to plasticity to evaluate the visco-plastic multiplier. As a result of the implicit numerical integration, algorithmic tangent moduli are made available to the global ABAQUS solution which results in a quadratic rate of convergence in the global iteration to reduce the computational time in FE analysis.

A parametric analysis was conducted to investigate the effect of key parameters in the model on material response. The results clearly show that the model is sensitive to material hardening (κ), dilation (β), anisotropy (Δ), void nucleation and growth (ξ), and stress path direction (d). The study also shows that increasing loading rate and confinement causes increasing in yield stress.

An increase in the anisotropy level causes an increase in the yield stress of the material (increases its strength) in the axial direction normal to the preferred orientation of particles. The yield strength in the direction parallel to the orientation of particles decreases slightly with an increase in anisotropy.

CHAPTER VI

EXPERIMENTAL EVALUATION OF MODEL PARAMETERS

INTRODUCTION

This chapter discusses the experimental and analytical methodologies used to determine the model parameters for the yield function, flow rule, and damage function. The parameters were determined for three mixes prepared using different aggregates compression and extension triaxial tests at different confining pressures and strain rates were used to evaluate model parameters. The parameters were used in the finite element (FE) analysis, and the results of FE simulations were compared with experimental measurements. FE also is used to simulate pavement section and predict rutting profile due to wheel loads.

SPECIMEN PREPARATION AND TESTING PROGRAM

Twenty four HMA specimens of granite, limestone, and gravel mixes were fabricated using the Servopac gyratory compactor to a target air void content of 7.0 %. All three mixes were prepared according to the Superpave specifications for high traffic roads (10 - 30 million Equivalent Single Axial Loads (ESALs)). Mix volumetrics laboratory data for these mixes are tabulated in Table 6.1, while Fig. 6.1 shows the gradation of the three aggregates used in the mixes.

Table 6.1. Mix Design Factors for the Three Asphalt Mixes (after Masad et al. 2003).

Mix	**Gravel**	**Limestone**	**Granite**
Avg. Measured Air void, %	7.04	6.7	6.89
SD of AV	0.48	0.25	0.30
Binder Type	PG 64-22	PG 64-22	PG 64-22
Binder Content, %	3.6	4.85	4.86
Maximum Specific Gravity	2.484	2.47	2.471
Specimen Height, mm	155	157.5	157.5
Sieve Size, mm	**Percent Passing**		
12.5	100	98.8	98.8
9.5	91.748	79.5	79.5
4.75	48.22	46.2	46.2
2.36	32.71	31.6	31.6
1.18	27.96	24.5	24.5
0.6	22.26	17.8	17.8
0.3	9.75	11.2	11.2
0.15	3.94	6.3	6.3
0.075	2.95	1.5	1.5
Pan	0	0	0

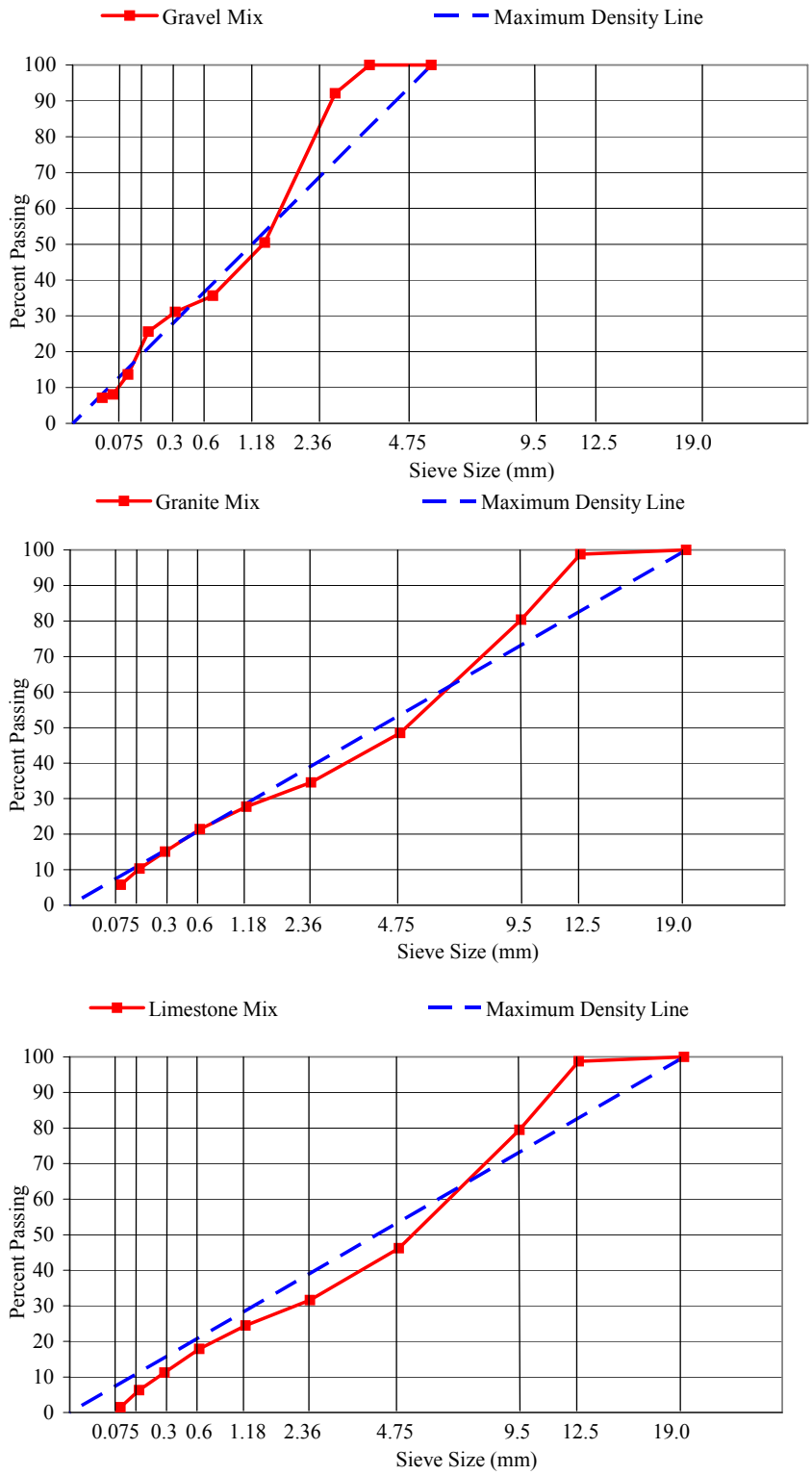

Figure 6.1. 0.45 Power Gradation Charts of the Three Mixes (after Masad et al. 2003).

Laboratory experiments conducted in this study were strain-controlled triaxial compressive strength tests at five displacement rates and three confining pressures and triaxial tensile strength tests at three displacement rates and three confining pressures. One of the main advantages of using the triaxial test is that the axial and radial (or volumetric and shear) strains can be determined relatively easily. Radial ring-type LVDTs were attached to a specimen at mid-height, while axial strains were measured by vertical LVDTs along a specimen side. Axial LVDTs were 120^o apart from each other. For the compressive strength test, the specimens were deformed at strain rates of 0.0660%/min, 0.318%/min, 1.60%/min, 8.03%/min, and 46.4%/min and at confining pressures of 0, 15, and 30 psi. For the tensile strength tests, the same confining pressures and three axial loading rates of 0.0660%/min, 0.318%/min, and 1.60%/min were used. All specimens were loaded up to an axial strain of 8 % or until failure, whichever occurred first. All tests were conducted at a temperature of 130^o F. Two replicates of each mix were tested for each loading condition, and axial and radial stresses and strains were recorded throughout testing.

EVOLUTION LAWS FOR THE MODEL PARAMETERS

Damage

The physical mechanisms of interaction between damage and viscous deformation are complicated in nature and may not be modeled through one phenomenological constitutive model due to the nature of the material. Asphalt pavement materials usually fail because of nucleation, growth, and coalescence of damage following work hardening and stiffening of the microstructure. Experimental observations show that accumulation of microdamage has a tendency to form macroscopically localized damage, which is a precursor to failure. This progressive physical process of degradation of the material mechanical properties up to complete failure is commonly referred to as damage.

Ductile damage is basically characterized by three mechanisms (Thomason 1990; Hertzberg 1996):

- Nucleation of microscopic voids that initiates at the particle-particle and particle-matrix interfaces;
- Growth of microcracks when the material undergoes viscous deformation, and hydrostatic pressure; and
- Connectivity of the growing microvoids with neighboring ones leading to decreased intact area and causing reduction in material load-carrying capacity.

This study proposed to model the phenomenon of strain softening primarily due to the damage effect. In this chapter, similar to the work of Perzyna's analysis, damage was assumed to be a function of the confining pressure and effective visco-plastic strain as follows:

$$\xi = f(I_1, \varepsilon_{vp}) \tag{6-1}$$

where ξ is the damage parameter, I_1 is the first invariant of stresses to account for the confining pressure, and ε_{vp} is the effective visco-plastic strain. It is implied from the triaxial test results from

this study that confining pressure minimizes the growth of air voids and cracks, and hence reduces damage as illustrated in Fig. 6.2.

The model parameter ξ is an indicator of the damage percent in the material. The parameter is incorporated in the model through the effective stress theory presented by Kachanov (1958), who introduced for the isotropic case a one-dimensional damage variable. In this theory, damage is interpreted as the effective surface density of microdamage per unit volume. This concept is based on considering a fictitious undamaged configuration of a body and comparing it with the actual damaged configuration.

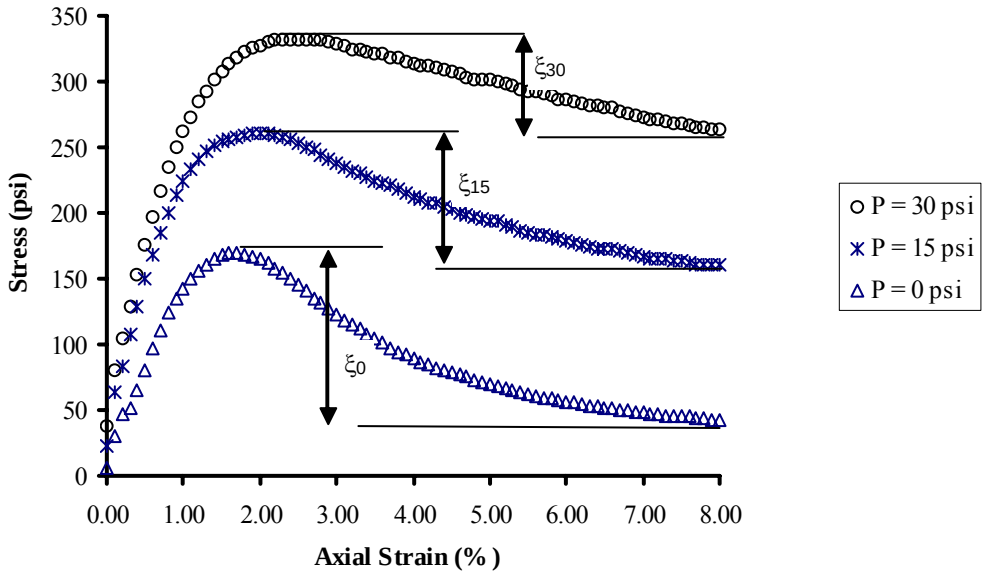

Figure 6.2. Influence of Confining Pressure on Material Softening.

Therefore, a damaged material exposed to a stress σ exhibits the same deformation behavior as an undamaged material exposed to an effective stress σ^e

$$\sigma^e = \frac{\sigma}{1-\xi} \tag{6-2}$$

where according to the definition above, damage models can be implemented in deformation models by replacing stress with effective stress.

Desai (1998) adopted an evolution form for the disturbance or damage of the material under monotonic loading. The study proposed that damage evolution is a function of the ultimate damage at high strain level and plastic deviatoric strain. An exponential form has been used to simulate the

degradation response as the material passes the ultimate stresses. The function in Eq. (6-3) used in this study is similar to the one proposed by Desai (1998):

$$\xi = \exp(\xi_1 \cdot \frac{I_1}{3}) \cdot \left[1 - \exp(\xi_2 \cdot \varepsilon_{vp} + \xi_3 \cdot \frac{I_1}{3})\right] \quad (6\text{-}3)$$

where ξ_1, ξ_2, and ξ_3 are coefficients to be determined experimentally. The first exponential term controls the asymptotic limit of the function. The last term, which includes the confining pressure, controls the damage rate of growth.

Sousa and Weissman (1995) emphasized that HMA exhibits different response under tension and compression. Under compression, the material goes through strain hardening due to the newly formulated microstructure with more aggregate contacts trying to resist the applied load. On the other hand, work softening occurs when the aggregate rotation and sliding become high enough to cause cohesive and/or adhesive failure within the microstructure, resulting in microcracks (Masad et al. 2003). The situation is different in tensile tests, where the formation of aggregate contacts, and consequently hardening, is much lower than with compressive loading. Opening of cracks and voids is promoted by the applied tensile stresses even before excessive sliding of particles. In other words, softening in tension occurs earlier and at a faster rate than in compression. Therefore, it is proposed to introduce two sets of parameters to account for damage evolution in compression and in tension.

Anisotropy

The initial value of the vector magnitude depends on aggregate characteristics, aggregate gradation, and the compaction method used to prepare the specimen. Dessouky et al. (2003) presented experimental results showing that the initial value and the evolution of the vector magnitude during compaction are functions of aggregate shape and gradation. The vector magnitude Δ describes the aggregate orientation distribution measured on two-dimensional images and is a function of aggregate shape properties and distribution. Δ quantifies the level of anisotropy measured on two-dimensional vertical of asphalt pavement section using the imaging analysis. The vector magnitude was determined using Image Analysis Techniques (IAT) developed by Tashman et al. (2001) on four images of cut sections of two HMA specimens selected randomly.

Tobita (1989) concluded that preferred orientation of sand particles exhibits minor change when the material undergoes inelastic deformation. This observation was later verified by Tashman (2003), who showed that aggregate orientations in HMA specimens did not change significantly when the material experienced inelastic deformation. Thus, it is proposed to utilize the initial vector magnitude only to describe the HMA inherent anisotropy.

Work Hardening and Frictional Parameters

The evolution laws for α and κ are postulated based on experimental measurements. α is a parameter that reflects the material frictional properties, whereas κ is a hardening parameter that

reflects the combined effect of the cohesion and frictional properties of the material. To illustrate the evolution of the hardening parameters, the yield surface is plotted in the $I_1 - \tau$ plane as shown in Fig. 6.3. The results show that α tends to change only at small strain levels, while the evolution of κ is more pronounced. This finding is consistent with the findings of Tan et al. (1994). Therefore, α is assumed to be constant.

The evolution of κ is associated with hardening resulting from deformation in the binder, which causes changes in the aggregate contact interface and aggregate frictional properties due to the strain driven in the material. Hence, it is proposed to account for the evolution of the hardening parameter κ, based on the experimental measurements and motivated by the work of Dafalias (1990) as shown in Eq. (6-4):

$$\kappa = \kappa_0 + \kappa_1 \left\{1 - \exp(-\kappa_2 \cdot \varepsilon_{vp})\right\} \tag{6-4}$$

where κ_0 defines the initial yield surface and κ_1 and κ_2 are material coefficients that account for the effect of effective visco-plastic strain on the material work hardening. The exponential form by itself provides an asymptotic response in the stress-strain relationship once the strain level passes the peak stresses.

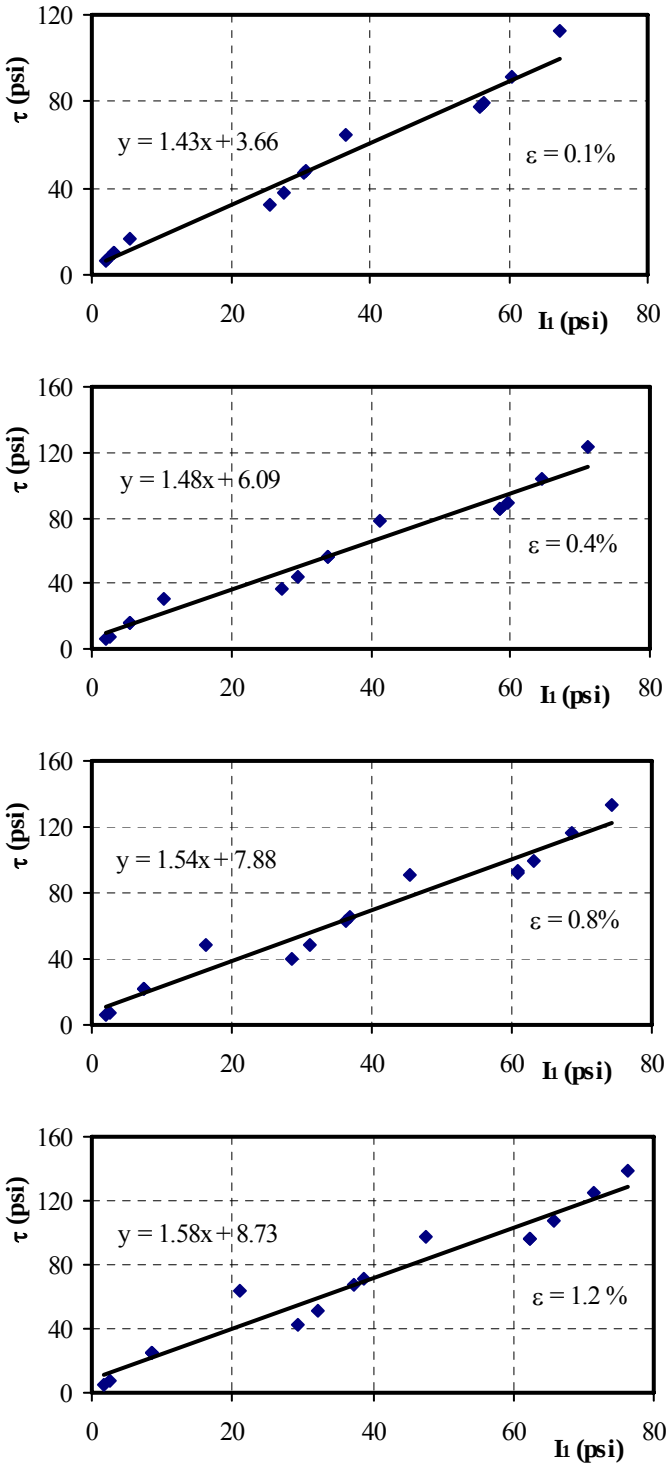

Figure 6.3. Changes in α and κ During Deformation at Different Deformation Levels.

DETERMINATION OF THE MODEL PARAMETERS

A systematic procedure was developed to determine the model parameters. As shown in Fig. 6.4, a typical stress-strain response obtained in the experiment is divided into three zones. The first zone is the linear response, where initiation of the visco-plastic flow has not taken place. The linear zone represents the visco-elastic behavior of the material where the modulus, E, and Poisson's ratio, ν, as a function of time can be determined.

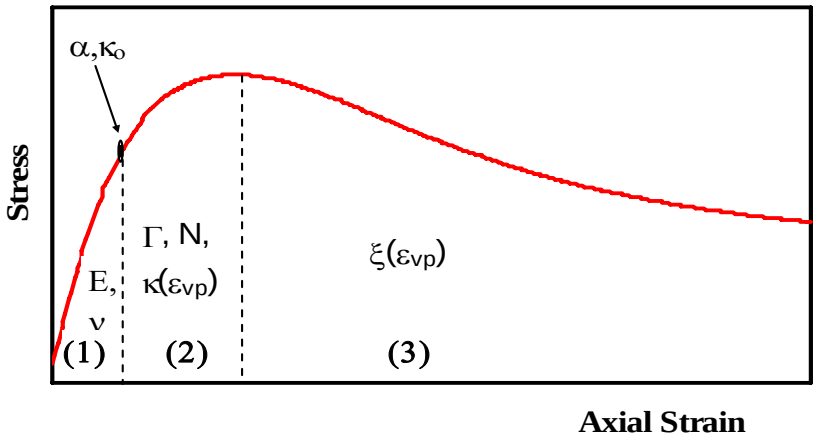

Figure 6.4. Stress-Strain Relationship Zones for Model Parameters Identification.

Experimental measurements indicated that elastic modulus varies with respect to loading rate. Material that undergoes a small rate of loading exhibited a small elastic modulus. Fig. 6.5 indicates that granite had the largest modulus, while gravel had the smallest modulus.

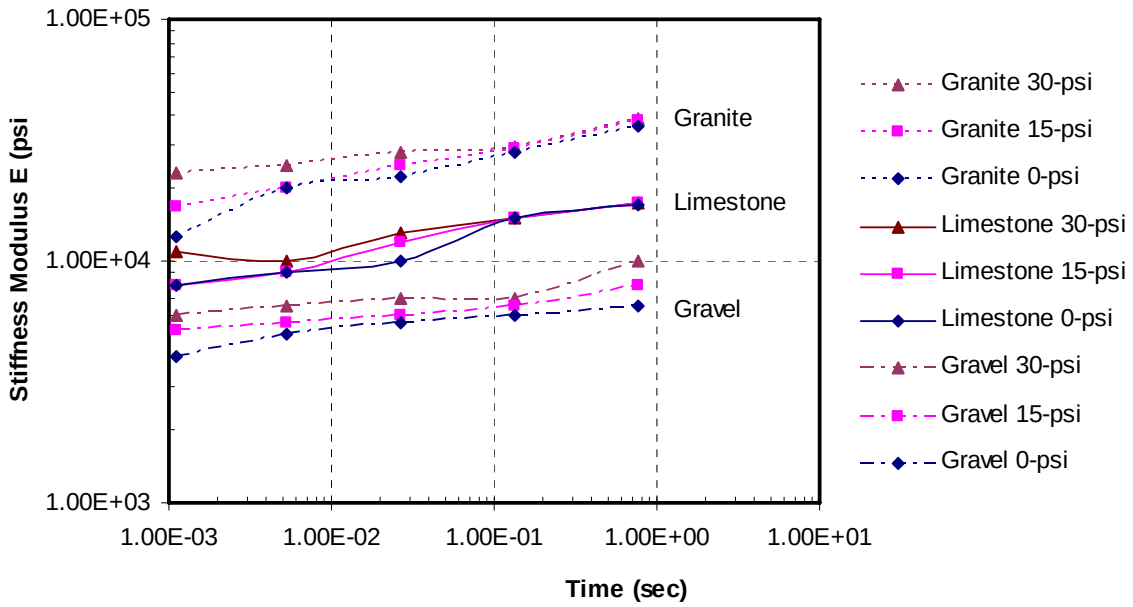

Figure 6.5. Stiffness Modulus Evolution as a Function of Time.

The moduli values agree with the nature of the aggregate characteristics, in which granite particles are stiffer than those of limestone and gravel. It is noticed also that, the moduli had a negligible dependency on the confinement pressure for all mixes. Therefore, it is concluded that the initial modulus is a function of only the loading rate. A power law function for the modulus as a function of time has been used by many researchers to find such a relation Daniel et al. (2002). The viscoelastic response is represented by Eq. (6-5):

$$\sigma(t) = \int_0^t \tilde{E}(t-\tau)\frac{d\varepsilon}{d\tau}d\tau \tag{6-5}$$

where $\tilde{E}(t-\tau)$ is the relaxation modulus as a function of time, τ is a time-dependent variable, and ε is the axial strain. For a strain rate-controlled strength test, Eq. (6-5) reduces to the following:

$$\sigma(t) = \dot{\varepsilon}(t)\int_0^t \tilde{E}(t-\tau)d\tau \tag{6-6}$$

Assuming a power law for the relaxation modulus and solving the convolution integral in the form:

$$L[h(t)] = L\left[\int_0^t P(\tau)Q(t-\tau)d\tau\right] = L[P(t)]L[Q(t)] \tag{6-7}$$

where L is the Laplace operator and solving Eq. (6-6), the stiffness modulus can be expressed as follows:

$$E = \frac{\sigma(t)}{\varepsilon(t)} = E_1 t^{-E_2} \tag{6-8}$$

where E_1 and E_2 are material parameters to be determined experimentally using the relationship between the stiffness modulus and time as presented in Fig. 6.5.

Following the linear zone in Fig. 6.4 is the stress level (flow stress) at which the material exceeds the visco-elastic limit and starts to initiate visco-plastic deformation. At the flow stress, the initial Drucker-Prager yield surface parameters α and κ_o are evaluated. The flow stress is determined for each combination of strain rate and confining pressure, and the initial yield surfaces are determined as shown in Fig. 6.6.

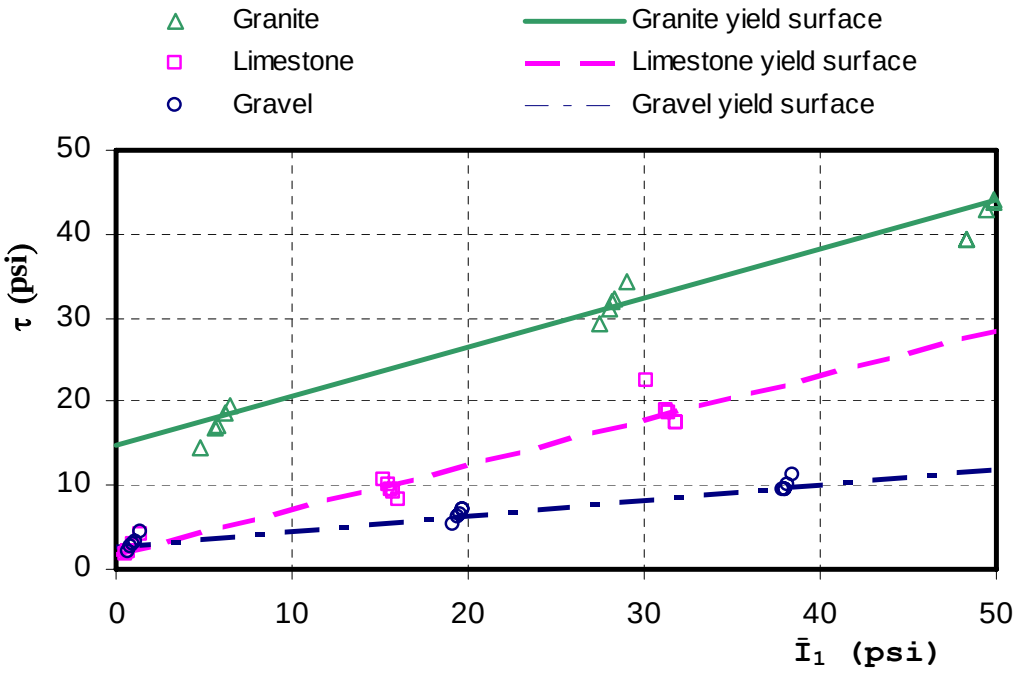

Figure 6.6. Initial Yield Surfaces for Different HMA Types in Compression Triaxial Testing.

The slope of the yield surface represents the frictional properties of the aggregates within the material microstructure. The intercept reflects the cohesive and adhesive properties of the binder within the microstructure. Fig. 6.6 indicates that granite and limestone mixes had the same slopes of yield surfaces indicating that they have similar aggregate friction potential. On the other hand, the intercept, which is the measure of initial hardening, was found higher in the granite mix, and

comparable values were found for the limestone and gravel mixes. It seems that the strength of the limestone mix is produced mainly from its aggregate frictional properties. The granite mix combines both aggregate frictional and binder cohesive and adhesive properties to develop its strength, which could possibly be the reason for its relatively high strength.

The second zone in stress-strain relationship is the work hardening phase, starting from the flow stress to the ultimate response where the parameters Γ and N and the hardening parameters κ_1 and κ_2 are determined simultaneously, as shown in Fig. 6.4. The last zone of the curve is the softening phase, where the damage parameters are evaluated.

Finally, another constraint is applied to the material response to find the dilation potential by using the ratio of axial and radial strain measurements. The plastic potential function, g, is assumed to have the same form as the yield function but with a slope of β^*, which influences the proportions of the volumetric and deviatoric strains. The parameter is determined by the visco-plastic strain rate ratio (VSRR) as shown in Eq. (6-9) and Eq. (6-10):

$$VSRR = \frac{-\dot{\varepsilon}_{33}^{vp}}{\dot{\varepsilon}_{11}^{vp}} = \frac{-\left(\frac{\partial g}{\partial \sigma_{33}}\right)}{\left(\frac{\partial g}{\partial \sigma_{11}}\right)} = \frac{(1+\Delta)}{(1-\Delta)} \cdot \frac{\left(\frac{1}{2d} + \frac{\beta}{3}\right)}{\left(\frac{1}{d} - \frac{\beta}{3}\right)} \tag{6-9}$$

$$\beta^* = 3 \cdot \frac{\beta + \Delta\left(\frac{2}{d} - \frac{1}{3}\beta\right)}{\frac{3}{d} - \Delta\left(\frac{1}{d} - \frac{4}{3}\beta\right)} \tag{6-10}$$

The derivation for Eq. (6-10) is provided in Chapter IV. Experimental measurements indicate that the evolution of β with respect to the effective visco-plastic strain was minimal, especially at high strain levels, and thus for simplicity it could be assumed to be constant. It is indicated that, the dilation parameter was the lowest for the gravel mix and highest for the limestone.

Table 6.2 summarizes the material parameters for all mixes. The limestone mix had the highest vector magnitude among the three mixes, while granite and gravel had comparable vector magnitudes. In terms of the yield function parameters, the gravel mix had the highest N values indicating a higher potential to develop permanent deformation. On the other hand, the limestone and granite mixes had comparable values of N, which were smaller than that of the gravel. Fig. 6.7 shows the evolution of hardening parameters with respect to the effective visco-plastic strain. The figure indicated that granite has the highest work-hardening potential where limestone has the lowest.

Table 6.2. Summary of Model Parameters.

Parameter	Granite	Gravel	Limestone	Notes
Δ	2.860E-01	2.610E-01	4.360E-01	Measured by IAT
d	7.780E-01			
E_1	1.833E+04	7.583E+03	3.798E+04	Linear material properties
E_2	1.236E-01	6.010E-02	1.158E-01	
υ	1.800E-01	3.610E-01	2.180E-01	
α	5.862E-01	2.462E-01	5.345E-01	Static parameters
κ_o	1.468E+01	3.025E+00	1.739E+00	
Γ	5.000E-07	1.000E-07	9.000E-07	Perzyna's parameters
N	2.160E+00	2.993E+00	2.200E+00	
β	3.332E-01	3.000E-01	3.570E-01	Dilation parameter

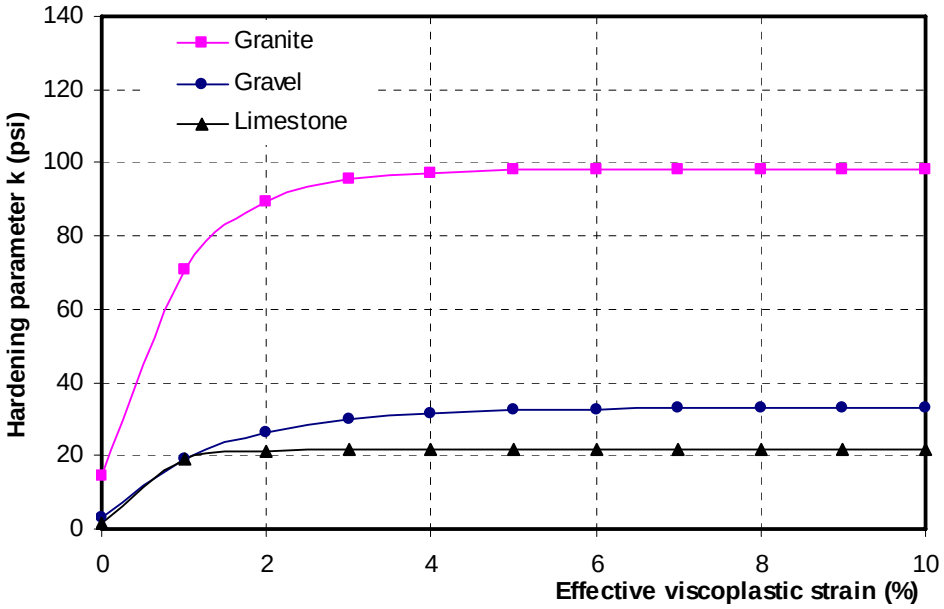

Figure 6.7. Evolution of κ with Respect to Effective Visco-plastic Strain.

FINITE ELEMENT SIMULATIONS OF LABORATORY EXPERIMENTS

As discussed in Chapter V, ABAQUS was used to develop a quadrilateral two-dimensional four-node axisymmetric FE model. This model as presented in Fig. 6.8 was used to simulate a laboratory specimen subjected to uniform vertical strain rates and confining pressure similar to those used in the experiments. The material properties were obtained from the experiments, as discussed in the previous section. The boundary conditions were applied such that there was no vertical

displacement at the bottom of the model and no lateral displacement at the left side of the model to represent symmetry. The model was for a specimen with 4 in diameter and 6.2 in height. The analysis was conducted in perturbation mode with a time increment. Load was applied in two steps. Confining pressure was applied in the first step, and constant strain rate in the vertical direction was applied in the second step. Stress and strain values were recorded at each time step and compared with the experimental measurements.

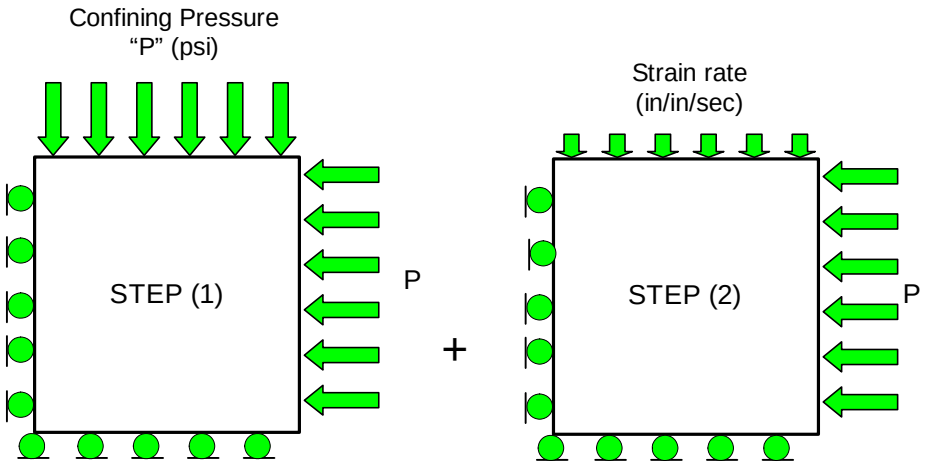

Figure 6.8. FE Geometric Model and Loading Step Procedure .

Fig. 6.9 show the triaxial compressive and extension strength test data for the three mixes. Each curve represents an average of two replicates. Fig. 6.9 show the effect of the strain rate and confining pressure. Higher strengths were associated with higher strain rates and/or confining pressures. It can be seen that gravel mix is the weakest and granite mix is the strongest among the three tested mixes.

The model has showed good simulation to the experiments, the model parameters are able to distinguish between the three mixes in terms of their response to different strain rates and confining pressures. It is interesting to note that although limestone and granite mixes had relatively close material parameters, the significant difference in the anisotropy highly governed the response of each mix.

For triaxial extension strength test, the simulation was conducted using damage parameters different than those used in the compression test, while other parameters were kept the same. The extension results were much less influenced by confining pressure and strain rate compared with the compression test results. As expected, the extension tests experienced softening behavior much earlier than the compression tests. As discussed earlier, extension loading promotes opening of cracks and softening behavior, while damage in compression tests is associated with sliding particles that occurs after some hardening behavior.
FE simulation results showed that tensile strength is much lower than compressive strength for all confining pressures and strain rates. However, the FE results overestimated the tensile strength

compared with the experimental measurements. This overestimation is not expected to have a significant impact on the ability of the model to simulate permanent deformation under traffic loading, since the tensile strength results are still considered small values.

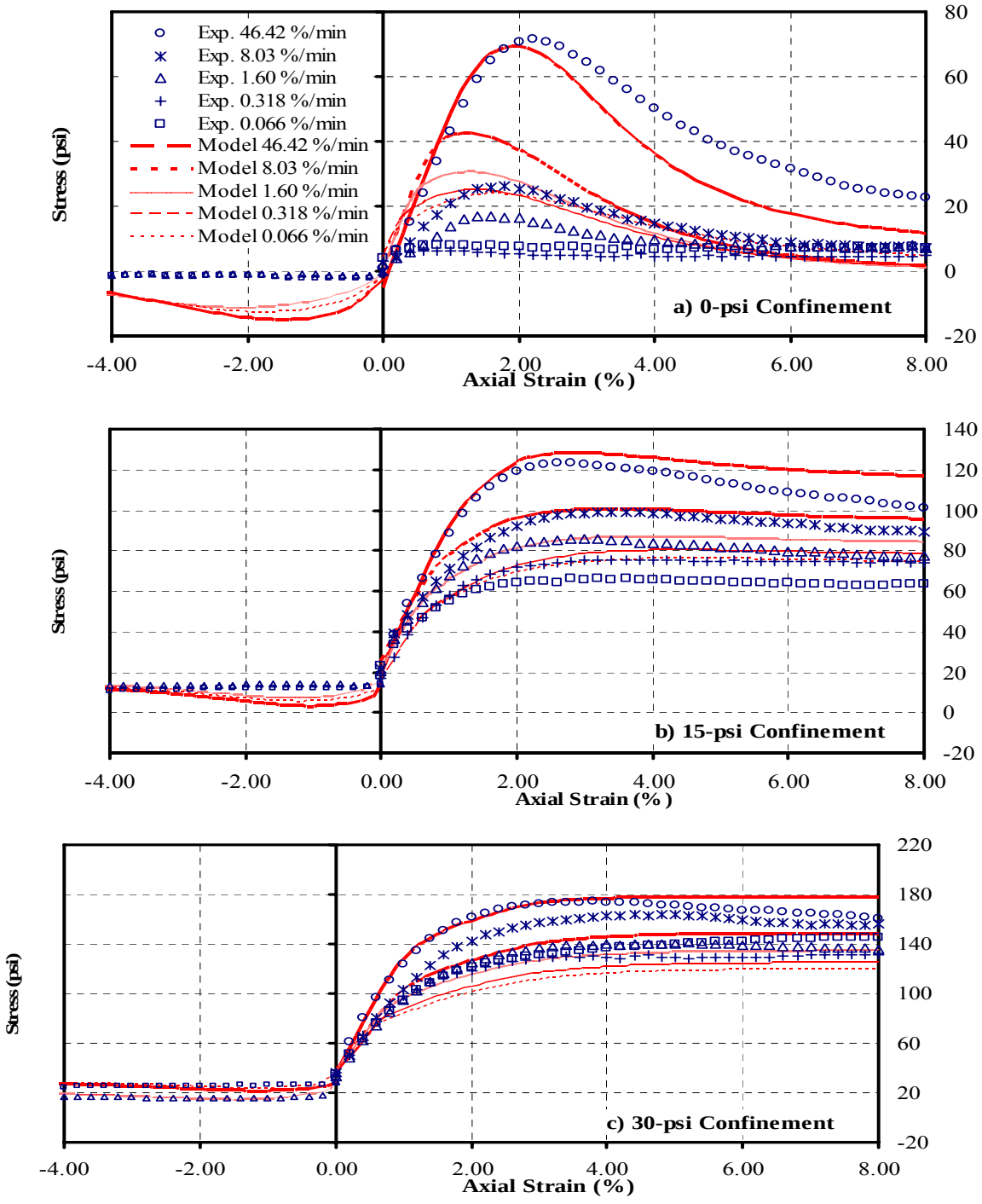

a) Gravel Mixes

Figure 6.9. Matching Compression and Extension Strength Tests.

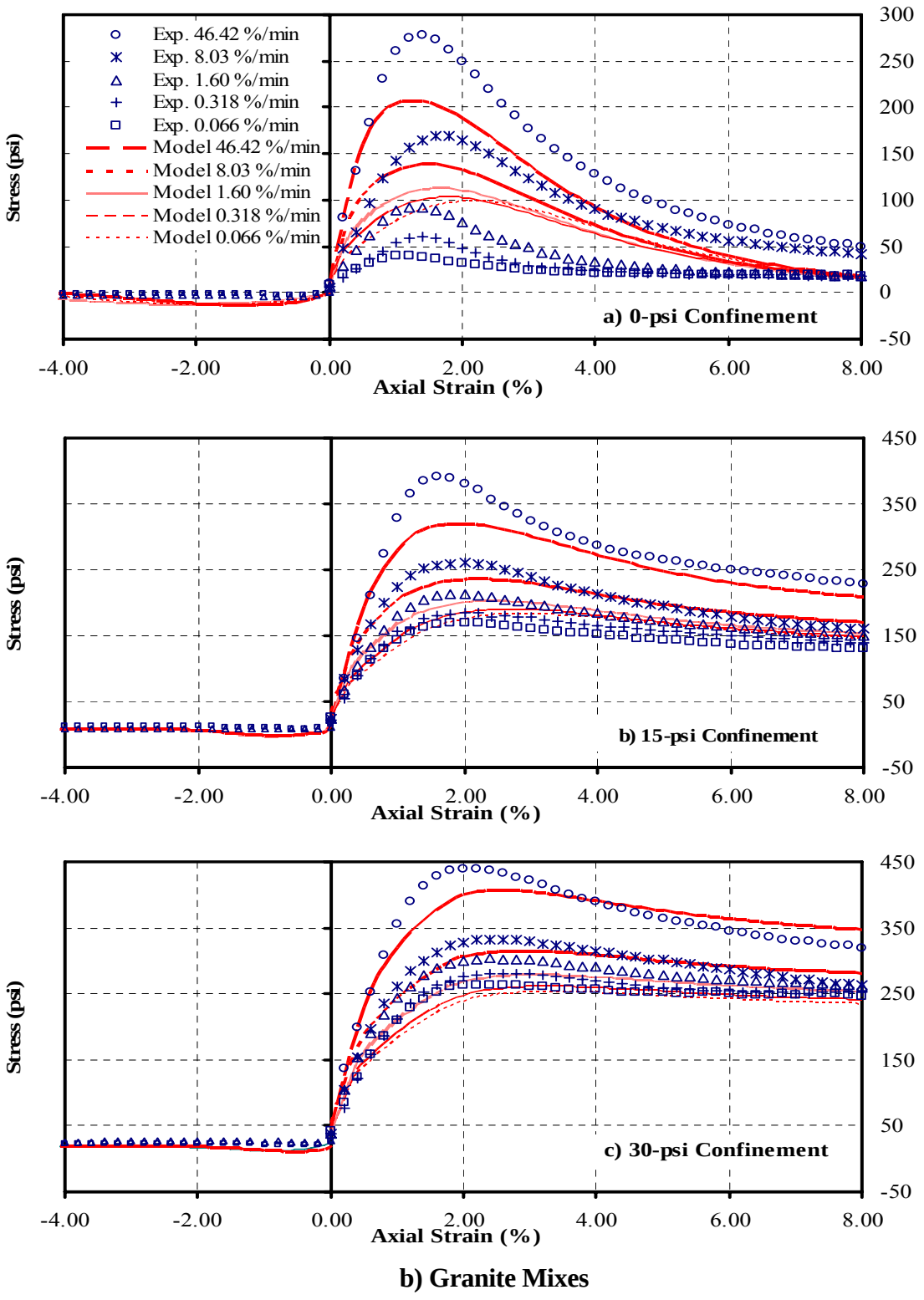

b) Granite Mixes

Figure 6.9. Continued

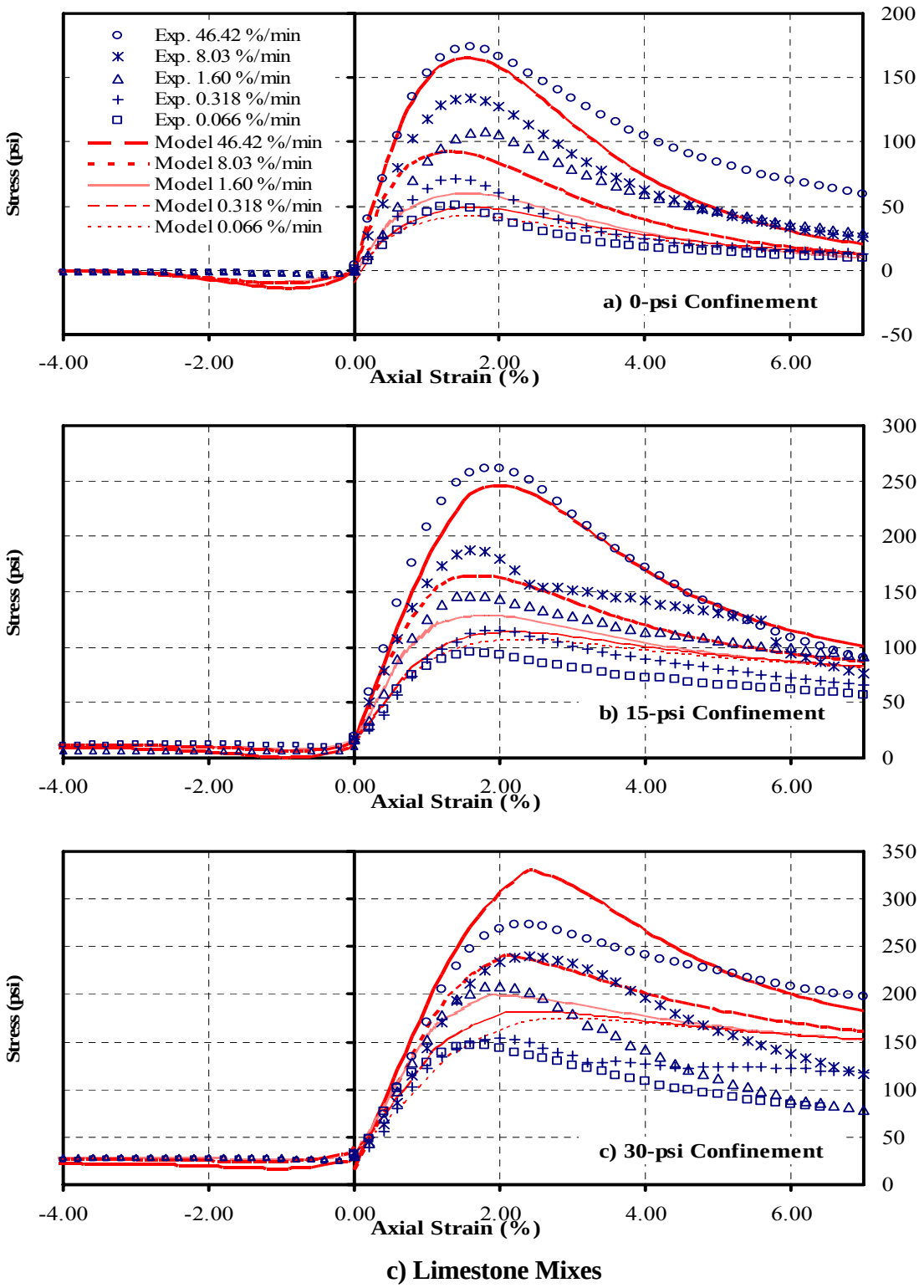

c) Limestone Mixes

Figure 6.9. Continued

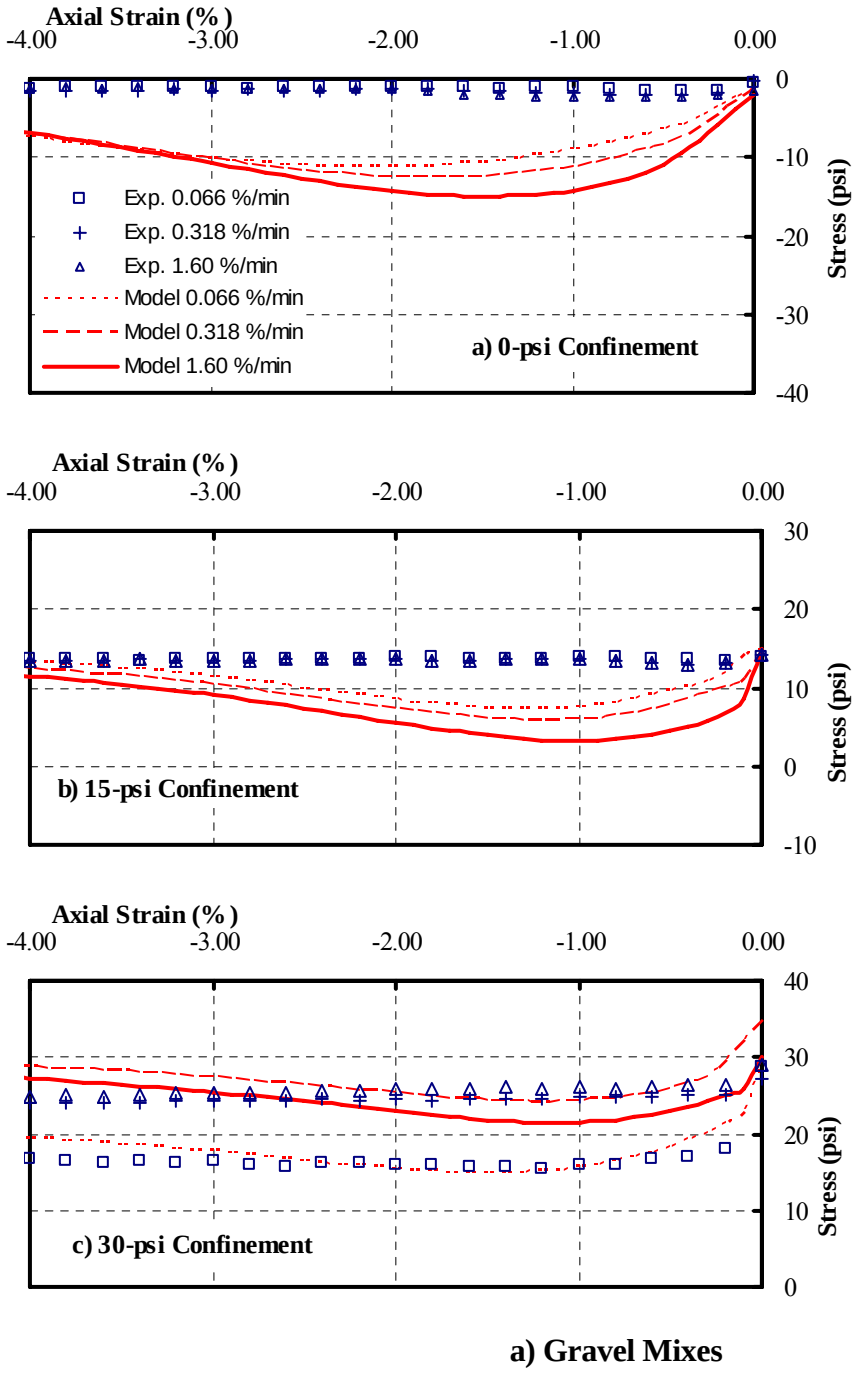

Figure 6.10. Matching Extension Strength Test (Using Different Damage Parameters)

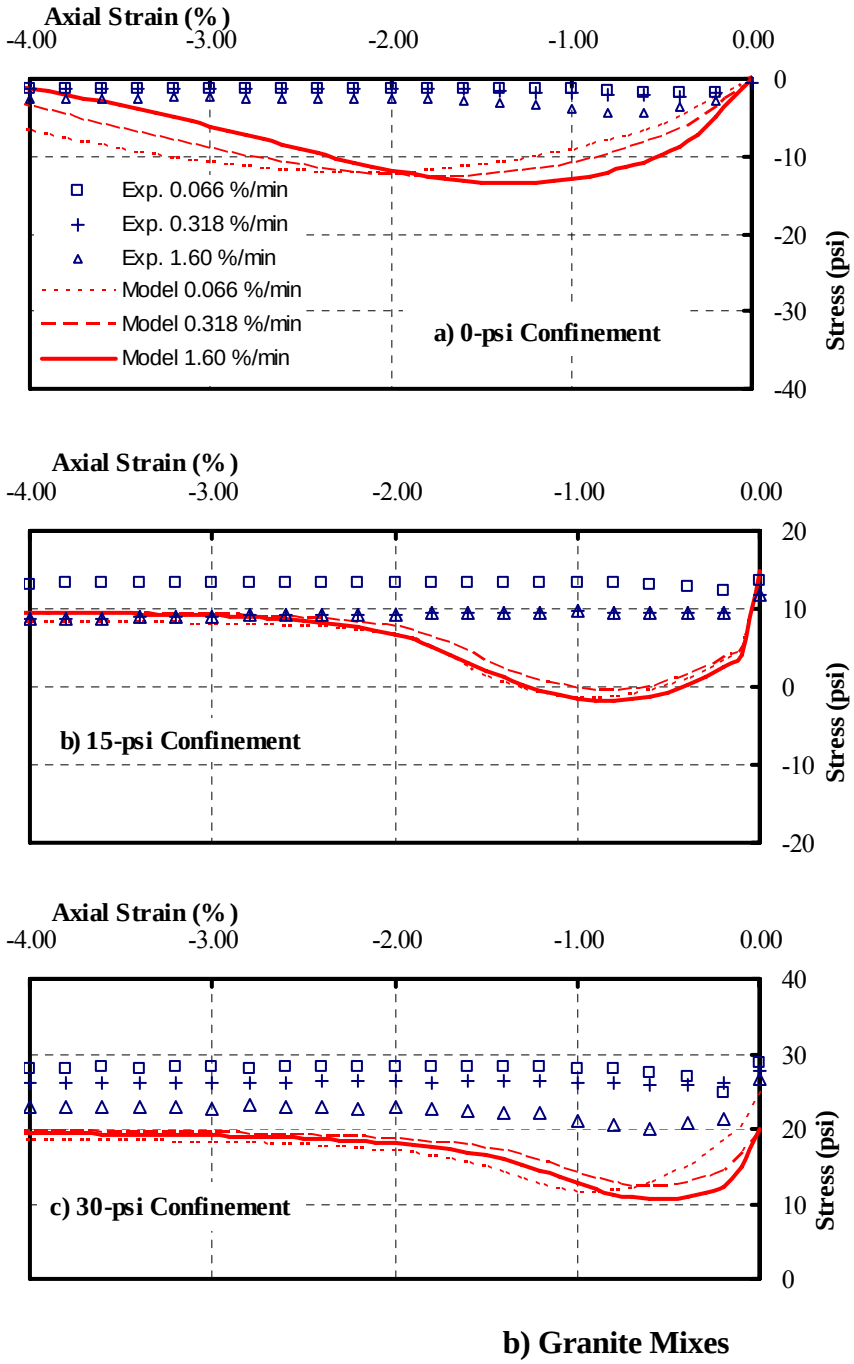

b) Granite Mixes

Figure 6.10. Continued

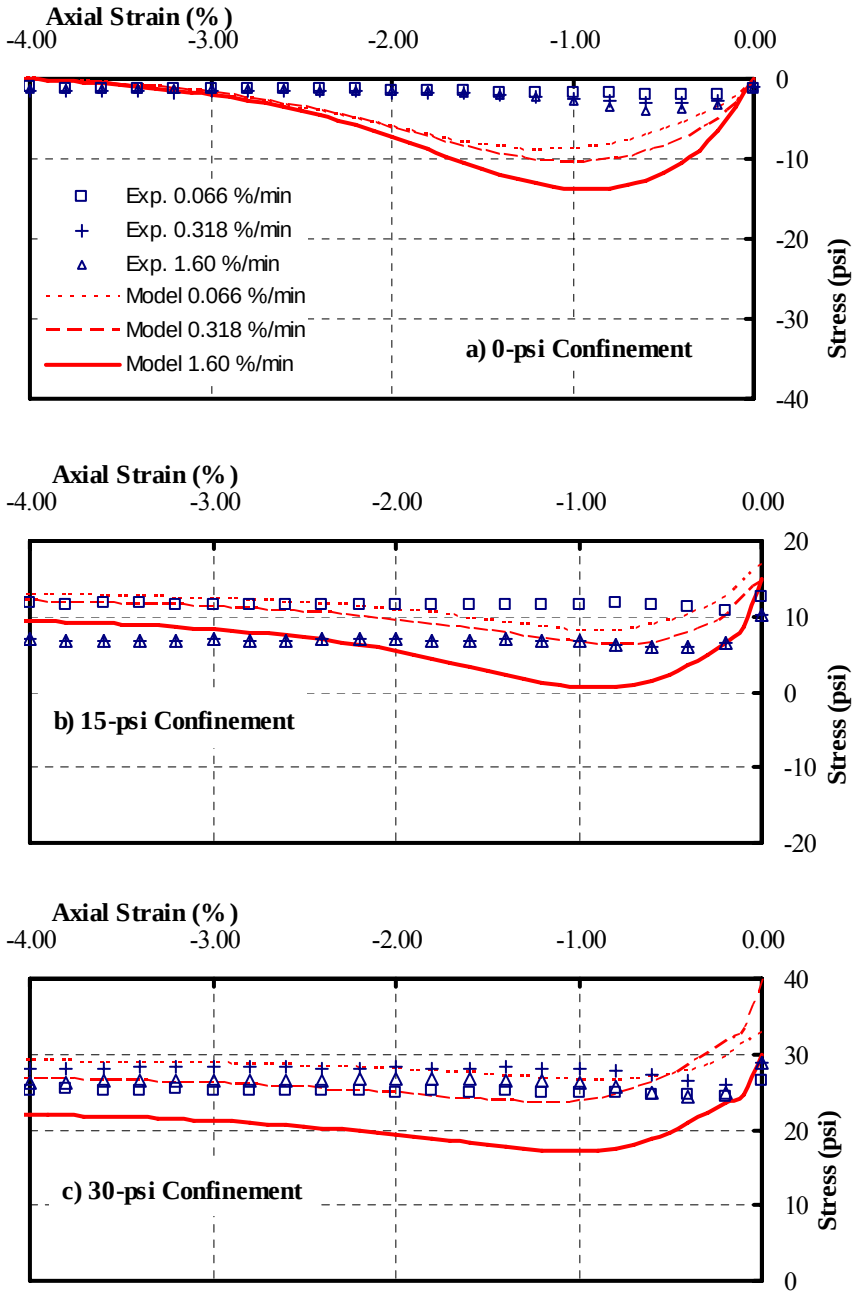

b) Limestone Mixes

Figure 6.10. Continued

As shown in Fig. 6.9, it is noticed that the material showed independency of the confining pressure under tensile stresses. Therefore, another approach is presented to simulate extension data by using the same evolution law for damage parameter in Eq. (6-3) with no confining pressure effect. Results indicate, as shown in Fig. 6.10 that much improved simulation with the experiment is obtained.

FE simulations of lateral deformation are compared with experimental measurements as shown in Fig. 6.11. Radial deformation was measured for all mixes at strain rates of 1.60%/min and 46.4%/min and at confining pressures of 0 and 30 psi. It is evident that the FE simulations were able to capture the lateral deformations, especially at lower strain levels. As the deformation increases, the simulation model tends to underestimate the experimental measurements. The region where the model deviates from the experiment is where the material starts to soften, passing the ultimate stress.

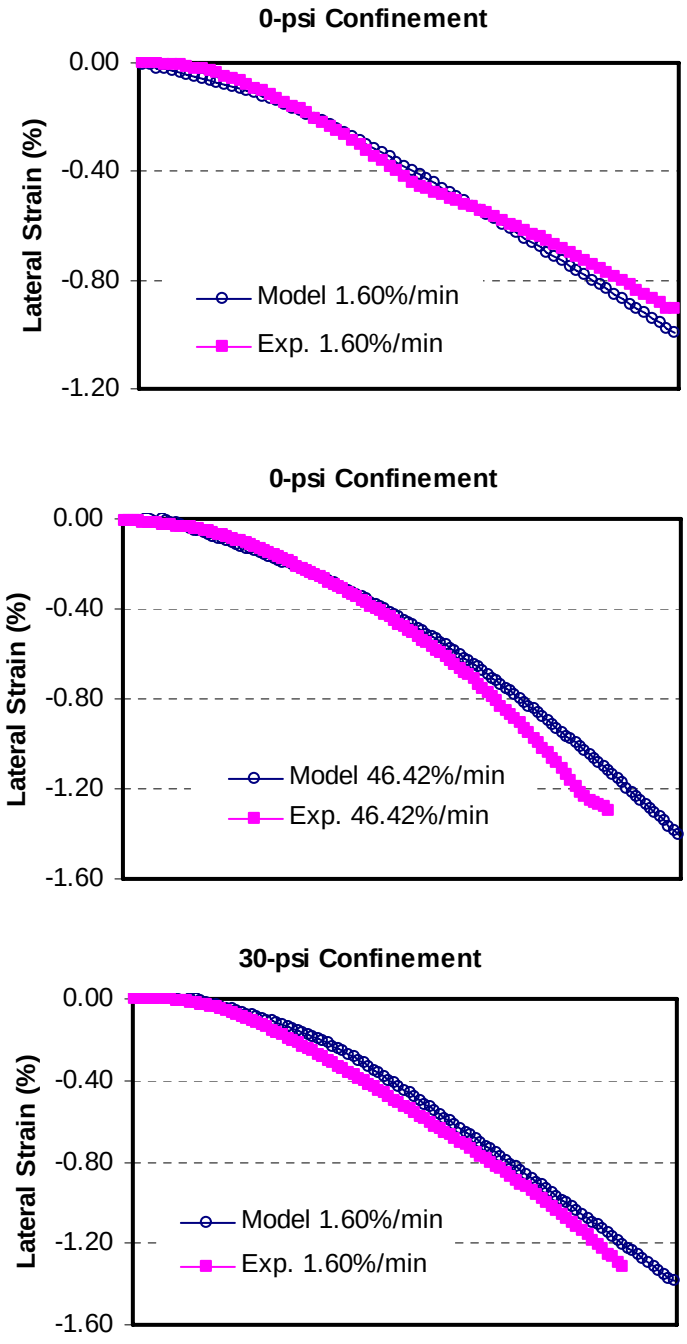

a) Gravel Mixes

Figure 6.11. Lateral Strain Simulation.

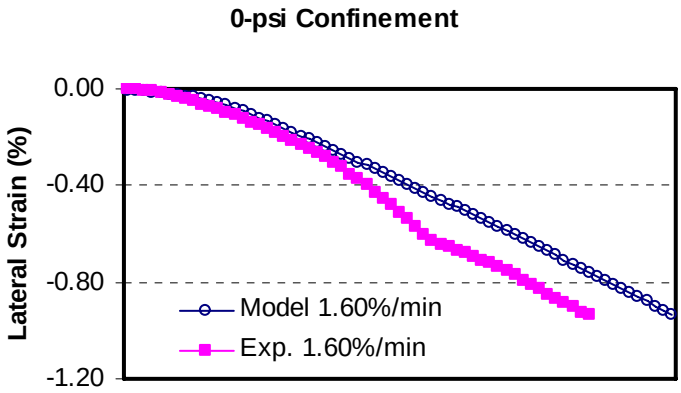

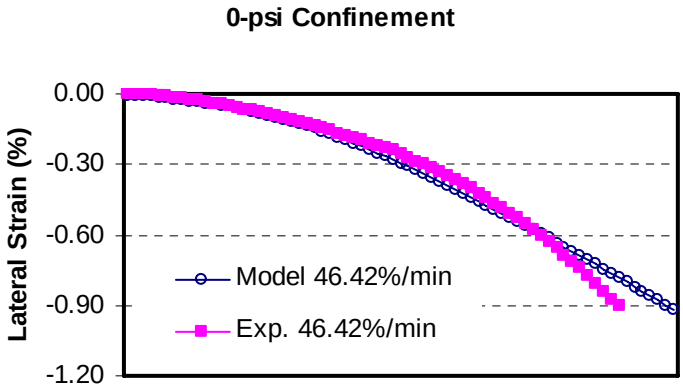

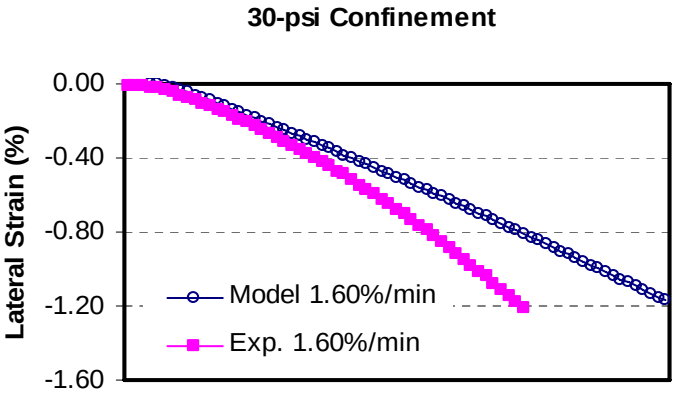

b) Granite Mixes

Figure 6.11. Continued

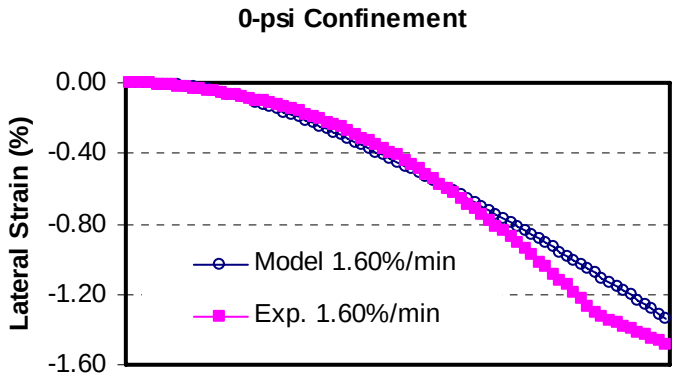

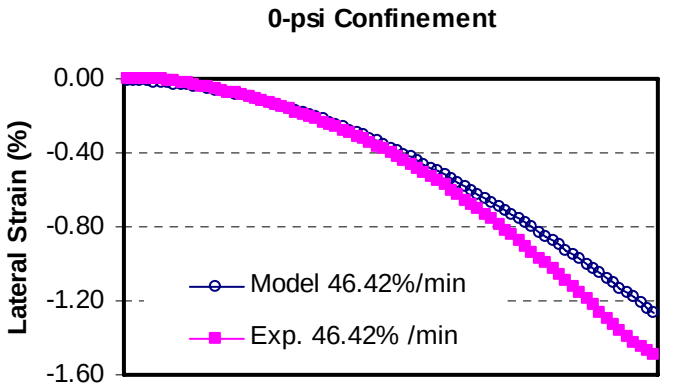

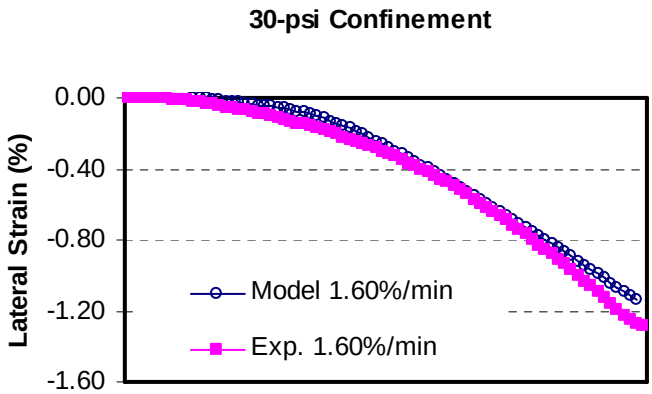

c) Limestone Mixes

Figure 6.11. Continued

AN EXAMPLE OF FINITE ELEMENT SIMULATION OF ASPHALT PAVEMENTS

A one-lane HMA layer with 15 in thickness and 80 in width, is simulated with axisymmetric elements as shown in Fig. 6.12. a static distributed pressure of 100 psi is applied at the top layer to simulate tire pressure. Fixed boundary condition in the horizontal direction only is maintained. Assuming that permanent deformation to occur in the HMA layer only, the subbase layer is considered very stiff and hence, the bottom layer of HMA is not allowed to deform in the vertical direction. The analysis is conducted by applying pressure in the initial time step, and permanent deformation is recorded as a function of time. The analysis is conducted to emphasize the influence of anisotropy on permanent deformation. HMA is defined with two different cases, $\Delta = 0$, for isotropic, and $\Delta = 30\%$, for anisotropic case, the remaining model parameters represent the limestone mix described earlier in this chapter.

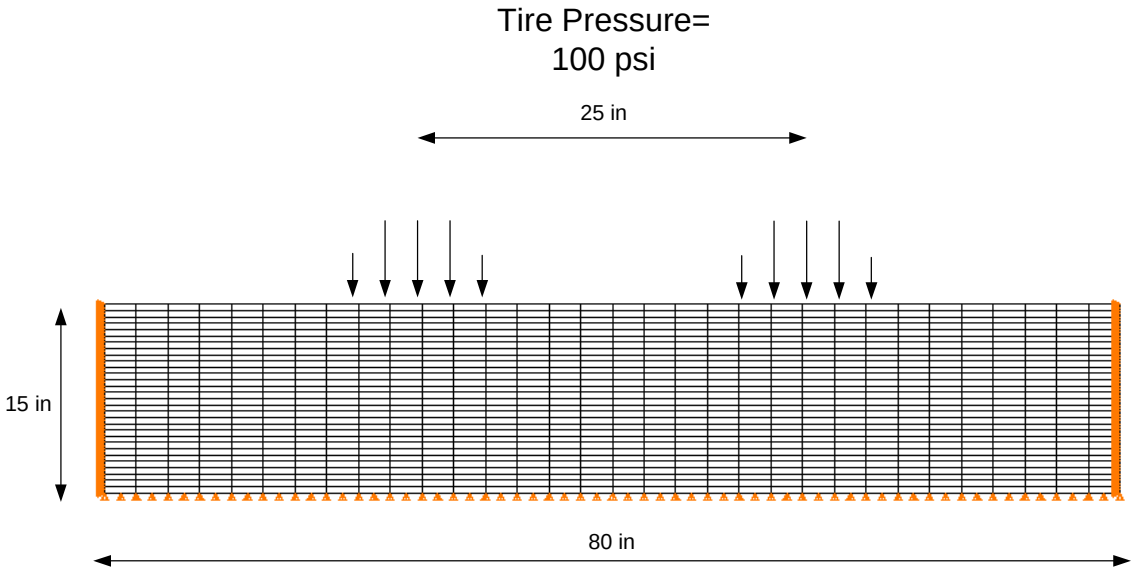

Figure 6.12. FE Geometric Model for Pavement Lane

Fig. 6.13 indicates that anisotropy increased the shear stress by about 30 % under the wheel loads. Although the anisotropic HMA layer developed more shear stress, permanent deformation was found to be less in magnitude when anisotropy is considered as shown in Fig. 6.14. The material also exhibited more dilation between the tires as a result of anisotropy. This is consistent with the findings in Eq. (4-40) that the angle of dilation increases with anisotropy.

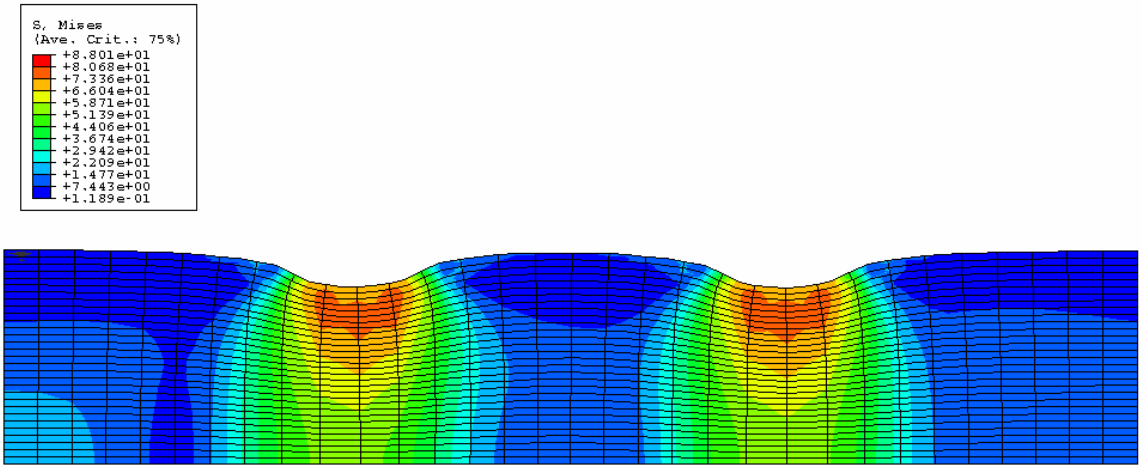

a) Isotropic layer (Δ =0)

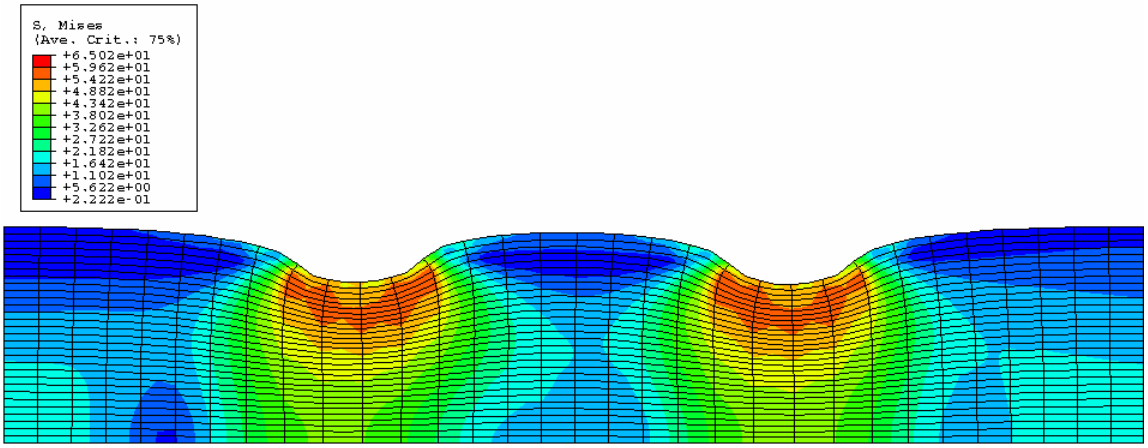

b) Anisotropic layer (Δ =30%)

Figure 6.13. Shear Stress Distribution in HMA Layer due to Tire Pressure.

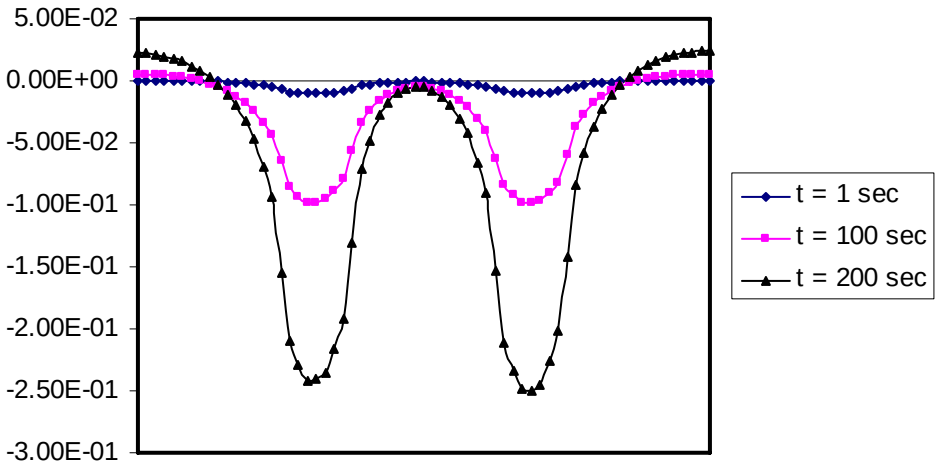

a) Isotropic layer (Δ =0)

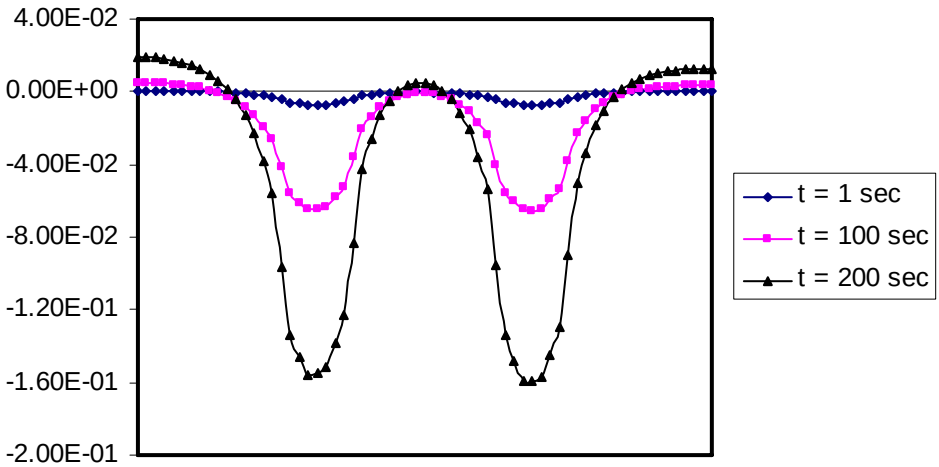

b) Anisotropic layer (Δ =30%)

Figure 6.14. Permanent Deformation Profile in HMA Layer due to Tire Pressure.

SUMMARY

A procedure for the determination of the evolutions of model parameters was established using triaxial compression and extension strength tests. Model parameters were calculated using a systematic approach by dividing the stress-strain relationship. FE implementation of the model showed that model parameters were able to distinguish between three HMA specimens with different aggregate type and characteristics. Experimental results and FE simulations showed that gravel mix had the highest potential for permanent deformation while granite had the lowest potential. Granite mix also had the highest κ and α values reflecting the adhesion between binder and aggregates, and aggregate friction, respectively. This finding is resulting from the coarse

texture of granite as indicated by Masad et al. (2003). The influence of aggregate angularity was manifested in dilation where the experimental results and model parameters showed limestone to have the highest dilation followed by granite.

The FE simulations had very good agreement with experimental measurements under compression loading at almost all strain rates and confining pressures. The simulation results also showed that tensile strength of all mixes was much lower than compressive strength. The damage parameters used in simulating the extension tests were different than those used in the compression tests. This is justified by the fact that damage is promoted by tensile stresses much earlier than under compressive stresses. Tensile stresses cause an increase in cracks and void sizes, leading to softening, while damage in compression occurs due to particle sliding after some hardening behavior.

Field conditions for a pavement surface subjected to wheel loads were simulated using FE. Results indicated that anisotropy increases shear stresses underneath wheel loads, decreases permanent deformation in the axial direction, and increase the dilation in the lateral direction. Although more shear stress is expressed due to anisotropy, HMA exhibited more stiffness in the axial direction and hence, less permanent deformation is achieved.

CHAPTER VII
SUMMARY AND CONCLUSIONS

SUMMARY AND MAIN CONCLUSIONS

This study focused on the development of continuum models for hot mix asphalt (HMA) that account for the influence of microstructure distribution into macroscopic behavior. The first advancement in this study was the development of an elasticity gradient model that employs the strain gradient concept and effective material properties. The use of strain gradient introduces a length scale parameter to the elasticity constitutive model which allows the model to capture the influence of particle size distribution on HMA response. Analytical procedures were developed in this study to obtain microstructure characteristic length scales to be used in the constitutive relationship. These analytical procedures are the moving window technique and the autocorrelation function.

The elasticity gradient model was implemented in finite element (FE) analysis and used to analyze microstructure response and predict the macroscopic properties for HMA with different aggregate characteristics and structures. In FE analysis, each point was assigned effective local material properties, which capture the influence of the material in the vicinity of a point on the mechanical response of that point. FE results showed that the developed model was successful in overcoming some limitations of using the individual properties of the constituents in FE analysis of HMA microstructure. For example the model reduced mesh size dependency, reduced sensitivity of the response to small changes in the microstructure caused by image capturing and processing, and reduced the numerical instability caused by several orders of magnitude indifference in stiffness between adjacent elements of the microstructure. In addition, the model captured the influence of HMA length scales on microscopic and macroscopic responses. The results showed that the determined HMA effective properties using the model were more consistent with the experimental measurements.

The second advancement in this study was the development of an elasto-visco-plastic continuum model to predict HMA response and performance under wheel loadings. The model included microstructure parameters that captured the directional distribution of aggregates and density of cracks. In addition, the model was capable to account for the factors affecting the mechanisms of permanent deformation such as shear stress, aggregate structure friction and dilation, confining pressure, strain rate, and stress path direction.

The elasto-visco-plastic model was implemented in FE analysis. The implementation of the model was in the form of a fully implicit algorithm using the backward Euler scheme in time-step control. The Newton-Raphson iterative scheme was used to define available initial solutions. The numerical scheme is based on the return mapping algorithm, which leads to elastic predictor-plastic corrector steps. The algorithm included a consistency condition analogous to the time-independent plasticity theory to evaluate the visco-plastic multiplier. Quadratic convergence was achieved in the analysis by using algorithmic elasto-visco-plastic tangent moduli in the algorithm.

A parametric analysis was conducted to investigate the effect of key parameters in the model on the material response. The results showed clearly that the model is sensitive to particle friction (α), material hardening (κ), dilation (β), anisotropy (Δ), void nucleation and growth (ξ), and stress path direction (d). d affects the geometry of the yield surface in the deviatoric plane. $d = 0.778$ is the minimum value to achieve the convexity of the yield surface. An increase in the anisotropy level causes an increase in the material strength in the axial direction normal to the preferred orientation of particles. The yield strength in the direction parallel to the orientation of particles decreases slightly with an increase in anisotropy level. The study also showed that loading rate and confinement affected the model response. Increasing loading rate and confinement caused an increase in the ultimate stress.

Triaxial compression and extension strength tests on granite, gravel, and limestone mixes were used in this study to determine model parameters and evolution formulation for each mix type. Strength tests were conducted at different loading rates and confining pressures. Model parameters were determined using a systematic approach by using the stress-strain relationship. Experimental results showed that granite had the lowest potential for permanent deformation, the highest work hardening capability. Gravel had the highest potential for permanent deformation, and limestone had the highest dilation.

FE analysis was conducted to simulate experimental measurements under compression and extension loading with different strain rates and confining pressures. The FE results indicated that the elasto-visco-plastic model parameters were able to distinguish between HMA mixtures with different aggregate characteristics. The simulation results showed that tensile strength of the mixes is much lower than compressive strength. The damage parameters used in simulating the extension tests are different than those used in the compression tests, because softening in extension test occurs earlier and at a faster rate than in compression.

FE analysis was also utilized to simulate permanent deformation in a pavement section. Anisotropy is found to influence shear stress distribution, permanent deformation underneath the tires, and dilation in the lateral direction and beneath the tires.

IMPLEMENTATIONS AND RECOMMENDATIONS

The advantage of continuum models is their computational simplicity, and once the material properties are known, simulations of material deformation under static or dynamic loading can be implemented in FE analysis to predict HMA performance. Moreover, the developed model provides a powerful tool to understand the role and contribution of fundamental properties of the constituent materials in composite structure into the overall response. The model can also be used to directly examine the influence of changes in mix design and material properties on microstructure distribution and performance.

The developed continuum model contains the elements needed to account for all the characteristics that influence permanent deformation including loading rate, confining pressure, dilation under shear loading, and stress path direction. The model also accounts for microstructure distribution in

terms of damage and anisotropy due to the aggregate preferred orientation. Therefore, the model can be used to optimize mix design based on performance predictions of the model.

The use of axisymmetric presentation of the continuum model in FE analysis is an acceptable approach to simulate field conditions. However, it is recommended that the model be improved to three-dimensional representation to account for more realistic boundary and loading conditions. This representation will improve simulation of field conditions and hence will lead to improved predictions of performance.

The model needs to further development to account for the effects of temperature and aging on permanent deformation. This can be accomplished by developing relationships between the evolution of model parameters and temperature.

In this study, damage is assumed to have an isotropic distribution. However, damage can be easily expressed using directional distribution functions to account for the anisotropic distribution of damage. Recent advances in imaging techniques and nondestructive evaluation make it possible to characterize the directional distribution of damage.

The model needs to be verified by simulating boundary conditions different than those used to determine the model parameters. These boundary conditions could include static creep and repeated loading with different rest periods. Finally, the model needs to be implemented for predicting HMA performance under full-scale accelerated loading and actual field conditions.

REFERENCES

ABAQUS (2004). *User's and Theory Manuals*, versions 6.4, Hibbit, Karlsson & Sorensen Inc., Pawtucket, RI.

Abbas, A., Papagiannakis, T., and Masad, E. (2001). "Relating the microstructure of asphalt mixes to their constitutive behavior." *Proc., 2001 ASCE-ASME-SES Joint Applied Mechanics and Materials Summer Conference*, University of California, San Diego, LaJolla, CA.

Abdulshafi, A., and Majidzadeh, K. (1985). "Combo viscoelastic-plastic modeling and rutting of aphaltic mixtures." *Transportation Research Record* 968, Transportation Research Board, Washington, D.C., 19-31.

Aifantis, E. C. (1984). "On the microstructural origin of certain inelastic models." *Journal of Engineering Materials and Technology*, ASME, 106(4), 326-330.

Aifantis, E. C. (1987). "The physics of plastic deformation." *International Journal of Plasticity*, 3, 211-247.

Alfano, G., De Angelis, F., and Rosati, L. (2001). "General solution procedures in elasto/ viscoplasticity." *Computer Methods in Applied Mechanics and Engineering*, 190, 5123-5147.

Auricchio, F., and Taylor, R.L. (1995). "Two material models for cyclic plasticity: nonlinear kinematic hardening and generalized plasticity." *International Journal of Plasticity*, 11(1), 65-98.

Bahia, H., Zhai, H., Bonnetti, K., and Kose, S. (1999). "Nonlinear viscoelastic and fatigue properties of asphalt binders." *Journal of the Association of Asphalt Paving Technologists, 68,* 1-34.

Baxter, S. C., and Graham, L. L. (2000). "Characterization of random composites using moving-window technique." *Journal of Engineering Mechanics*, ASCE, 126(4), 389-397.

Berryman, J., and Blair, S. (1986). "Use of digital image analysis to estimate fluid permeability of porous materials: application of two-point correlation functions." *Journal of applied Physics*, 60(6), 1930-1938.

Bonnier, P. G., and Troost, E. (1991). "Numerical model for elastic-viscoelastic-viscoplastic behaviour of bituminous concrete." *Proc., International Conference on Computer Methods and Advances in Geomechanics*, 575-580.

Brown, S., and Bell, C. (1977). "The prediction of permanent deformation in asphalt pavements." *Journal of the Association of Asphalt Paving Technologists*, 48, 438-476.

Brown, S. F., and Cooper, K. E., (1980). "A fundamental study of the stress-strain characteristics of a bituminous material." *Journal of the Association of Asphalt Paving Technologists*, 49, 476.

Buttlar, W. G., and You, Z. (2001). "Discrete element modeling of asphalt concrete: microfabric approach." *Transportation Research Record* 1757, Transportation Research Board, Washington, D.C., 111-118.

Buttlar, W. G., Bozkurt, D., Al-Khateeb, G., and Waldhoff, A. S. (1999). "Understanding asphalt mastic behavior through micromechanics." *Transportation Research Record* 1681, Transportation Research Board, Washington, D.C., 157–169.

Button, J., Perdomo, D., and Lytton, R. (1990). "Influence of aggregate on rutting in asphalt concrete pavements." *Transportation Research Record* 1259, Transportation Research Board, Washington, D.C., 19 - 31.

Chang, K. G., and Meegoda, J. (1997). "Micromechanical simulation of hot mix asphalt." *Journal of Engineering Mechanics*, ASCE, 123(5), 495-503.

Chehab, G. R., Kim, Y. R., Schapery, R. A., Witczak, M. W., and Bonaquist, R. (2003). "Characterization of asphalt concrete in uniaxial tension using a viscoelastoplastic model." *Journal of the Association of Asphalt Paving Technologists*, 72, 315-355.

Chen, W. F., and Han, D. J. (1988). *Plasticity for structural engineers*, Springer-Verlag, NY.

Christensen, R. M. (1979). *Mechanics of composite materials*, 2nd ed., J. Wiley, NY.

Christensen, R. M. (1990). "Critical evaluation for a class of micro-mechanics models." *Journal of the Mechanics and Physics of Solids*, 38(3), 379-404.

Collop, C., Scarpas, A. T., Kasbergen, C., and de Bondt, A. (2003). "Development and finite element implementation of a stress dependent elasto-visco-plastic constitutive model with damage for asphalt." *Transportation Research Record* 1832, Transportation Research Board, Washington, D.C., 96-104.

Cosserat, E., and Cosserat, F. (1909). *Theorie des corps deformables*, A. Hermann, Paris.

Dafalias, Y. F. (1990). "The plastic spin in viscoplasticity." *International Journal of Solids and Structures*, 26(2), 149.

Daniel, J. S., Kim, Y. R., Brown, S., Rowe, G., Chehab, G., and Reinke, G. (2002). "Development of a simplified fatigue test and analysis procedure using a viscoelastic, continuum damage model." *Journal of the Association of Asphalt Paving Technologists*, 71, 619-650.

Debye, P., Anderson, H. R., and Brumberger, H. (1957). "Scattering by an inhomogeneous solid. II. The correlation function and its application." *Journal of applied Physics*, 28, 679–683.

Desai S. (1998). "Review and evaluation of constitutive models for pavement materials." *Research Report submitted to SUPERPAVE*, Tucson, AZ.

Desai, C. S., and Zhang, D. (1987). "Viscoplastic model for geologic materials with generalized flow rule." *International Journal for Numerical and Analytical Methods in Geomechanics*, 11, 603-620.

Desai, C. S., Somasundaram, S., and Frantziskonis, G. (1986). "A hierarchical approach for constitutive modeling of geologic materials." *International Journal of Numerical and Analytical Methods in Geomechanics*, 10(3), 225-257.

Deshpande, V. S. (1995). "Deformation behaviour of idealized bituminous mixes." MSc thesis, University of Cambridge, Cambridge, U.K.

Deshpande, V. S., and Cebon, D. (1999). "Steady-state constitutive relationship for idealized asphalt mixes." *Mechanics of Materials*, 31, 271-287.

Dessouky, S., Masad, E., and Bayomy, F. (2003). "Evaluation of asphalt mix stability using compaction properties and aggregate structure analysis," *International Journal of Pavement Engineering*, 4(2), 87-103.

Dessouky, S., Masad, E., and Bayomy, F. (2004). "Prediction of hot mix asphalt stability using the superpave gyratory compactor." *Journal of Materials in Civil Engineering*, ASCE, 16(6), 578 – 587.

Drucker, D. C., and Prager, W. (1952). "Soil mechanics and plastic analysis or limited design." *Quarterly Applied Mathematics*, 10(2), 157-165.

Eisenmann, J., and Hilmer, A. (1987). "Influence of wheel load and inflation pressure on the rutting effect at asphalt pavement – Experiments and theoretical investigations." *Proc., Sixth International Conference on the Structural Design of Asphalt Pavements*, I, 392-403.

Erkens, S., Liu, X. and Scarpas, A. (2002). "3D finite element model for asphalt concrete response simulation." *The International Journal of Geomechanics,* 2(3), 305-330.

Gibson, N. H., Schwartz, C. W., Schapery, R. A., and Witczak, M. W. (2004). "Confining pressure effects on viscoplasticity and damage in asphalt concrete." *16th ASCE Engineering Mechanics Conference,* Seattle, WA.

Graham, L. L., and Baxter, S. C. (2001). "Simulation of local material properties based on moving-window GMC." *Probabilistic Engineering Mechanics*, 16(4), 295-305.

Green, A. E., and Rivlin, R. S. (1964). "Simple force and stress multipoles." *Archive for Rational Mechanics and Analysis*, 16, 325-3534.

Heeres, O. M. (2001). "Modern strategies for the numerical modeling of the cyclic and transient behavior of soils." PhD dissertation, Delft University, The Netherlands.

Hertzberg, R. W. (1996). *Deformation and fracture mechanics of engineering materials*, 4th ed., J. Wiley, NY.

Hills, J. F. (1973). "The creep of asphalt concrete mixes." *Journal of the Institute of Petroleum,* 59(570), 247.

Huang, B., Mohamad, L., and Wathugala, W. (2002). "Development of a thermo-viscoplastic constitutive model for HMA mixtures." *Journal of the Association of Asphalt Paving Technologists*, 71, 594-618.

Huang, Y. H. (1967). "Deformation and volume change characteristics of a sand asphalt mixture under constant direct triaxial compressive stresses." *Highway Research Record* 178, 60-74.

Hughes, T. J. R., and Taylor, R. L. (1978). "Unconditionally stable algorithms for quasi-static elasto/viscoplastic finite element analysis." *Computers and Structures,* 8, 169-173.

Kachanov, L. M. (1958). "On Creep Fracture Time." *Izv. Akad. Nauk USSR Otd*. Tekh. 8, 26-31 (in Russian).

Khaleel, M. A., Zbib, H. M., and Nyberg, E. A. (2001). "Constitutive modeling of deformation and damage in superplastic materials." *International Journal of Plasticity*, 17, 277-296.

Kim, Y. R., and Little, D. (2004). "Linear viscoelastic analysis of asphalt mastics." *Journal of Materials in Civil Engineering*, ASCE, 16(2), 122 – 132.

Kose, S., Guler, M., Bahia, H. U., and Masad, E. (2000). "Distribution of strains within hot-mix asphalt binders." *Transportation Research Record* 1391, Transportation Research Board, Washington, D.C., 21-27.

Li, X. S., and Dafalias, Y. F. (2000). ''Dilatancy for cohesionless soils.'' *Geotechnique*, 50(4), 449–460.

Lu, Y., and Wright, P. J. (1998). "Numerical approach of visco-elastoplastic analysis for asphalt mixtures." *Journal of Computers and Structures*, 69, 139-157.

Lubliner, J. (1991). *Plasticity theory*, Macmillan Publishing Company, NY.

Lytton, R., et al. (1993). "Development and validation of performance prediction models and specifications for asphalt binders and paving mixes." *The Strategic Highway Research Program Report No. SHRP-A-357*, Washington, D.C.

Marin, E. B., and McDowell, D. L. (1997). "Semi-implicit integration scheme for rate-dependent and rate-independent plasticity." *Computers and Structures*, 63(3), 579-600.

Masad, E., Little, D., Tashman, L., Saadeh, S., Al-Rousan, T., and Sukhwani, R. (2003). "Evaluation of aggregate characteristics affecting HMA concrete performance." *Research Report ICAR 203-1*, Texas Transportation Institute, College Station, TX.

Masad, E., Muhunthan, B., Shashidhar, N., and Harman, T. (1998). "Aggregate orientation and segregation in asphalt concrete." *Geotechnical Special Publication,* ASCE, GSP 85, 69-80.

Masad, E., Muhunthan, B., Shashidhar, N., and Harman T. (1999a). "Internal structure characterization of asphalt concrete using image analysis." *Journal of Computing in Civil Engineering (Special Issue on Image Processing*), ASCE, 13(2), 88-95.

Masad, E., Muhunthan, B., Shashidhar, N., and Harman, T. (1999b). "Effect of compaction procedure on the aggregate structure in asphalt concrete." *Transportation Research Record* 1681, Transportation Research Board, Washington, D.C., 179-185.

Masad, E., and Somadevan, N. (2002). "Microstructural finite element analysis of the influence of localized strain distribution on asphalt mix properties." *Journal of Engineering Mechanics,* ASCE, 129(10), 1105-1114.

Masad, E., Somadevan, N., Bahia, H., and Kose, S. (2001). "Modeling and experimental measurements of localized strain distribution in asphalt mixes." *Journal of Transportation Engineering*, ASCE, 127(6), 477- 485.

Masad, E., Tashman, L., Somadevan, N., and Little, D. (2002). "Micromechanics-based analysis of stiffness anisotropy in asphalt mixtures." *Journal of Materials in Civil Engineering,* ASCE, 15(5), 375-383.

McLean, D., and Monismith, C. (1974). "Estimation of permanent deformation in asphalt concrete layers due to repeated traffic loading." *Transportation Research Record* 510*,* Transportation Research Board, Washington, D.C., 14-30.

Mindlin, R. D. (1965). "Second gradient of strain and surface tension in linear elasticity." *International Journal of Solids and Structures*, 1, 417-438.

Monismith, C. L. (1992). "Analytically based asphalt pavement design and rehabilitation." *Transportation Research Record* 1354, Transportation Research Board, Washington, D.C., 5–26.

Morris, J., Haas, R. C., Reilly, P., and Hignell, E. T. (1974). "Permanent deformation in asphalt pavements can be predicted." *Journal of the Association of Asphalt Paving Technologists*, 4, 11-76.

Murakami, S. (1983). "Notation of continuum damage mechanics and its application to anisotropic creep damage theory." *Journal of Engineering Materials and Technology*, 105, 99-105.

Murakami, S. (1988). "Mechanical modeling of material damage." *Journal of Applied Mechanics*, ASME, 55(2), 280-286.

Nagtegaal, J. C. (1982). "On the implementation of inelastic constitutive equations with special reference to large deformation problems." *Computational Methods in Applied Mechanics and Engineering*. 33, 469-484.

Oda, M. (1972). "Initial fabrics and their relations to mechanical properties of granular materials." *Soils Foundation*, 12(1), 17–36.

Oda, M., and Nakayama, H. (1989). "Yield function for soil with anisotropic fabric." *Journal of Engineering Mechanics*, ASCE, 15(1), 89-105.

Oda, M., Nemat-Nasser, S., and Konishi, J. (1985). "Stress-induced anisotropy in granular masses." *Soils Foundation*, 25(3), 85–97.

Oeser, M. and Moller, B. (2004). "3D constitutive model for asphalt pavements." *International Journal of Pavement Engineering*, 5 (3), 153-161.

Paley, M., and Aboudi, J. (1992). "Micromechanical analysis of composites by the generalized cells model." *Mechanics of Materials*, 14(2), 127-139.

Papagiannakis, T., Abbas, A., and Masad, E. (2002). "Micromechanical analysis of the viscoelastic properties of asphalt concretes." *Transportation Research Record* 1789*,* Transportation Research Board, Washington, D.C., 113-120.

Park, S. W., Xia, Q., and Zhou, M. (2001). "Dynamic behavior of concrete at high strain rates and pressures: II. Numerical simulation." *International Journal of Impact Engineering*, 25, 887-910.

Peirce, D., Shih, C. F., and Needleman, A. (1984). "Tangent modulus method for rate dependent solids." *Computers and Structures*, 18(5), 875-887.

Perl, M., Uzan, J., and Sides, A. (1983). "Visco-elasto-plastic constitutive law for bituminous mixture under repeated loading." *Transportation Research Record* 911, Transportation Research Board, Washington, D.C., 20-26.

Perzyna, P. (1966). "Fundamental problems in viscoplasticity." *Advances in Applied Mechanics*, 9, 253-377.

Ristinmaa, M., and Ottosen, N. S. (2000). "Consequences of dynamic yield surface in viscoplasticity." *International Journal of Solids and Structures*, 37, 4601–4622.

Roberts, F. L., Kandhal, P. S., Brown, E. R., Lee, D., and Kennedy, T. (1996). *Hot mix asphalt materials, mixture design and construction*, NAPA Education Foundation, Lanham, MD.

Rothenburg, L., Bogobowicz, A., Haas, R., Jung, F. W., and Kennepohl, G. (1992). "Micromechanical modeling of asphalt concrete in connection with pavements rutting problems." *Seventh International Conference on Asphalt Pavement,* Nottingham, United Kingdom.

Scarpas, A., Al-Khoury, R., Van Gurp, C., and Erkens, S. M. (1997a). "Finite element simulation of damage development in asphalt concrete pavements." *Proc., eighth International Conference on Asphalt Pavements*, University of Washington, Seattle, WA, 673-692.

Schapery, R. A. (1999). "Nonlinear viscoelastic and viscoplastic constitutive equations with growing damage." *International Journal of Fracture*, 97, 33-66.

Schwartz, C. W., Gibson, N. H., Schapery, R. A., and Witczak, M. W. (2004). "Viscoplasticity modeling of asphalt concrete behavior." *Geotechnical Special Publication*, 123, 144-159.

Seibi, A. C., Sharma, M. G., Ali, G. A., and Kenis, W. J. (2001). "Constitutive relations for asphalt concrete under high rates of loading." *Transportation Research Record* 1767*,* Transportation Research Board, Washington, D.C., 111-119.

Sepehr, K., Harvey, O. J., Yue, Z. Q., and El Hussein, H. M. (1994). "Finite element modeling of asphalt concrete microstructure." *Proc., third International Conference Computer-Aided Assessment and Control Localized Damage*, Udine, Italy

SHRP (1991). "Summary report on permanent deformation in asphalt concrete." *Strategic Highway Research Program Report No. SHRP- A-318*, Washington, D.C.

Sides, A., Uzan, J., and Perl, M. (1985). "A comprehensive visco-elastoplastic characterization of sand-asphalt under compression and tension cyclic loading." *ASTM Journal of Testing and Evaluation*, 13, 59-59.

Simo, J. C., and Hughes, T. J. R. (1998). *Computational inelasticity*, Springer-Verlag, NY.

Somadevan, N. (2000). "Measurements and modeling of strain distribution in asphalt concrete mixes." MSc thesis, Washington State University, Pullman, WA

Sousa, J. B., and Weissman, S. (1995). "Modeling permanent deformation of asphalt concrete mixtures." *Journal of the Association of Asphalt Paving Technologists*, 63, 225-257.

Sousa, J. B., Weissman, S., Sackman, J., and Monismith, C. L. (1993). "A nonlinear elastic viscous with damage model to predict permanent deformation of asphalt concrete mixtures." *Transportation Research Record* 1385, Transportation Research Board, Washington, D.C., 80-93.

Szabo, L. (1990). "Tangent modulus tensors for elastic-viscoplastic solids." *Computers and Structures*, 34 (3), 401-419.

Tan, S. A., Low, B. H., and Fwa, T. F. (1994). "Behavior of asphalt concrete mixtures in triaxial compression." *Journal of Testing and Evaluation*, 22(3), 195-203.

Tashman, L., (2003). "Microstructure viscoplastic continuum model for permanent deformation in asphalt pavements." PhD Dissertation, Texas A&M University, College Station, TX.

Tashman, L., Masad, E., Peterson, B., and Saleh, H. (2001). "Internal structure analysis of asphalt mixes to improve the simulation of superpave gyratory compaction to field conditions." *Journal of the Association of Asphalt Paving Technologists*, 70, 605-655.

Thomason, P.F. (1990). *Ductile fracture of metals,* Pergamon Press, Oxford.

Tobita, Y. (1989). "Fabric tensors." *Mechanics of granular materials*, *Report from TC13*, International Society of Soil Mechanics and Foundations Engineering, M. Satake, ed., Rio De Janeiro, 6–9.

Tobita, Y., and Yanagisawa, E. (1988). "Contact tensor in constitutive model for granular materials." *Micromechanics of Granular Materials*, Elsevier Science Publishers, Amsterdam, 263-270.

Toupin, R. A. (1962). "Elastic materials with couple stresses." *Archive for Rational Mechanics and Analysis,* 11, 385-414.

Truesdell, C., and Toupin, R. A. (1960). "The classical field theories." *Handbuch der physic*, III/I, Berlin-Gottingen-Heidelberg, Germany.

Van der Poel, C. (1954). "A general system describing the viscoelastic properties of bitumens and its relation to routine test data." *Journal of Applied Chemistry*, 4, 221-236.

Vermeer, P. A. (1984). "A five constant constitutive model unifying well-established concepts." *Constitutive Relations for Soils*, G. Gudehus, F. Darve, and I. Vardoulakis, eds., Balkema, Rotterdam, 175-197.

Wan, R. and Guo, P. (2004). "Stress dilatancy and fabric dependencies on sand behavior." *Journal of Engineering Mechanics*, ASCE, 130(6), 635-645.

Weissman, S. L., Sackman, J. L., Harvey, J., and Long, F. (1999). "Selection of laboratory test specimen dimensions for permanent deformation of asphalt concrete pavements." *Transportation Research Record* 1681*,* Transportation Research Board, Washington, D.C., 113–120.

Witczak, M. (1998). "Superpave support and performance models management." *NCHRP 9-19 project*, University of Maryland, MD.

Yoshimura, S., Chen, K. L., and Atluri, S. N. (1987). "Study of two alternate tangent modulus formulations and attendant implicit algorithms for creep as well as high-strain-rate plasticity." *International Journal of Plasticity*, 3(4), 391-413.

Zaghloul, S. and White, T. (1993). "Use of a three-dimensional, dynamic finite element program for analysis of flexible pavement." *Transportation Research Record* 1388, Transportation Research Board, Washington, D.C., 60-69.

Zbib, H. M., and Aifantis, E. C. (1989). "A gradient dependent flow theory of plasticity: Application to metal and soil instabilities." *Applied Mechanics,* 42 (11), 295-304.

Zbib, H. M., and Aifantis, E. C. (1992). "On the gradient dependent theory of plasticity and shear banding." *Acta Mechanica*, 92, 209-225.

Zeinkiewicz, O., Humpheson, C., and Lewis, R. (1975). "Associated and non-associated visco-plasticity in soils mechanics." *Journal of Geotechnique*, 25(5), 671-689.

APPENDIX A
RELATIONSHIP BETWEEN THE DEVELOPED MODEL AND MOHR-COLOUMB PARAMETERS (c & ϕ)

Extended Drucker-Prager yield surface, assuming no damage, is giving in the form:

$$f = \bar{\tau} - \alpha \bar{I}_1 - \kappa \tag{A-1}$$

where for extension triaxial state condition

$$\begin{aligned} \bar{I}_1 &= \frac{1}{3}\left(\bar{\sigma}_1 + 2\bar{\sigma}_3\right) \\ \bar{\tau} &= \frac{1}{d}\left(\bar{\sigma}_1 - \bar{\sigma}_3\right) \end{aligned} \tag{A-2}$$

Substituting Eq. (A-2) and the values of the effective stress in Eqs. (4-17 and 4-18) into Eq. (A-1) yields:

$$3 \cdot \frac{(1-\Delta)}{(3+\Delta)} \cdot \left(\frac{1}{d} - \frac{\alpha}{3}\right)\sigma_1 - 3 \cdot \frac{(1+\Delta)}{(3+\Delta)} \cdot \left(\frac{1}{d} + \frac{2\alpha}{3}\right)\sigma_3 - \kappa = 0 \tag{A-3}$$

For the sign convention that compression is positive, the Mohr-Coloumb yield surface is given as (Chen and Han 1988):

$$(1-\sin\phi)\sigma_1 - (1+\sin\phi)\sigma_3 - 2c\cos\phi = 0 \tag{A-4}$$

by comparing Eqs. (A-3) and (A-4) it follows:

$$\begin{aligned} \sin\phi &= \frac{\alpha\left(1+\frac{\Delta}{3}\right)+\frac{2\Delta}{d}}{\alpha\left(\frac{1}{3}+\Delta\right)+\frac{2}{d}} \\ c &= \frac{\kappa\cdot(3+\Delta)\cdot\left[\left(1+\frac{\Delta}{3}\right)-\left(\frac{1}{3}+\Delta\right)\sin\phi\right]\cdot d}{6\left(1-\Delta^2\right)\cos\phi} \end{aligned} \tag{A-5}$$

For compression triaxial condition, d is dropped out from Eq. (A-2). In isotropic case, Eq. (A-5) reduces to

$$\begin{aligned} \sin\phi &= \frac{\alpha}{\frac{\alpha}{3}+2} \\ c &= \frac{\kappa\cdot(3-\sin\phi)}{6\cdot\cos\phi} \end{aligned} \tag{A-6}$$

Eq. (A-6) is found equivalent to the relationships introduced by Chen and Han (1988) for matching Drucker-Prager to Mohr-Coulomb yield surface parameters.